Effect of Solid-Fluid Couplings on Transport in Organic Source Rocks from Molecular Simulations.

Kristina Ariskina

Thesis

for the degree of Doctor of Philosophy in Petroleum Engineering
at the University of Pau and Pays de l'Adour

Ecole Doctorale des Sciences Exactes et leurs Applications

Effect of Solid-Fluid Couplings on Transport in Organic Source Rocks from Molecular Simulations

Kristina Ariskina

Defense Date : 16/12/2022

Reviewers:

Benoit Coasne DR / CNRS - Université de Grenoble

Céline Merlet CR / CNRS - Université de Toulouse

Examiners:

Didier Bégué PR / Université de Pau et des Pays de l'Adour

Zhehui Jin PR / University of Alberta

Directors of thesis:

Guillaume Galliéro PR / Université de Pau et des Pays de l'Adour

Amaël Obliger CR / CNRS - Université de Bordeaux

Acknowledgment

The thesis work has been carried out in the ”Thermophysical Properties” research team of the Laboratory of Complex Fluids and their Reservoirs (LFCR) at the University of Pau and Pays de l’Adour.

First of all, I would like to thank my thesis directors, Dr. Amaël OBLIGER and Pr. Guillaume GALLIÉRO, for their invaluable assistance and expert knowledge they have given me throughout these three years of my PhD study.

I would especially like to thank Dr. Benoit COASNE and Dr. Céline MERLET who have honored me by accepting to be the reviewers of this thesis. Also, I thank Pr. Didier BÉGUÉ and Pr. Zhehui JIN for having accepted to examine this work and to be part of the defense jury.

I would like to extend my appreciation to Dr. Jean-Marc Leyssale and his PhD student Kévin Potier from the University of Bordeaux for their research collaboration. It is also an opportunity for me to thank all my colleagues at the LFCR at the University of Pau and Pays de l’Adour and the Theoretical Chemistry and Modeling Group of the Institute of Molecular Sciences at the University of Bordeaux, as well as my friends.

Finally, my most sincere thanks go to my family, and in particular my parents and my sister Regina ARISKINA for their encouragement during my thesis. This work is dedicated to them.

Contents

List of Figures

Chapter 1

Introduction

Contents

1.1 | Scope

1.1.1 | Organic Source Rocks Study

In the geological context, organic source rocks or their insoluble part, kerogen, which occupies the majority of the whole diversity of organic matter (OM), is of great interest and value in the industry because of the fluids adsorbed or potentially able to be adsorbed in it. Despite the ability to expel and migrate to reservoir rocks, large amounts of hydrocarbons remain trapped in organic pockets of ultra-low porosity in what is named shale. Thus, due to its strong adsorption potential, kerogen is important for two global challenges. Firstly, shale represents one of the Earth's largest reservoir of crude oil and gas reserves [10, 11], and kerogen knowledge is crucial for their exploitation. Second, because of its characteristic microscale porous phase (pore size less than 2 nm), kerogen could potentially be used for the sequestration of fluids of interest, such as carbon dioxide and hydrogen, to reduce the effects of climate change. One of the key processes controlling the success of fluid extraction or storage in shale is fluid transport in kerogen. In contrast to a bulk fluid, when confined in a microscale porous matrix, as in kerogen, fluids move more chaotically, preventing the development of long-range hydrodynamic modes and ensuring the diffusive nature of its transport properties. Moreover, transport, being highly affected by solid dynamics is accompanied by phenomena, such as poromechanics and adsorption effects which are still poorly understood despite recent progresses made at the molecular scale [2, 5–7].

As a starting point in the study of kerogen, a generally accepted classification was proposed by Dirk Willem Van Krevelen [12] distinguishing organic matter by its chemical composition, that is the atomic H/C and O/C ratios [13], and according to the depositional origin. The maturation of the organic matter, which produces both the kerogen and the hydrocarbons over millions of years timescale, occurs during the sedimentation process of the rocks hosting the organic matter. The corresponding diagram identifying four kerogen types is displayed in figure 1.1.1. The type I kerogen usually belongs to lacustrine origin, the type II to marine origin, the type III to terrestrial origin, and the type IV to residual origin. The kerogen is also classified according to its maturation stage, globally going from the top-right to the bottom-left parts of the diagram. The maturation process follows three main stages: diagenesis, catagenesis and metagenesis. The former is characterized by high H content, resulting in structures with often prevailing short aliphatic chains, and is mainly inherent of kerogen type I. At this stage, kerogen begins to generate oil, i.e. it is the beginning of the oil window. Kerogen at the stage of catagenesis is in the most effective state for the formation of oil, with a predominant amount of C. At the end of this stage, gas formation becomes more intensive: the oil window turns into the gas window (kerogen types II and III). Kerogen in the last maturation stage, called metagenesis, (types III and IV kerogen) produces only gas, being in the gas window and consisting mostly of C, which leads to a structure with often aromatic rings giving rigidity to the matrix.

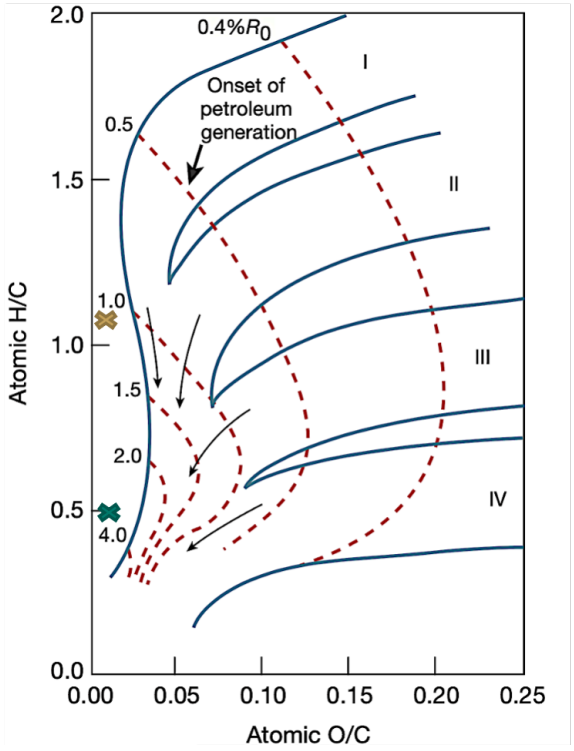

Figure 1.1 | Van Krevelen diagram indicating the kerogen maturation within a two-dimensional O/C – H/C map and taken from [1]. The red dashed isolines correspond to the vitrinite reflectance that is used by experimentalists to quantify the maturity. The atomistic models of kerogen of immature type I (brown cross) and mature type III (green cross) used in my work are indicated.

The high variety of kerogens resulting from the different origins and maturation stages induces a high complexity in accounting for their various physico-chemical properties, such as chemical composition (also accounting for N and S elements), ultra-low porosity, internal flexibility and structural heterogeneity. All these should be accounted for in transport and adsorption investigations. However, such studies have frequently overlooked some important characteristics of shales as the amorphous nature and flexibility of their organic part [14, 15]. Being coupled to empirical or semi-empirical analytical models, experimental results on diffusion [16, 17] and adsorption [18, 19] have been based on oversimplified assumptions – surface diffusion, etc. Overall, only a small number of papers have been devoted to adsorption experiments on kerogen isolated from shale [20–22], where the description of the solution behaviour has been proved to deviate from the regular solution theory. Similarly, only a few studies have reported diffusive transport in kerogen based on experiments measuring, for instance, fluid concentration [23, 24]. It is noteworthy that methods based on nuclear magnetic resonance phenomena have been widely used in laboratory measurements of adsorption properties of organic matter and fluid diffusivities [25–28]. Due to the time-consuming and costly laboratory experiments, more attention has been paid to simpler structures, coals, for which the free porous volume was mainly estimated by

solvent or gravimetric swelling [29, 30] and adsorption and diffusion have been investigated using volumetric method [31–33].

Together with the high complexity of in situ transport analysis in shales and the extraction of kerogen samples without destroying the kerogen structure and composition [34], all this has led to the development of Molecular Dynamics (MD) tools to complement these not numerous experimental studies. As such MD tools have extensively been used to study transport properties of fluids in various porous media, MD simulations have begun to be used along with experiments, and then as an advanced technique for studying such ultra-low permeability porous materials. Atomistic kerogen models, in turn, have led to numerous pioneering works, some of them covered in review [35] and discussed below, which have advanced the understanding of transport phenomena in kerogen.

1.1.2 | Brief Review of Kerogen Atomistic Models

Numerical study of transport properties in kerogen has become a great challenge of the past decade. The inherent structural organisation of kerogen, being a key factor in determining the mechanisms of the fluid dynamics, has been simulated from different points of view. Various atomistic model of kerogen matrices have been recently proposed, either by representing it by focusing on the disorder of the micro porous network [6, 36], the chemical diversity [4], the structure [3], the mechanics [2], or the degradation process [37]. Some of those models are shown in figure 1.2.

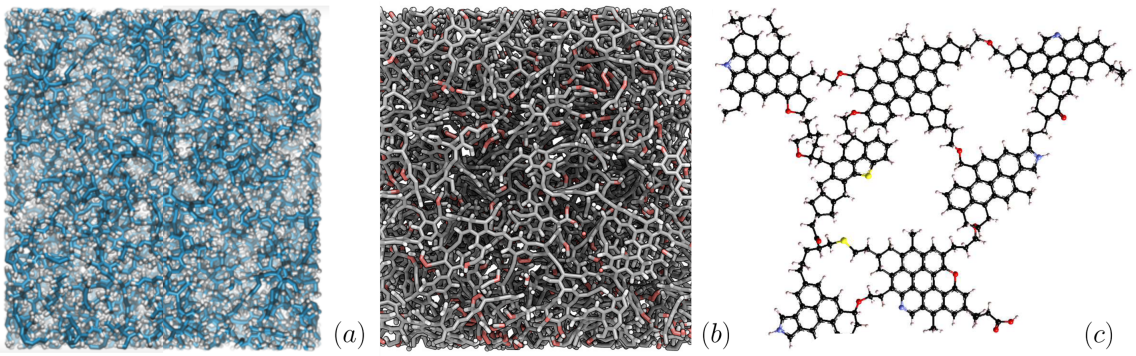

Figure 1.2 | Snapshots of different atomistic micro structures of kerogen found in the literature. The kerogen models with (a) C (blue) and H (white) [2], (b) C (black), H (white) and O (red) [3],(c) C (black), H (white) and O (red), S (yellow) and N (purple) [4]. They are built using (a) a liquid quench MD simulation, (b) hybrid reverse Monte Carlo reconstruction method, and (c) by annealing and cooling MD simulations containing several identical molecules accurately reproducing the kerogen chemistry.

The representative size of the kerogen matrix has been varied from 584 [38] and 680 [39] total atoms to 19574 atoms [2], using multiple techniques for generating the organic structure. One widely used method has been the construction of molecular models of kerogen by transferring experimental results from nuclear magnetic resonance spectroscopy, X-ray

photoelectron spectroscopy, thermal and elemental analyses, etc. as input data for molecular simulations [39–43]. Another method has been based on the imitation of porous disordered organic structures through the introduction of dummy particles of different sizes [4, 44, 45]. In order to build reticulated kerogen models, quenching simulations have been used with a reactive force field, first melting a liquid system at a very high temperature (6000 K) followed by a cooling at a typical reservoir temperature (~400 K) [2]. A technique relying on experimentally obtained kerogen characterization, and using a reconstruction method based on the Hybrid Reverse Monte Carlo (HRMC) method to get close to real kerogen structures and textures, also using a reactive force field, has been applied in [3]. Even attempts to simulate the geological evolution of kerogen precursors (lignin and cellulose) have been successfully accomplished with Replica Exchange MD (REMD), manipulating multiple copies of the system at different temperatures to accelerate the natural pyrolysis of the precursors [37, 46, 47].

Despite the different representations and applied construction methods, mostly all models of shales' organic matter have structural/mechanical/compositional properties close to those of experimentally extracted kerogen samples [48, 49]. The well-modeled characteristic properties allows studying by MD the transport of the fluids adsorbed in kerogen.

1.1.3 | Molecular Simulations of Transport in Kerogen

The multi-scales porosity of the organic part of a gas and oil reservoir implies different approaches to fluid transport, taking into account the modulated importance of the solid/fluid interactions. In the macroscale porosity (pore size above 50 nm), fluids are very close to their bulk state. In this case, both the fluid and the solid constitute distinct phases described by their bulk properties. Thus, the phenomenological Darcy's law relating the pressure gradient ∇P applied to the fluid and its resulting flow velocity v at steady-state as

$$v = -\frac{k}{\eta}\nabla P \tag{1.1}$$

where η is the bulk fluid viscosity and k is the intrinsic solid permeability, is valid.

Within the mesoscale porosity (pore size below 50 nm and above 2 nm), fluid molecules may adsorb on the pore walls, which involves additional parameters in the poromechanical relation, such as surface stress and specific pore area. Meanwhile, the classical Darcy description has proved to be invalid for describing transport in kerogen despite attempts to extend this classical transport equation with additional parameters, and transport in mesoscale pores has been determined to be of little significance compared to that at lower scales for kerogen [50].

For kerogen microscale porosity (pore size less than 2 nanometers), which controls the adsorption and transport properties, the known relationships for the solid-fluid porome-

chanical coupling and the transport affected by this coupling, were found to be untenable, as strong adsorption/surface effects appears. Most of the numerical works have been devoted to the study of adsorption properties [3, 4, 15, 51–56]. The following insights have been established: the linear dependence of adsorption capacity on maturation level and type of kerogen and its ability to adsorb fluids [3, 55, 57], the inverse dependence of adsorbed fluid amount to the chain length of hydrocarbons at high applied pressure inducing porosity decrease which is valid for hydrocarbons'mixtures as well [4, 53], and the strong impact of thermodynamic conditions on gas adsorption [58]. Furthermore, wettability effects may also be involved and has been accounted for in MD simulations incorporating water into the kerogen model, which resulted in stronger adsorption effects than for carbon dioxide and methane [59–63].

In contrast to MD studies of adsorption in the microscale porosity, transport has only been scarcely studied. Botan and colleagues were among the first to point out the inapplicability of conventional laws to describe the flows found to be non-continuum in a disordered and microscale porous carbon model close to a kerogen microstructure [36]. Fluid transport have been determined to be diffusive from MD simulations of kerogen [14, 64, 65] and previously for simple microscale porous materials (1D, 2D models) [66, 67]. Affected by significant fluid adsorption and interfacial effects, the investigation of transport mechanisms requires consideration of the influence of all occurring phenomena.

Collell and co-workers have contributed to the study of single and multicomponent diffusion in a self-built molecular model of organic matter [4, 5, 68]. They revealed the impact of fluid loading and chemical content on the diffusivity and proposed a transport model for simple hydrocarbons' mixtures. The impact of kerogen maturity and another physico-mechanical properties as well as different conditions on fluid diffusion has been extensively investigated [6, 50]. Obliger et al. have carried out a series of works [2, 14, 64] to study various aspects of fluid transport at the microscale. The decrease in transport with increasing amounts of fluid has been well captured by a free volume theory with linear alkanes (up to dodecane) for pure fluids [6], mixtures [14], and within a collection of different kerogen models [64].

The choice of fluid and applied thermodynamic conditions have also been raised. The majority of adsorption and transport studies have been carried out for methane, longer-chain HCs, carbon dioxide and their mixtures under typical geological conditions and near [17, 69–73] due to the particular interest in carbon dioxide to enhance gas/oil recovery and for the purpose of its sequestration. For carbon dioxide adsorbed in kerogen, stronger solid-fluid coupling caused by its greater adsorption capacity than for methane has been determined, which is favorable for hydrocarbon recovery from shale as well as for carbon dioxide storage.

Notably, the majority of the above mentioned numerical studies have often been performed within the rigid kerogen approximation implying immobility of solid's atoms during the simulations. However, despite the differences in terms of the origin and maturity be-

tween kerogen types, the inherent flexibility is present to certain extent in each kerogen sample. Total or partial freezing of solid's atoms in the majority of works on swellable kerogen models [2, 5, 6, 14, 44, 45, 63, 64] prevents natural volume deformations/fluctuations notwithstanding the important solid-fluid interactions. Thus, this has led to the highly limited movements of fluid molecules during their adsorption due to the invariance of the free volume which has resulted in decreasing transport trends with fluid amount (figure 1.3).

Transport and fluid dynamics in general depend on the mechanical constraints applied on the solid/fluid system as well as the mechanical response of the solid, that can be influenced by the adsorption of fluid when poroelastic couplings are important. For a macroscale porous media, the poroelastic solid/fluid coupling is described through the Biot constitutive law $\sigma = K\epsilon - bp$ relating the confining stress σ, bulk modulus K, volumetric strain of the system ϵ, Biot coefficient b and fluid pore pressure p. Within the mesoscale porosity, fluid/-solid interactions cannot be fully neglected anymore, which involves additional parameters in the poromechanical relation, such as surface stress and specific pore area. Then, in the microscale porosity, such interactions predominate and a mechanics framework integrating thermodynamics becomes necessary as illustrated in [2, 74, 75]. Attempts to quantitatively describe the coupled behavior of porous solid and fluid have been made in the case of regular pore geometries by introducing the disjoining pressure [76–80].

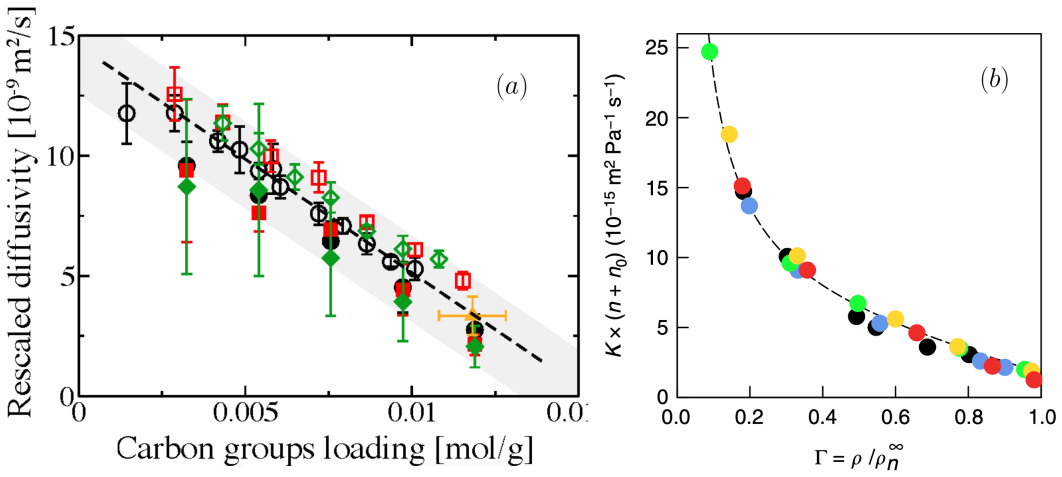

Figure 1.3 | (a) Rescaled diffusivity [5] and (b) permeance [6] of different hydrocarbons and their mixtures as functions of fluid loading within rigidified kerogen models.

Within low-permeability gas/oil deposits fluid adsorption/desorption leads to the volume expansion or contraction due to the strong interplay between the solid and the fluid. These effects are more pronounced in immature kerogens and, to a lesser extent, in mature ones. As opposed to the use of the popular rigid approximation, Obliger et al. found that the volumetric strain induced by adsorption in immature and overmature kerogen models during adsorption were important for the immature one and negligible in the overmature one [2]. Thus, neglecting the matrix internal deformations is a rather crude approximation

maybe even considering mature kerogens that can exhibit adsorption-induced swelling. Carbon dioxide has been found to swell in kerogen more than methane and other hydrocarbons [70]. Several works have been done for argon and nitrogen adsorption at low temperature conditions to properly capture the poroelastic behavior of the solid matrix during fluid adsorption [77, 81, 82]. Based on the previous MD simulations of kerogen, the impact of flexibility effects on solid-fluid couplings has been poorly investigated. Kerogen atomistic representations accounting for adsorption-induced swelling effects on fluid transport have been introduced only recently [7]. It has been shown that adsorption-induced swelling has an important role on the dynamics of an adsorbed fluid in a flexible kerogen matrix. The previously established trend of decreasing transport properties with the amount of adsorbed fluid has been revised in this case where significant swelling arises due to fluid adsorption. On the contrary to rigid, or rigidified, matrices, fluid adsorption assists the fluid flux in deformable kerogens (figure 1.4). We refer the interested reader to a recent comprehensive review [83] summarizing previous contributions and recent insights into gas flow processes in shales — adsorption and diffusion.

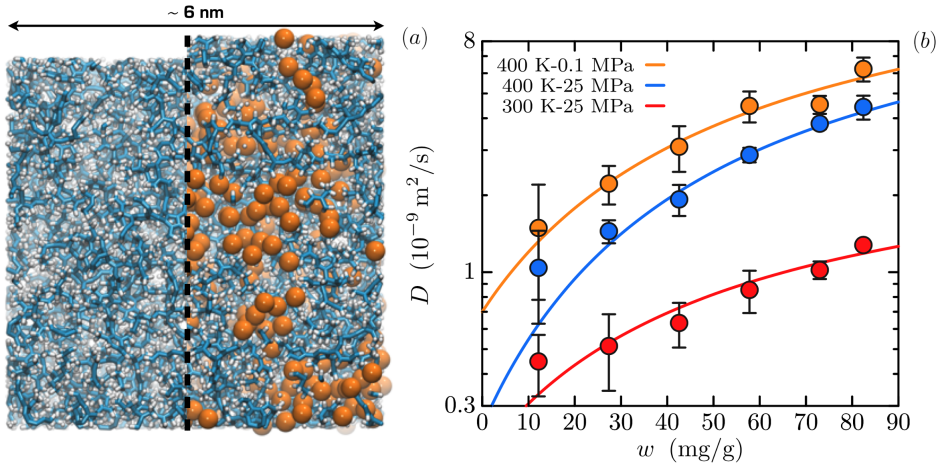

Figure 1.4 | (a) Snapshot of the flexible kerogen matrix extracted from [7] and (b) the increasing trend of the diffusivity with fluid loading due to the adsorption-induced swelling.

Based on the above studies, as a step towards developing a general theory of transport in microscale porous kerogen, it appears to be important to thoroughly study the impact of fluid adsorption-induced swelling, and poromechanical properties of kerogen on microscale transport, which has been not sufficiently reported for a comprehensive understanding of the diffusion mechanism within a deformable host organic matter.

1.2 | Thesis Motivation

We have shown that transport in microscale porous kerogen has been mostly investigated within an approximation of rigid kerogen. Indeed, the flexibility of the matrix resulting in

adsorption-induced swelling has often been neglected in the transport properties studies. Only recently has the importance of accounting for matrix deformations during adsorption and fluid diffusion been clearly demonstrated for swellable nanoporous organic matter. In that regard, a particular attention in this thesis is paid to the flexibility effects, i.e. the impact of internal motions of matrix atoms on the propagation of the molecular fluid diffusion based on the MD simulations. In order to study flexibility effects, we encompass a wide range of oil and gas-bearing kerogens, considering two kerogen models: a type I immature model in the middle of the oil window (H/C $\sim$ 1.5–0.7) with H/C= 1.1 and a mature lignin-based Type III model at the end of the gas window ($\sim$ 1.0–0.5) with H/C= 0.5, which are indicated in the Van Krevelen diagram (figure 1.1.1). For both kerogen models we provide an extensive analysis of its pore-volume characteristics evolution with fluid adsorption. Within the immature model we then verify for the first time if solid's volumetric and internal deformations are able to contribute to the cross-correlations between fluid molecules and consequently to the change of the fluid transport nature by studying two fluids, methane and carbon dioxide, at a wide range of thermodynamic conditions and from very long MD runs counting tenth of nanoseconds. The poromechanical properties upon gas adsorption are carefuly captured for a mature kerogen model by applying low temperature (243 K) and large pressure range ($\sim 5 \times 10^{-3}$ to $\sim$ 220 MPa). For both kerogen models, we provide an extensive analysis of the evolution of its pore-volume characteristics upon fluid adsorption.

Another important point that we emphasize is the choice of the representative box size and the homogenization during the initial construction stage of molecular kerogen models. It is well known that computational time and supercomputer power limit the study of confined transport when building a realistic solid model. Consequently, this implies important size effects for 3D molecular kerogen models, which together with the flexibility of the kerogen model and its disordered network can cause anisotropy [15, 65]. The latter will lead to anisotropic transport properties, which is undesirable in transport analysis, even if fluids within nanoscale pores of various materials often show transport anisotropy [84, 85], that should not be the case for highly amorphous materials such as kerogen. Thus, the representativity of the kerogen model is discussed in this work.

Moreover, by replacing the methane molecules by carbon dioxide molecules in the immature kerogen model allowed us to compare these models at the same molar loading in the context of gas production and carbon dioxide sequestration. The analysis of local microscale deformations is performed after the replacement of methane by carbon dioxide in order to further comment on the effects of flexibility.

Flexibility effects play a crucial role in fluid transport trends, as we have shown previously. We have analyzed diffusion trends for immature kerogen under different fluids, loading, and different applied temperatures and pressures. We observed that increases in transport correlate strongly with increases in accessible free volume; we rationalized these trends for methane and carbon dioxide using the free volume theory. From this free volume model, we extracted coefficients characterizing the coupling between solid and fluid and explained

their evolution as a function of thermodynamic conditions for both fluids. Diffusion has been examined in a mature model for three adsorption schemes, with the matrix allowed to deform, at a fixed volume and total rigidity, in order to have a clear understanding of the effect of flexibility on transport.

Finally, inspired by recent work on hydrodynamics prediction based on memory kernel reconstruction, which incorporates delayed fluid response to environmental dynamics for molecular bulk fluid [9], we have used a coarse-grained technique based on the generalized Langevin equation employing two algorithms for the memory kernel reconstruction. We study the impact of the important flexibility effects in the immature kerogen compared to the rigidified case and of the fluid adsorption on the dynamics of methane. Additionally, an attempt has been made to reproduce the transport coefficient from autocorrelation functions of atomic velocity, force and noise (projected force related to the memory kernel), introducing the perspective of building multi-scales simulations techniques to incorporate the influence of the mesoscale pores at the next scale.

The purpose of all this is to contribute to the construction of a general theory of transport in microscale porous organic matter through an emphasis on the effects of adsorption-induced swelling and solid-state flexibility.

1.3 | Outline

The outline of this thesis is the following:

- Chapter 2 first presents the general concepts of transport, and then the basics of molecular dynamics simulations, the methods about kerogen model construction and adsorption within, and the methods for calculating transport properties.
- Chapter 3 is devoted to the study of fluid transport in kerogen involving immature and mature kerogen, considering different fluids, for a wide range of thermodynamic conditions. To begin with, we show an analysis of the porous characteristics of immature and mature models under adsorption-induced swelling. Then, the effect of immature kerogen flexibility on the collective fluid effects for both fluids, methane and carbon dioxide, is studied. Anisotropy is also discussed in this chapter. Finally, adsorption-induced transport is studied for both kerogen models, immature and mature.
- Chapter 4 shows the results of free volume theory-based transport modelling for methane and carbon dioxide.
- Chapter 5 introduces a coarse-grained technique based on the reconstruction of so-called memory kernel that stores the memory of past fluid dynamics affected by solid dynamics, and its application to studying fluid dynamics in the immature kerogen model through memory effects for methane.

- Chapter 6 contains general conclusions and perspectives of the present work.

CHAPTER 2

Methodology of Fluid Transport Modelisation in Kerogen

Contents

2.1 | Introduction

The focus of this chapter is on a brief explanation of Molecular Dynamics (MD) simulations in general and a description of the MD setups used in this thesis in particular. In addition, the way the two kerogen models studied in this thesis have been built and dealt with is described in the present chapter. Thus, the following sections are introduced in this chapter:

- The first section is devoted to the general transport theory in microscale pores. Moreover, the main idea of the transport modeling in kerogen is explained with the support of basic equations.
- The second section provides the fundamental principles of molecular dynamics simulations.
- Atomistic representations of kerogen models are introduced in the third section. Rigidified and poroelastic models and their impact on transport are compared.
- The fourth section describes the used molecular models built to explore flexibility effects and the numerical setups used to compute transport properties in flexible kerogen.

2.2 | General Transport Theory in Microporous Solids

Transport at scales characteristic of atomic interactions is of great interest not only in geological applications such as greenhouse gas sequestration and hydrocarbons extraction, but also in a tremendous number of industrial processes - gas separation, selective removal of radioactive elements from nuclear waste, catalytic processes, etc. Causing phenomena such as slippage, adsorption effects, friction, wettability, whose mechanism is not always fully clear, the general principles accounting for confinement induced solid-fluid couplings need to be well-defined.

Scientists first began to consider a fundamental theory of the ultra-confined transport in carbon structure since the late twentieth century, determining the non-viscous nature of fluid flow from experiments, [24] and mostly from molecular simulations [86, 87] and theoretical studies [88] owing to the difficulty of appropriate laboratory measurements. The fundamental Darcy's transport description has been successfully applied to fluids confined down to a few nanometers through the use of phenomenological parameters independent of each other to characterize a fluid (viscosity), a confining solid (permeability) and an environment (pressure gradient). Inspired by this applicability over a wide range of characteristic

scales, from macro- to nano-scale, numerous works have been devoted to the modification of this law by involving correction factors to fit ultra-confined transport [89]. Alternatively, Vanderlick T. and Davis H. proposed a microscopic description of the hydrodynamic flow equations based on the Enskog's diffusion theory [88]. However, this approach is capable of consistently describing transport only for a single-component gas and was inapplicable to gas mixtures. Attempts to apply the continuum potential failed to correctly model the coupling between fluid molecules and the solid wall [87]. Overall, from 1 nm and below, continuum principles and their extensions proved unable to fully capture the fluid transport mechanisms [53, 64] as the parameters of the Darcy's flow equation became sensitive to each other. Indeed, at such scales the right driving force is the chemical potential gradient which is not fully embodied in the pressure gradient used in the Darcy's law. The most recent findings have come from a model that accounts for adsorption effects [7]. By incorporating the solid-fluid couplings, it describes well the transport properties affected by the solid's poromechanics, its ability to swell upon fluid adsorption, and flexibility effects. This model could yield a framework for a proper capture of fluid mechanics within a microscale confinement.

2.2.1 | Modelling the Fluid Transport

This section is devoted to the fundamentals of molecular modeling of transport properties at equilibrium with a focus on the diffusion coefficient computation. The fluid particles positions used in the calculation algorithm stand in the reference frame of the solid and thus do not depend on a molecular model.

Transport Model Equations

I first recall here the usual Darcy's law that relates the steady-state velocity $\boldsymbol{v}$ of a fluid confined in a porous media as a response to an applied pressure gradient ∇P:

$$\boldsymbol{v} = -\frac{k}{\eta}\nabla P\,. \tag{2.1}$$

This law is valid within the linear response regime where the pressure gradient that trigger the flow is sufficiently small to stay in the Stokes regime. Darcy's law makes use of two specific quantities to characterize such linear response, the bulk fluid viscosity η that depends only on the fluid nature, and the intrinsic permeability k that only depends on the geometry of the pore space. This phenomenological law has also benefited from a theoretical derivation [90] starting from hydrodynamics and describing the local behaviour of a fluid and using the volume averaging theory to upscale transport at the scale of the homogenized porous sample. This suggests that in the case of confined fluids where solid-fluid interactions cannot be neglected on the fluids properties, thermodynamic and dynamical, such law will breakdown as hydrodynamics fails to account for the discrete — molecular — nature of the

fluid and the solid impacting the dynamic behaviour of the fluid. This was clearly evidenced by Falk et al. [6] in the specific case of transport of linear alkanes in a microscale porous model of kerogen, while treating the carbon structure as rigid.

Following this work within the kerogen model, the permeance K has been introduced to characterize the linear response between the pressure gradient and the flow within such confining media. The pressure gradient remains sufficiently small to guaranty the linear response regime. As a replacement for Darcy's law, we get a generic law

$$\boldsymbol{v} = -K\,\nabla P \tag{2.2}$$

that can be immediately generalized to the multicomponent case

$$\boldsymbol{v}_i = -K_i\,\nabla P \tag{2.3}$$

where the index i labels the different fluid species involved in the mixture. The flows of species arise from thermodynamic perturbations, which can be formalized by chemical potential gradients $\nabla\mu_i$, to which any species of the mixture can respond by fluids internal cross-correlations. We then return to the general framework devised by Onsager L. relating the flows of n mixture species to all chemical potential gradients as

$$\boldsymbol{v}_i = -\frac{1}{x_i k_B T}\sum_{i=1}^{n}\Lambda_{ij}\,\nabla\mu_j \tag{2.4}$$

where $x_i = N_i/N$ is the molar fraction of the species i with N standing for the number of molecules, k_B is the Boltzmann constant, and Λ_{ij} is the Onsager transport coefficient relating the flow of species i responding to the chemical potential gradient of species j. Those coefficients are the elements of the Onsager matrix Λ, which is positive and symmetric ($\Lambda_{ij} = \Lambda_{ji}$). When a chemical potential gradient is applied to a single species j, if the internal fluid cross-correlations between species cannot be neglected, then the other species will flow besides species j as well, otherwise the Onsager cross-coefficient Λ_{ij} is zero, indicating that cross-correlations between different species do not affect the transport properties. But, in general, even if these cross terms are zero, the transport of a component in response to its chemical potential gradient can be affected by other molecules, i.e. , the diagonal transport coefficients depend on the concentration of all the species.

Alternatively to equation 2.4, introducing the species flows $\boldsymbol{j}_i = \rho_i\boldsymbol{v}_i$ with $\rho_i = N_i/V$, the molar density of species i, the previous relation can be expressed as $\boldsymbol{j}_i = -\beta\rho\sum_{i=1}^{n}\Lambda_{ij}\,\mu_j$ where β is the inverse temperature and $\rho = N/V$ is the total molar density of the fluid mixture. The arrangement of flows j_i and chemical gradients $\partial_x\mu_i$ on n size arrows $\boldsymbol{J}$ and $\boldsymbol{F}$,

respectively, allows using the following matrix relation

$$\boldsymbol{J} = -\beta\rho\Lambda\,\boldsymbol{F}\,. \tag{2.5}$$

$$\boldsymbol{J_i} = -\sum_{i=1}^{n} D_{ij}\nabla c_j\,. \tag{2.6}$$

We assume in this section that the transport properties are isotropic for the sake of simplicity.

When considering steady states in a linear regime, flows responding to pressure or chemical potential gradients are identical to those resulting from constant volumetric forces. Thus, applying a pressure gradient is equivalent to applying a constant force

$$\boldsymbol{f}^{(P)} = -\nabla P/\rho \tag{2.7}$$

over all the mixture molecules which differs from applying a constant acceleration when the molecules have different masses. Applying a chemical potential gradient is equivalent to applying a constant force

$$\boldsymbol{f}_i^{(\mu)} = -\nabla\mu_i \tag{2.8}$$

over the molecules of species i only. Consequently, the steady state resulting from a pressure gradient applied to multicomponent fluids is equivalent to the steady state occurring when the same chemical potential gradient is simultaneously applying to all components of the fluid, i.e. $\boldsymbol{f}^{(P)} = \boldsymbol{f}^{(\mu_1)} = ... = \boldsymbol{f}^{(\mu_n)}$, which implies that $\mu_i = \nabla P/\rho$. Substituting this equality into equation 2.4 in the case of applied pressure gradient to multicomponent fluid and comparing with equation 2.3 allows expressing permeances K_i as a function of Onsager transport coefficients Λ_{ij} as

$$K_i = \frac{\beta}{\rho_i}\sum_{j=1}^{n}\Lambda_{ij}\,. \tag{2.9}$$

Within the linear response regime, the fluctuation-dissipation theorem allows the derivation of the so-called Green-Kubo relations between Onsager transport coefficients Λ_{ij} and equilibrium fluctuations of the corresponding flow velocities $\boldsymbol{v}_i$ and $\boldsymbol{v}_j$:

$$\Lambda_{ij} = \frac{N_i N_j}{3N}\int_0^\infty \langle \boldsymbol{v}_i(0)\cdot\boldsymbol{v}_j(t)\rangle_{\text{eq.}}\,\mathrm{d}t\,. \tag{2.10}$$

Conversely, displacements of the centers of mass (c.o.m.) $\boldsymbol{r}_i$ of the species can be considered instead of the flow velocities giving the Einstein's relations

$$\Lambda_{ij} = \frac{N_i N_j}{6Nt} \lim_{t\to\infty} \langle \Delta \boldsymbol{r}_i(t) \cdot \Delta \boldsymbol{r}_j(t) \rangle_{\text{eq.}} . \tag{2.11}$$

The three dimensional isotropic case has been considered. It should be noted that the diagonal transport coefficients and collective diffusion coefficients $D_i^{(\text{c})}$ are related as

$$\Lambda_{ii} = x_i D_i^{(\text{c})} . \tag{2.12}$$

Simply stated, the collective diffusion coefficient is the self-diffusion coefficient of the species c.o.m. multiplied by its number of molecules N_i.

Additionally, the diagonal terms Λ_{ii} can be separated into self and collective contributions. Expanding the c.o.m. values, velocities $\boldsymbol{v}_i = \sum_{k=1}^{N_i} \boldsymbol{v}_{i,k}/N_i$ and positions $\boldsymbol{r}_i = \sum_{k=1}^{N_i} \boldsymbol{r}_{i,k}/N_i$, using molecular quantities where the index k denotes molecules of the species i, leads to

$$D_i^{(\text{c})} = D_i^{(\text{s})} + \frac{1}{3N_i} \sum_{k\neq l}^{N_i} \int_0^\infty \langle \boldsymbol{v}_{i,k}(0) \cdot \boldsymbol{v}_{i,l}(t) \rangle_{\text{eq.}} \, \mathrm{d}t \tag{2.13}$$

or, equivalently,

$$D_i^{(\text{c})} = D_i^{(\text{s})} - \lim_{t\to+\infty} \frac{1}{3N_i t} \sum_{k\neq l} \langle \boldsymbol{r}_{i,k}(t) \cdot \boldsymbol{r}_{i,l}(0) \rangle . \tag{2.14}$$

The first term is the self-diffusion coefficient of the species i, quantifying the mean square displacement of the individual molecules of the corresponding species, and the second term sums up all cross-correlations between different molecules of the same component contributing to the transport coefficient.

Post-treatment Transport Coefficients Calculation

Steady-state transport properties can be obtained from the self- and collective diffusion coefficients of the adsorbed fluid, which can be simply derived from equilibrium MD calculations. Consider for simplicity the derivation of these transport coefficients from a one-dimensional fluid motion on the x direction. To evaluate the self-diffusion coefficient D_{s} of a single fluid molecule, one can compute its Mean Square Displacement (MSD) in the solid's reference frame, $\langle \Delta x^2(t) \rangle = \langle (x(t+t_0) - x(t_0))^2 \rangle$with time t, which, after a sufficiently long time reaches a linear regime as

$$\langle \Delta x^2(t) \rangle = 2D_{\text{s}}\, t + A \tag{2.15}$$

In practice, the MSD is averaged over all the confined fluid molecules and a sliding average over the initial time t_0 is achieved thanks to the stationarity of the trajectories.

To investigate the collective effects impacting the long term diffusion process within the kerogen matrix the collective diffusion coefficients are compared with the self-diffusion coefficient. Similarly, tracking the MSD of the fluid c.o.m. (x_c) allows to evaluate the collective diffusion coefficient D_c from

$$\langle \Delta x_c^2(t) \rangle = 2\frac{D_c}{N}\, t + B \tag{2.16}$$

The linear fits used to determine the self- and the collective diffusion coefficients are performed from a few hundreds of ps to 10 ns or 50 ns, respectively. The error bars with 95% confidence interval estimated from 5 independent trajectories for each condition.

From the use of the definition of the c.o.m. in equation 2.16 and relating equations 2.15 and 2.16 in the long time limit, the difference between these two transport coefficients can be explicitly expressed through the cross correlations terms, quantifying the collective effects, as shown by

$$D_c = D_s - \lim_{t\to+\infty} \frac{1}{tN} \sum_{i\neq j} \langle x_i(t) x_j(0) \rangle \,. \tag{2.17}$$

Alternatively, as recalled in [2,6] the Green-Kubo relationship can be invoked to express the cross term in the form of the integral of the velocity cross-correlation function as

$$D_c = D_s + \lim_{t\to+\infty} \frac{1}{N} \sum_{i\neq j} \int_0^t \langle v_i(t') v_j(0) \rangle \, \mathrm{d}t' \,. \tag{2.18}$$

2.3 | Basics of Classical MD Simulations

Molecular Dynamics simulation used in the thesis is a numerical-based approach which uses the classical mechanics laws in trying to reproduce realistic molecule's movements at the atomistic scale without involving quantum effects. The idea behind this method is to assign to each atom 6 degrees of freedom – 3 for the position and 3 for the momentum – and to be able to express the desirable property through these microscopic parameters (assuming the ergodic theorem, see [91]) using long time trajectories [92]. The evolution of the system in time on the atomic scale is achieved from MD thanks to Newton's second law:

$$m\frac{\mathrm{d}v(t)}{\mathrm{d}t} = f(t)\,, \tag{2.19}$$

where we focus on the dynamics of an atom of mass m with velocity v, and where f is the total force exerted on the atom by all the other ones. Integrating this equation over time

allows to obtain the velocity and then the position of each molecule of the system. A widely used algorithm for providing the temporal evolution of a microscopic system in a discretised manner is the velocity Verlet algorithm [93], which is based on the Taylor expansion of the molecule position r which can be taken for the x, y or z coordinate. The principle is that the microscopic variables (r, v and the acceleration a) known at a certain time t yield the molecule position after a timestep of duration δt at $t + \delta t$ where t' is the timestep:

$$r(t + \delta t) = r(t) + \delta t v(t) + \frac{1}{2}\delta t^2 a(t)\,. \tag{2.20}$$

The acceleration a at $t + \delta t$ can be thus computed from the gradient of the potential energy U:

$$a(t + \delta t) = -\frac{1}{m}\frac{\partial U}{\partial r}(t + \delta t)\,. \tag{2.21}$$

Now, to update the velocity, this algorithm requires first to deduce its value at $t + \delta t/2$ such as

$$v\left(t + \frac{\delta t}{2}\right) = v(t) + \frac{1}{2}\delta t a(t)\,, \tag{2.22}$$

and then after the full timestep:

$$v(t + \delta t) = v\left(t + \frac{\delta t}{2}\right) + \frac{1}{2}\delta t a(t + \delta t)\,. \tag{2.23}$$

The trajectories produced by this algorithm conserves the total energy E of the system during the time evolution. From a statistical point of view it produces, timestep after timestep, configurations that sample the microcanonical ensemble (NVE) for sytems with a constant number of atoms N and constant volume V. Several ensembles can be considered depending on the constraint we enforce on the system, for instance:

- The isothermal-isobaric ensemble (NPT) in which, the temperature T and pressure P of the system are maintained constant during the simulation thanks to the coupling with a thermostat and barostat, correspondingly. The number of atoms N is also fixed in this ensemble. Each configuration or state i occurs with a weighted probability

$$W_i = \frac{\exp\left(-\beta(E_i + PV_i)\right)}{\sum_j \exp\left(-\beta(E_j + PV_j)\right)} \tag{2.24}$$

  with E_i and V_i its energy and volume, respectively, and β the inverse temperature $1/k_B T$. The sum runs over all the possible configurations.

- The canonical ensemble (NVT) in which the volume V, number of atoms N, and temperature are fixed. This ensemble implies the use of a thermostat to conserve the

temperature. The weighted probability for a state i is

$$W_i = \frac{\exp(-\beta E_i)}{\sum_j \exp(-\beta E_j)}. \tag{2.25}$$

- The microcanonical ensemble (NVE) where the system's energy E is constant, then the weigthed probability does not depend on the configuration, leading to

$$W = \frac{1}{\sum_j \delta(E_j - E)}, \tag{2.26}$$

where the denominator counts the number of states j having the energy E.

- The grand canonical ensemble (μVT) which imposes a constant chemical potential μ, volume and temperature. This ensemble is usually sampled from Monte Carlo methods that allows the number of atoms to change. The weighted probability is then

$$W_i = \frac{\exp(-\beta(E_i + \mu N_i))}{\sum_j \exp(-\beta(E_j + \mu N_j))} \tag{2.27}$$

where N_i is the number of atoms in the state i.

2.3.1 | Principle of a Thermostat and Barostat

As was mentioned above, the temperature of the system is controlled and maintained by applying an external heat bath (thermostat) to the system. Numerous techniques have been proposed in MD to accomplish this objective [94]. The simplest, but not the most efficient, is the velocity rescaling, which modifies the particle velocity according to the desired temperature at the account of kinetic energy. More advanced methods used in MD simulations are, for instance, the Berendsen thermostat, introducing the strength of the coupling with the heat bath through a time-dependent constant. However, the most efficient in keeping the temperature constant is the Nosé–Hoover thermostat, that I have used for MD simulations within the powerful Large-scale Atomic/Molecular Massively Parallel Simulator (LAMMPS), which will be described below. The principle of the Nosé–Hoover thermostat, is that it introduces an additional degree of freedom coupled to the other ones of the system [95]. Then, the governing equation of an atom motion takes the form

$$m\frac{\mathrm{d}v}{\mathrm{d}t} = f(t) - \zeta(t)v, \tag{2.28}$$

where ζ is a coupling parameter that enters into the additional dissipative term that takes the form of a friction force. This dynamical quantity has a "mass" Q, modulating the strength

of the coupling with the atoms motion, and its time evolution follows

$$Q\frac{\mathrm{d}\zeta}{\mathrm{d}t} = \sum_i m_i \boldsymbol{v}_i^2 - 3Nk_BT\,. \tag{2.29}$$

The "force" acting on the thermostat variable is proportional to the difference between the instantaneous kinetic energy and the average kinetic energy $3Nk_BT/2$ following from the equipartition theorem. The same principle can be used to control the pressure (barostatting).

2.3.2 | LAMMPS

The simulation package LAMMPS [96], used in this work, is one of the most efficient parallel molecular dynamics codes besides GROMACS, NAMD and DL POLY. LAMMPS provides a wide choice of interaction potentials. Information on all the proposed diversity of methods for atomistic modelling is presented in its official website.

2.3.3 | Introduction to Force Fields

Moving on to a more detailed consideration, particular attention in MD simulations is paid to the choice of an empirical interaction potential that should provide an accurate description of the atomic interactions in order to produce a molecular model that is close to reality. There are many existing potentials for various materials and applications, all of which aimed at obtaining precise interactions in a fast way. A distinction is usually made between bonded, applied from paired to quartet particles, and non-bonded interactions, where atoms are unlinked or linked by more than three bonds, which are both used to get a proper description of intermolecular interactions.

The commonly used potential for non-bonded pair interactions adds the Lennard-Jones (LJ) and the Coulomb potential for two atoms i and j separated by a distance r_{ij} as

$$U_{LJ-C}(r_{ij}) = 4\epsilon\left[\left(\frac{\sigma}{r_{ij}}\right)^{12} - \left(\frac{\sigma}{r_{ij}}\right)^{6}\right] + \frac{q_i q_j}{4\pi\epsilon_0 r_{ij}}\,, \tag{2.30}$$

where the LJ parameters σ and ϵ, stand for the distance at which the potential cancel and the maximum depth of the potential well. The electrostatic potential introduces the charges q_i and q_j of the atoms and the vacuum dielectric permittivity ϵ_0. The LJ parameters for atoms with different LJ parameters are expressed through the Lorentz-Berthelot combining rule as follows

$$\epsilon_{ij} = \sqrt{\epsilon_i \epsilon_j} \tag{2.31}$$

and

$$\sigma_{ij} = \frac{\sigma_i + \sigma_j}{2} . \tag{2.32}$$

For the sake of saving computational time, a cutoff is used, after a given cutoff distance the interactions are disregarded. It should be noticed that to ensure correct interactions between particles in systems with periodic boundary conditions, the minimum image convention is employed to establish the interactions with their periodic images.

In this work, one of the advanced bond-order potentials, the Adaptive Intermolecular Reactive Empirical Bond Order (AIREBO) potential of Stuart [97], is used to properly describe the atomic interactions between the carbon and hydrogen atoms of kerogen, so that the mechanical properties of kerogen could be accurately modelled. It has been derived from the Reactive Empirical Bond Order (REBO) potential of Brenner [98] by including torsional and long-range (nonbonded) interactions which has allowed its wide use in molecular modelling carbon-based nanomaterials. Originally, the AIREBO potential has been fitted based on Density Functional Theory (DFT) / experimental values for hydrocarbons. This potential is represented in the form

$$U = \frac{1}{2} \sum_i \sum_{j \neq i} \left[U_{ij}^{REBO} + U_{ij}^{LJ} + \sum_{k \neq i,j} \sum_{l \neq i,j,k} U_{kijl}^{TORSION} \right] , \tag{2.33}$$

where U_{ij}^{REBO} is the Brenner's (REBO) potential determining short-ranged couplings between carbon and hydrogen atoms. Notably, this term of the AIREBO potential, defining the repulsion and attraction between two atoms, has remained unchanged from its initial form because of its accurate description of the covalent bonds between carbon and hydrogen. U_{ij}^{LJ} is the standard Lennard-Jones potential, covering longer range couplings according to the manually adjustable cut-off distance. Finally, $U_{kijl}^{TORSION}$ is a four-body potential describing different configurations of dihedral angles in a hydrocarbon system according to the bond weights that contribute to the dihedral angle. This torsional term allows a realistic description of carbon and hydrogen bonds.

The bond order principle used in the AIREBO potential counts several neighboring atoms to compute the short range atomic interactions, thus, providing a more accurate description of intra-molecular interactions accounting for the chemical diversity of carbon and hydrogen. The bond order between atoms i and j, contains three main terms corresponding to σ, π, and $\pi\pi$ bonding as follows

$$BO_{ij} = \exp\left[p_{bo,1} \left(\frac{r_{ij}^{\sigma}}{r_0} \right)^{p_{bo,2}} \right] + \exp\left[p_{bo,3} \left(\frac{r_{ij}^{\pi}}{r_0} \right)^{p_{bo,4}} \right] + \exp\left[p_{bo,5} \left(\frac{r_{ij}^{p\pi}}{r_0} \right)^{p_{bo,6}} \right] , \tag{2.34}$$

where the p_{bo}'s are calibrated parameters, and r_0 is the equilibrium bond length.

We used a slightly modified version of the AIREBO potential [2] in which the LJ parameters has been tune to precisely reproduce the equations of state for linear alkanes, with the idea of accurately determining the density of the kerogen model, a key quantity when studying adsorption-induced swelling. For carbon dioxide adsorbed in the kerogen models, a combination of the AIREBO potential and the Elementary Physical Model (EPM) potential proposed by Harris and Yung [99] through the hybrid pair style in LAMMPS has been used. The EPM model combines a rigid representation of the carbon dioxide molecules with LJ and Coulombic interactions.

The recent vectorized implementation of the AIREBO force field in LAMMPS by Höhnerbach and Bientinesi [100] has allowed to significantly speed up ($\sim \times 3$) the simulation of methane adsorbed in the kerogen model. However, this vectorized implementation in LAMMPS does not work with the hybrid pair style, therefore simulations with carbon dioxide have been three to four times slower than with methane.

Another force field close to the AIREBO potential, based on the bond order principle, is the reactive force-field (ReaxFF), developed by van Duin and co-workers [101] to properly describe chemical reactions. This reactive force field has been used to construct the kerogen models. Conversely, MD simulations of adsorption and diffusion have not been accompanied by formation or breaking of bonds, since the structures of kerogen are chemically stable.

2.3.4 | Classical MD Simulation Stages

Several stages of the MD simulation approach can be identified:

- The preparatory stage. Primarily, the construction of a molecular model should be performed. That implies the establishing of an initial configuration usually by creating a simulation box, inserting atoms and assigning some additional parameters such as the atom's charge if needed. In addition, all inter-/intra-molecular interactions must be defined through so-called force fields such as the classical Lennard-Jones (LJ) force field. Some examples of the construction and operation of a kerogen model will be considered in the next section.

- The preliminary stage. The imposition of simulation's conditions includes the choice of the ensemble, necessary dumped variables, etc. The simulation parameters vary broadly depending on the issues addressed by the present technique. To control the temperature and/or pressure the Nosé-Hoover thermostat and/or barostat is often applied during the MD run.

- The main stage. At this stage the MD simulation is launched and the model information selected in the previous stage is gathering during the MD run. The movement of particles and the generation of trajectories of atoms are accomplished by integrating Newton's equations of motion using the so-called Velocity-Verlet algorithm [102].

- The final stage is the post-treatment of the dumped information in order, for instance, to compute the properties of the molecular model.

2.4 | Replica Exchange Molecular Dynamics

Replica exchange molecular dynamics (REMD) or Parallel Tempering Molecular Dynamics (PTMD) [103] is an effective method for accelerating a long molecular simulation, especially when chemical reactions are involved. It has been used by [47] to build the mature model used in this work by reproducing the geological decomposition of lignin.

The basic idea of this method is to generate different replicas of the system at different temperatures and to periodically allow swapping between them in order to escape large free energy barriers at low temperature. The simulations of the replicas, meanwhile, are carried out in the NVT ensemble at temperatures, close to one another. Thus, the model can undertake only possible configurations during the MD simulation before reaching its thermodynamic equilibrium. In this way, the systems evolve very quickly even for the low temperatures at which the geological maturation of the organic matter occurs. Also, kerogen systems at various maturity levels can be obtained from a single run and a given organic precursor such as lignin, cellulose or fatty acids, for instance.

2.5 | Monte Carlo Simulations

In addition to MD simulation, Monte Carlo simulation is often used to study materials from various applications. Using statistical sampling as the basis, it had a convergence problem due to the large number of configurations involved. However, this has been overcome by introducing Markov chain processes which allow the system to move from one configuration to another by selecting the most probable configurations. This is possible thanks to the Metropolis algorithm which enables a new system's configuration by a simple random move followed by acceptance or rejection according to a set criteria. Compared to MD, it does not allow for the time evolution of the system, but rather yields its statistical properties.

To compute adsorption mimicking what could be obtained from experiments, the most widely used option in molecular simulations is to perform so called Grand Canonical Monte Carlo (GCMC) simulations [104], as done in this work. The reason is straightforward - the grand canonical ensemble provides a relatively natural environment for simulating adsorption by maintaining a constant volume and, more importantly, the temperature and chemical potential of the system. The idea behind GCMC is that in addition to allowing molecules to move, it permits the insertion or removal of molecules, which is established by an acceptability criterion.

2.6 | Atomistic Kerogen Models Construction

Studying transport properties requires realistic representations of organic source rocks. Since the generation of shale gas generally occurs in immature (H/C < 1.4) and mature kerogens (H/C > 0.4), in attempt to cover the majority of organic source rocks valuable for the hydrocarbons' extraction, kerogen models, one immature in the middle of the oil formation window (middle stage of catagenesis) and one mature, in the end of the gas formation window (late stage of catagenesis) are used in this work. The construction of the two models is briefly reviewed here. The mature model with methane adsorbed at various thermodynamic conditions is taken from [2] and the mature model loaded with argon was provided by Kévin Potier, PhD student under the supervision of Dr. Jean-Marc Leyssale (Theoretical Chemistry Group, Institute of Molecular Sciences, University of Bordeaux), during a research collaboration.

2.6.1 | Immature Kerogen Model

The molecular model of type I immature kerogen matrix shown in figure 1.2 has been used in this work to study the poroelastic couplings between the kerogen microscale porous structure and the adsorbed fluids that has been shown to be crucial because of adsorption-induced swelling [2].

Kerogen Model Construction

This microscale porous kerogen model has been developed by the liquid quench molecular dynamics technique [2]. This MD method compared to the REMD has allowed a rapid generation of a porous carbon matrix structure from a simply constructed crystal matrix of carbon and hydrogen by quenching it (heating the material to high temperature with subsequent rapid cooling). The density of the original model has been deliberately taken slightly larger (1.5 g/cm^3) than expected for the final model due to the fluid generation during quenching. Simulations have been run with a time step of 0.1 fs using a Nosé-Hoover thermostat with a 100 fs time constant. The temperature has been raised to 6000 K in the canonical ensemble while quenching to melt the crystal system, which has taken several tens of ps. This was followed by cooling to 300 K at a quench rate of 100 K/ps. The recent version of ReaxFF potential [105] has been used to describe the interactions between the carbon and hydrogen atoms.

Post-quench equilibration of the kerogen model has been performed using the AIREBO potential in order to reduce computational costs and allowing for an accurate modelling of the mechanical properties of the structure. Relaxation has been carried out in an isobaric-isothermal ensemble at temperatures that ranged from typical geological reservoirs (300 - 400 K) to a larger one (600 K) and at pressures ranging from 0.1 to 200 MPa. Depending on thermodynamic condition, the relaxation time has varied from 1 to 2 ns. The velocity-verlet

algorithm has been applied to integrate the equation of motion of the atoms. The temperature has been maintained using an Andersen thermostat [106] with a frequency parameter $4\,10^{-12}\mathrm{s}^{-1}$. Berendsen barostat has been applied with a coupling constant $4\,10^{2}\mathrm{Pa}^{-1}\mathrm{s}^{-1}$. for pressure.

The final version of the model has counted a total of 16864 atoms with an H/C ratio of 1.1 corresponding to a type I kerogen. The structure can be considered as well-ordered distinguishing it from kerogen at earlier catagenesis stage. For the sake of simplicity, the structure is only composed of carbon and hydrogen as it is believed that heteroelements entering the natural composition of kerogens like oxygen, sulfur and nitrogen in lower concentrations have a negligible impact on mechanical properties. A closer inspection of the chemical structure of the molecular model reveals that its texture is mainly composed of short aliphatic chains, containing 5 C atoms on average, and small aromatic ring clusters, containing 10 C atoms on average, with a balanced ring/chain ratio of 0.7. This leads to a "semi-flexible" matrix because of the inclusions of elements contributing to the stiffening (ring clusters) and to the softening (aliphatic chains) of the structure. Consequently, its bulk modulus is moderate ($\simeq$ 1-5 GPa) and consistent with type I immature kerogens. For geological conditions, the mechanical properties of the matrix decrease with the decrease of the pressure P, the increase of the temperature T and the fluid loading w [2].

Adsorption in the Kerogen Model

Grand Canonical Monte Carlo (GCMC) simulations have been performed before my work for the adsorption of methane in the immature kerogen model. First, methane in the form of a united atom has been adsorbed into the matrix, which has been maintained at the constant volume without accounting for flexibility effects. The corresponding LJ parameters used for adsorption simulations are given in [107]. The kerogen model at its maximum porosity (at 600 K, 0.1 MPa) has been taken for the GCMC simulations. A maximum fluid loading of 542 methane molecules has been obtained at high chemical potential. A total of 6 configurations with different adsorbed fluid amount have been produced. The number of adsorbed methane molecules considered varies from 80 to 542 molecules with the following fluid loading expressed in milligrams of fluid per gram of kerogen: 12.1 mg/g (80 molecules), 27.3 (180), 42.5 (280), 57.7 (380), 72.9 (480) and 82.4 (542). Then, an equilibration in the isobaric-isothermal ensemble with the AIREBO potential has been carried out while changing the fluid model from a united-atom one to a model representing all atoms of the methane molecules. It should be emphasized here that the mechanical pressure applied to the system do not correspond to any bulk fluid pressure since the amount of hydrocarbons adsorbed in the kerogens' microscale porosity results from the thermal degradation of the geologically buried organic matter and not from an equilibrium adsorption process as in a standard experiment. This differs from what has been done for the mature kerogen below.

For adsorption of carbon dioxide, I have replaced the methane molecules keeping the molar loading constant in each system of kerogen with methane. The following carbon diox-

ide loading has been obtained: 33.4 mg/g (80 molecules), 75.2 (180), 116.9 (280), 158.7 (380), 200.5 (480) and 226.4 (542). The models have been then relaxed in the isobar-isothermal ensemble allowing the kerogne matrix to relax, where temperature and pressure have been controlled by the Nosé-Hoover thermostat and barostat, respectively. A small-time step of 0.01 fs has been chosen for the first few tens of ps to avoid loss of fluid molecules from the simulation box due to their stronger interaction with the solid and proximity to each other. After that, the time step has been increased to 0.1 fs and the simulation has taken from a few ns to a few tens of ns (to 70 ns for the lowest fluid loading) depending on the kerogen model to reach equilibrium, obtaining the volumetric swelling corresponding to the adsorption of carbon dioxide.

According to the increase in the fluid amount, volumetric characteristics such as porosity (volume fraction not occupied by the matrix atoms), free volume (volume fraction not occupied by the matrix and fluid atoms) and swelling have changed in the flexible matrix due to poroelastic couplings. All volume characteristics for both kerogen models, immature and mature, and their impact on transport are discussed in chapter 3.

2.6.2 | Mature Kerogen Model

The second molecular model used in this work to study the adsorption-induced swelling effects on transport is the mature kerogen model of type III obtained by REMD [37]. This microscale porous mature kerogen model has a size of about $4 \times 4 \times 4$ nm^3 and is shown in figure 2.1.

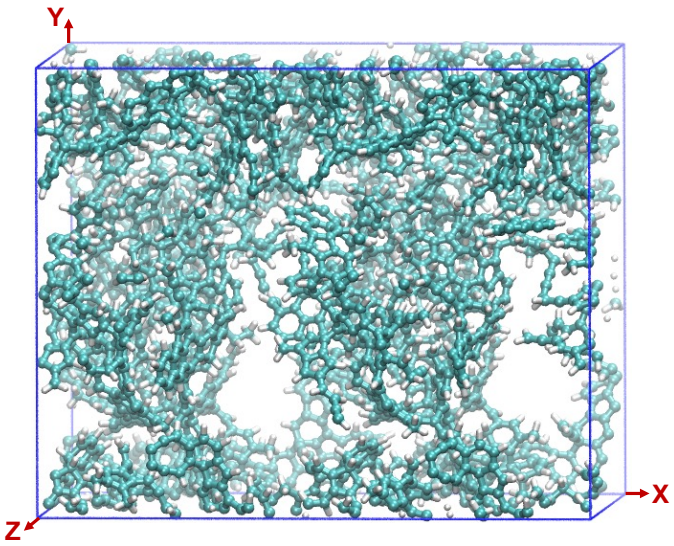

Figure 2.1 | Snapshot of the microscale porous carbon model equilibrated at 243 K and zero pressure. cyan: C; white: H.

Kerogen Model Construction

The lignin taken from [108] has been chosen as a kerogen precursor to build a mature kerogen model. It represents 18 oligomers of the softwood lignin model with the following compositional characteristics: O/C = 0.34 and H/C = 1.11. Placed in an orthorhombic box, it has been equilibrated at 423 K and 25 MPa in the isothermal-isobaric ensemble with Nosé-Hoover and Nosé-Hoover-Andersen thermostat and barostat, respectively, for about 100 ps. The ReaxFF force field has been used to account for all inter- and intramolecular interactions. A time constants of 0.5 ps has been taken for the thermostat. The equations of motion are integrated using the velocity-Verlet algorithm with a 0.1 fs time step.

After that, the REMD simulations have been performed in the canonical ensemble using 96 replicas of the lignin model with temperatures ranging from 423 to 3500 K, where replica exchange between the temperatures has been attempted every 10 fs. A relaxation run every 200 ps has been conducted to more accurately mimic the geological decomposition of lignin. In total, it has taken about 1.3 ns to reach chemical equilibrium at 423 K from the REMD simulations. At the end, fluid has been removed from the lignin-based matrix and the matrix has been equilibrated at 423 K, 25 MPa for 1 ns.

The obtained kerogen model has undergone some changes. First of all, the 15 oxygen-containing groups, mostly hydroxyl, were replaced by equivalent oxygen-free groups (H for OH and CH_2 for ether O). After that, the model was duplicated in the shorter periodic direction (X in figure 2.1). The final kerogen matrix contains 2754 carbon atoms and 1364 hydrogen atoms enclosed in an orthorhombic cell of $\sim 48 \times 39 \times 34$ Å^3, with periodic boundary conditions in all directions. Only carbon and hydrogen were retained in the matrix to account all the interactions by the AIREBO potential with the reparameterization proposed by Obliger et al. [2]. The H/C ratio, 0.495, defines modelled kerogen as belonging to the type III (mature), implying a dominant aromatic structure. Detailed structure analysis reveals that carbon atom hybridizations, determined from the numbers of the closest neighbors, are 87.4 % sp^2, 7.9 % sp^3 and 4.7 % sp (or radical sp^2). Texture analysis shows that 83.4 % of the carbon atoms are involved in ring clusters, with an average cluster size of 33 C atoms (9 rings) while the remaining atoms form small chain structures (2 atoms on average). Rings are predominantly hexagons (51 %), pentagons (34 %) and heptagons (9 %).

Adsorption in the Kerogen Model

Initially, the lignin-based matrix has been relaxed using MD in isobaric-isothermal ensemble at 243 K and zero pressure for 600 ns. The argon adsorption simulations were performed at 243 K and for pressures in the 0.05–2116 bar range by using an hybrid NPT-MD/μVT-GCMC scheme where the chemical potential imposed during the GCMC simulations correspond to a bulk fluid pressure equal to the pressure applied during the NPT simulation (unjacketed adsorption condition). 1000 MC runs of 250 000 trials and 1000 MD runs of 100 ps were performed. In addition, GCMC was performed in combination with

NVT runs thus preventing any volume change bu allowing for the mechanical relaxation of the kerogen microscale structure (jacketed adsorption condition), 3000 GCMC runs of 250 000 trials (argon insertion or deletion) and 3000 MD runs of 100 ps were performed. Finally, GCMC alone has been also used by considering the matrix rigid, thus not allowing for swelling and mechanical relaxation. 1000 MC runs of 250 000 trials were performed.

2.7 | Numerical Procedures to Evaluate Transport Properties

Fluid diffusion within flexible kerogen has been investigated in [7] for the molecular model, emphasizing on the importance of the adsorption-induced swelling phenomenon, but only for a few thermodynamic conditions, and for a few nanoseconds thus limiting the study to the self-diffusion coefficients. This limitation was caused by the use of a homemade MD code with a correct implementation of the AIREBO potential as opposed to its initial implementation in the LAMMPS package. This has been corrected by [100] proposing a vectorized and parallelized implementation of AIREBO that is particularly efficient.

2.7.1 | Immature Kerogen Model

We take advantage of these performances to explore a larger diversity of thermo-mechanical conditions (temperature, pressure) and longer simulations times to obtain accurate estimations of the self-diffusion coefficients and even investigate collective diffusion coefficients that could not be investigated before. Besides to the typical geological T/P, temperature and pressure above (500 K and 100 MPa, correspondingly) and below (300 K and 0.1 MPa, correspondingly), this range of conditions were considered.

As the matrix with methane only consist in carbon and hydrogen atoms, the description of inter- and intra-molecular interactions during MD) simulations is carried by the modified AIREBO potential. The AIREBO potential has proved to be highly realistic to describe a large number of carbon-containing molecular models. The long range part of the AIREBO potential has been slightly modified in [2] to reproduce more accurately the equation of states of linear alkanes. This reparameterization was motivated by the fact that the density of the kerogen structure is the key quantity controlling the properties of the molecular structure. The simulating of kerogen with adsorbed carbon dioxide is performed using the AIREBO (for solid-solid interactions) and Lennard-Jones (for fluid-fluid interactions) potentials while accounting solid-fluid interactions with the Lorentz-Berthelot combining rules [109].

In order to generate the trajectories, all-atoms MD calculations of the kerogen model with adsorbed fluid have been performed in the canonical ensemble with a timestep of 0.25 fs. The Nosé-Hoover thermostat was used to control the temperature following [110] with a

damping parameter of 0.4 ps. Three-dimensional periodic boundary conditions have been applied during the simulations. The constant volumes enforced during the MD trajectories at various conditions (temperature, pressure, loading) come from the results obtained in the isothermal-isobaric ensemble (NPT) and are taken from [2]. Despite rigorously equilibrated volumes, it has taken longer trajectories for systems with the lowest fluid quantities. The total time for the lowest fluid loading (12.1 mg/g) therefore have amounted to 50 ns instead of 10 ns for larger fluid loading. The detailed description of the relevant transport equations was discussed previously (see section 2.6.2).

2.7.2 | Mature Kerogen Model

Similarly to the flexible kerogen model, the integration timestep for all MD simulations amounts to 0.25 fs. However, the used time constant for the temperature in the three-member Nosé-Hoover chain method is 0.1 ps and for the pressure tensor in the anisotropic Nosé-Hoover barostat is 0.5 ps which is distinct from the mature model.

The self-diffusion coefficient (D_s) is obtained from the slope of the time evolution of the a Mean Square Displacement (MSD) of the argon molecules over the three directions x, y, and z using MD simulations in the NVT ensemble. For this, five independent configurations from each of the adsorption simulation schemes described above (NPT-GCMC, NVT-GCMC and RIGID) are taken at six different gas pressures, from 1.44 to 2116 bar, as initial configurations. The simulations are run for 6 ns, where after 100-200 ps the linear regime for the MSD is approximately reached.

CHAPTER 3

Fluid Transport Properties in Organic Source Rocks

Contents

3.1 | Introduction

Two atomistic models of kerogen are used here to study the transport of fluids in organic matter's microscale porosity. The immature one stands in the middle of the oil formation window and the mature one at the end of the gas formation window. They were both described in section 2.6. The variety of pore size/affinity/connectivity introduced in the kerogen atomistic models provides pathways for fluid flow and may accelerate as well as slowdown the motion of fluid molecules which is poorly documentated especially for swellable nanoporous media. In addition, characterizing immature kerogen flexibility effects could strongly contribute to the fluid transport increase. For instance, the transport in the immature kerogen model is associated with the adsorption-induced volume expansion as illustrated in figure 3.1. These effects as well can be crucial for more mature kerogens. The outlined issues together with the impact of kerogen's flexibility on the transport nature are not well understood and will be addressed in the current chapter.

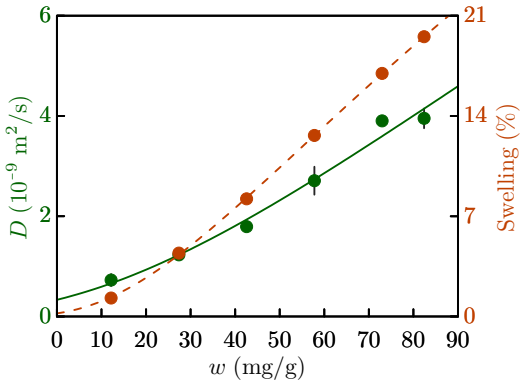

Figure 3.1 | Evolution of the self-diffusion coefficient (green) and the volumetric swelling (red) with the methane loading w, in milligram of fluid per gram of the solid matrix, at a temperature of 400 K and a mechanical pressure of 25 MPa within the flexible model of type I kerogen.

Another important aspect of the MD study of transport using atomistic models of kerogen is the size of the modelled matrix. Experiments revealed that shales' organic matter is anisotropic at the macroscopic scale [111, 112]. However, while anisotropy is crucial at the macroscale and could emerge at the microscale from size effects, the amorphous nature of the porous material at the mesoscale implies isotropic structural disorder [113]. Thus, the representativeness of the kerogen models is also raised here.

Thus, the present chapter is organized as follows:

- The first section synthesizes the structural/textural characteristics of the two used models of kerogen at different thermal maturity level, immature and overmature.
- In the second section a collective diffusion investigation is shown for the flexible immature kerogen matrix for two fluids, methane and carbon dioxide.

- The third section introduces a study of the anisotropy of transport induced by the size of the kerogen models.
- In the fourth section the diffusion of methane and carbon dioxide accounting for the poroelastic coupling between the kerogen matrix and the fluid is compared with reference to the first section to better understand the volume/structural effects on transport.

3.2 | Pore-Volume Characteristics of Kerogen Models

Since the effect of solid's flexibility on transport is the focus of the thesis, the porosity characterization for immature and overmature kerogen models with adsorbed fluids is given here. The pore-volume analysis for mature type III kerogen swollen upon argon adsorption and the atomistic configurations were provided by Kévin Potier, PhD student under the supervision of Dr. Jean-Marc Leyssale (Theoretical Chemistry Group, Institute of Molecular Sciences, University of Bordeaux), during a research collaboration. The porosity and free volume ratio are evaluated following the procedures described below for immature kerogen loaded with methane and carbon dioxide from equilibrated configurations under various temperatures (300, 400 and 500 K for methane, 300 and 400 for carbon dioxide) and mechanical pressures (0.1, 25 and 100 MPa).

3.2.1 | Numerical Methods to Compute Porous Properties

The porosity of the kerogen structures is calculated by considering randomly inserted dimensionless points in the simulation box. The ratio of number of positions that do not get into the C/H atoms of the kerogen matrix against the total number of positions is used to obtain the porosity and the free volume ratio if we also discriminate the points lying into the fluid molecules. The atoms are considered as spheres with diameters taken to be their Lennard-Jones parameters of the corrected AIREBO force field reused in this work: 3.36 and 2.42 Å for carbon and hydrogen atoms, respectively. Fifty thousands random trials are typically needed to reach convergence. The volumetric swelling is simply calculated by comparing the volume of the methane-containing matrix with the volume of the empty kerogen matrix at the same temperature-pressure conditions.

For the accessible quantities (porosity and free volume ratio) taking into account the volume of a fluid molecule to ensure free space for the fluid, a collection of spheres ($2.5\ 10^5$) with a diameter of 3.73 and 3.3 Å corresponding to the Lennard-Jones parameter of methane and carbon dioxide, respectively, both considered as a single interaction site that fits into the pore volume is first generated. Then, the accessible porosity is sampled by checking

the ratio of random points lying in this collection of spheres. The accessible free volume ratio is estimated by subtracting the volume of the adsorbed fluid molecules. Knowing the accessible porosity allowed to obtain the pore occupancy for methane loaded immature kerogen, expressed as the ratio of the volume occupied by the fluid to the porous volume available for its adsorption.

3.2.2 | Results and Discussion

Here we present porous properties described in section 2.6.1 for the kerogen models of type I and type III. The influence of kerogen maturity, fluid type, adsorption-induced swelling, temperature and pressure on volume and porous structure changes is discussed. While the used mature model is adsorbed with argon, in the immature one different fluids, methane and carbon dioxide, are considered, the latter of which is adsorbed by replacing methane, at the same molar loading. This section also studies the microscale structural deformations caused by this process.

Methane Loaded Type I Immature Kerogen

Contrary to the organic matter models considered as rigid, the matrix flexibility allows for the pore enlargement with the temperature increase and pressure decrease as it is shown for immature kerogen in figure 3.2.

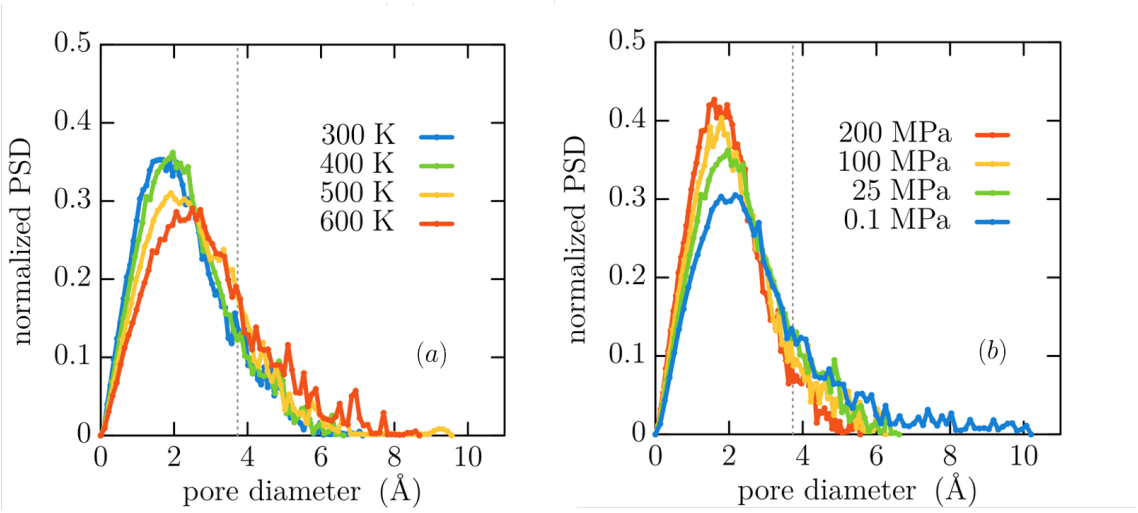

Figure 3.2 | Pore size distributions (PSD) of the empty immature matrix with (a) temperature at 25 MPa and (b) pressure at 400 K and are taken from [2]. The dashed grey vertical line indicates the diameter of the methane molecule (3.73 Å). The PSD was produced using a method based on a search for the center of the largest-diameter sphere proposed by L. D. Gelb and K. E. Gubbins [8]. 3×10^5 sphere centers and 2×10^5 pore locations were used.

The volume increase of the flexible kerogen model with fluid adsorption is shown in figure 3.3. The maximum swelling at the typical geological condition for adsorbed methane is 20 % that corresponds to the reported value from MD studies [114]. Apart from the fluid loading important for a high-volume change, thermo-mechanical (T-P) conditions also significantly impact adsorption-induced matrix swelling. Their influence on the pore space increase confirms the previously reported direct and inverse relations for temperature and pressure respectively [7], besides, the models expand or shrink more due to the temperature than pressure variations within investigated conditions. Moreover, it is indicative that the linear dependence is more pronounced at the elevated temperature and the volume does not much evolve for the same fluid loading at low temperature over all variations of applied mechanical pressure.

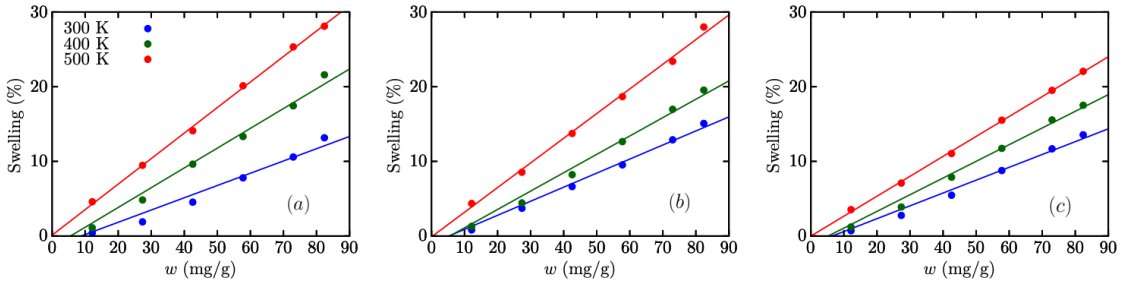

Figure 3.3 | Evolution of CH_4 adsorption-induced swelling as a function of fluid loading w expressed in milligram of fluid per gram of solid matrix at temperatures of 300, 400, and 500 K, and pressures of (a) 0.1 MPa, (b) 25 MPa and (c) 100 MPa. The solid curves stand for linear models of the swelling evolution.

The adsorption-induced swelling of the methane loaded kerogen model unambiguously leads to the increase in the total porosity thanks to the pore enlargement which is promoted by the flexibility of the solid (figure 3.4). At maximum fluid loading, it reaches ∼ 52 % at the typical geological condition. To assess porosity values during fluid adsorption for this type of organic matter, for instance, the small-angle neutron scattering technique is available due to its accessibility to pores at the microscale [115]. This is crucial for this microscale porous material as the increase in pore space is still significant (∼ 40 %) even for an ultra confining condition (300 K, 100 MPa).

The free volume takes into account the volume occupied by the adsorbed fluid molecules thus reducing the available volume in the kerogen microscale porosity. For instance, it occupies 5 % less porous space at a mild condition (400 K, 25 MPa) for the most swollen case (figure 3.5). Moreover, the dependence of the free volume on the fluid amount is ambiguous. At temperature and pressure conditions not favorable for the matrix expansion kerogen models show the inverse trend or almost constant free volume values with the fluid adsorption.

However, this is not the case for the shown accessible porous properties which capture the rise in porous space with CH_4 adsorption for all thermodynamic conditions (figure 3.19

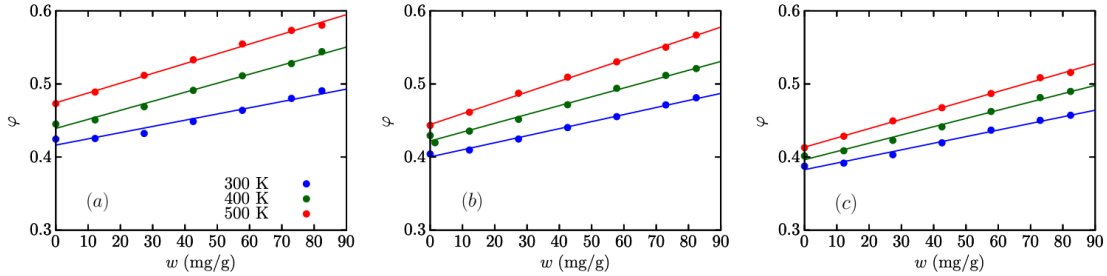

Figure 3.4 | Evolution of the total porosity for CH_4 as a function of fluid loading at pressures of (a) 0.1 MPa, (b) 25 MPa and (c) 100 MPa. The solid curves stand for linear models of the total porosity evolution.

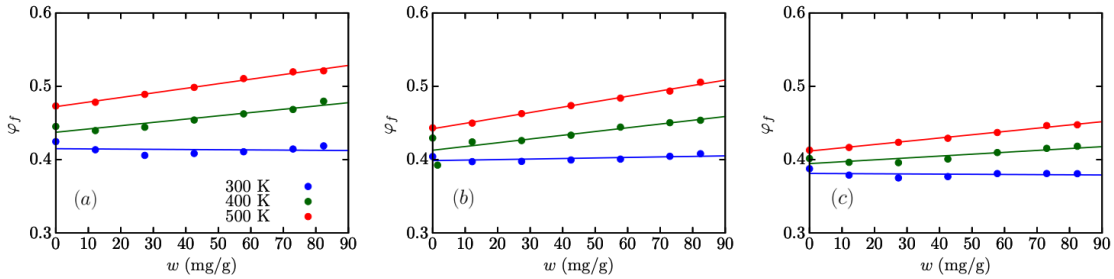

Figure 3.5 | Evolution of the free volume for CH_4 as a function of fluid loading at pressures of (a) 0.1 MPa, (b) 25 MPa and (c) 100 MPa. The solid curves stand for linear models of the free volume evolution.

and 3.5). Although these porous characteristics manipulate the volume that can be occupied by CH_4 molecules, they have values an order of magnitude smaller than the regular ones.

The reason of the decreasing trend of the free volume evolution with methane adsorption at highly confining conditions could be explained by the pore occupancy ratio shown in figure 3.8. Despite the flexibility of the matrix, the fluid occupies more kerogen pores under stronger confinement, thereby reducing the free volume.

It is worth emphasizing that whereas in the case where external pressure leads to a strong increase in kerogen permeability, as in hydraulic fracturing, and hence to fluid diffusion/release [116], our study is more relevant to the case where a decrease in the pore size of an equilibrated matrix under applied pressure hinders fluid movement which for instance corresponds to a geological process such as rocks bedding.

Carbon Dioxide Loaded Type I Immature Kerogen

The density change over simulation time after methane replacement by carbon dioxide and its equilibrium fluctuations are shown in figure 3.9 for the lowest fluid content at the typical geological condition (400 K, 25 MPa) and slightly below (300 K, 25 MPa). The density fluctuations caused by matrix volume relaxation for the lowest fluid content at a pressure of 0.1 MPa and temperatures of 300 K and 400 K are shown in appendix A.

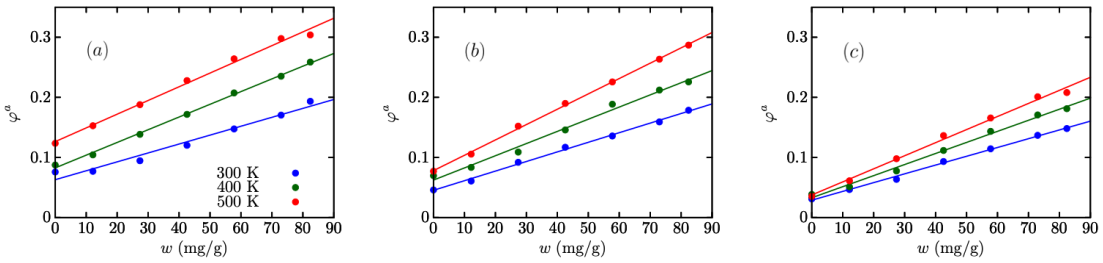

Figure 3.6 | Evolution of the accessible porosity with the CH_4 loading for the three different temperatures at pressures of (a) 0.1 MPa, (b) 25 MPa, (c) 100 MPa. The solid curves stand for linear models of the accessible porosity evolution.

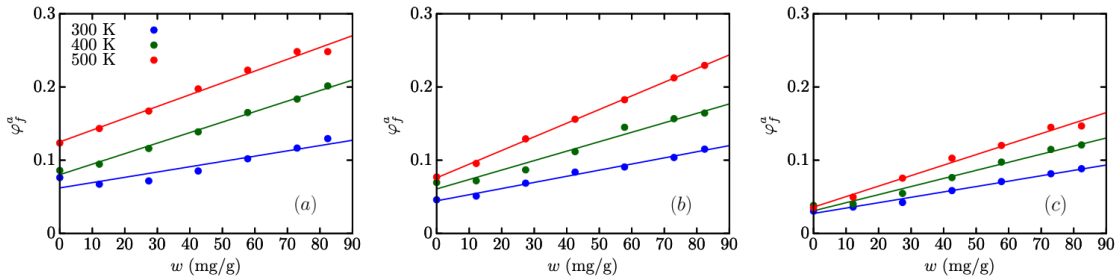

Figure 3.7 | Evolution of the accessible free volume ratio with the CH_4 loading for the three different temperatures at pressures of (a) 0.1 MPa, (b) 25 MPa, (c) 100 MPa. The solid curves stand for linear models of the accessible free volume evolution.

Kerogen swells significantly upon carbon dioxide adsorption as shown in figure 3.10. This volume expansion is more pronounced with increasing temperature increase at low pressure (0.1 MPa), while at moderate applied mechanical pressure it is weak which may be due to the fact that these thermodynamic conditions are close to the critical point of carbon dioxide (∼304 K, 7 MPa), which probably causes surface effects. At even stronger applied pressure, the volume increase with temperature remains important.

However, the total porosity increases due to adsorption-induced swelling markedly with increasing temperature for the entire range of confining pressures investigated (figure 3.11).

As can be seen from the figure 3.12, the free volume strongly decreases with minimal adsorption of carbon dioxide in the empty solid matrix, which is associated with strong adsorption effects with this type of fluid. Compared to the mentioned pore volume characteristics, the free volume does not yield a clear trend towards an increase in carbon dioxide adsorption under all variations of thermodynamic conditions. At more favorable for the expansion of the pore space confining pressures (0.1 MPa and 25 MPa) the linear evolution of the free volume with adsorbed carbon dioxide is maintained, discarding the case with the smallest amount of fluid. On the contrary, ultrahigh pressure (100 MPa) changes this linear trend with high fluid adsorption. The porous properties computed by considering the volume available to the fluid show clear trends of the adsorption-induced swelling

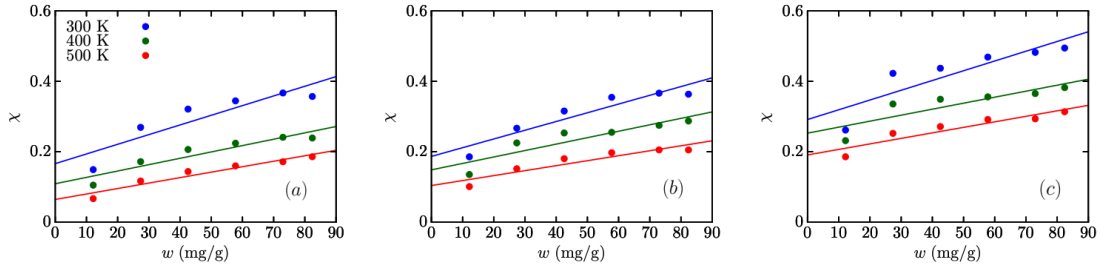

Figure 3.8 | Evolution of the pore occupancy ratio with the CH_4 loading for the three different temperatures at pressures of (a) 0.1 MPa, (b) 25 MPa, (c) 100 MPa. The solid curves stand for linear models of the pore occupancy evolution.

increase in pore space (figures 3.13 and 3.14. The dependence of porous characteristics on temperature and pressure is also reflected clearly over a wide range of conditions.

To compare the behaviour of models swollen with different fluids, the fluid loading is introduced in millimoles of fluid per gram of solid. It bears underlining that the matrix shrinks due to the presence of carbon dioxide in relation to that with adsorbed methane (figure 3.15). At the minimum fluid molecules amount carbon dioxide tends to contract the volume of the system, conversely to methane. This phenomena can be explained by the high energetic density of carbon dioxide molecules reinforcing solid-fluid interactions. Interestingly, that it is particularly pronounced at the typical geological condition and high fluid loading ($>$ 12.1 mg/g). However, at other conditions the shrinkage is stronger at low fluid content due to the predominating fluid adsorption to the solid walls which induces the volume decrease of the empty matrix.

The maximum swelling at the typical geological condition for adsorbed carbon dioxide (figure 3.15) is less (in 3 %) than for methane which is the opposite to that for the bulk fluid state. As for the kerogen model with adsorbed methane, the matrix volume does not undergo significant swelling with confining pressure at low temperature.

Switching to the carbon dioxide slightly affects the matrix total porosity in reducing its values due to a more constrained environment caused by significant solid-fluid interactions (figure 3.16).

The potential volume for carbon dioxide adsorption having greatly reduced values than those for methane adsorbed models tends to rise for more swollen models except the case with the lowest porosity condition (300 K, 100 MPa) at which the values are almost not changing for both fluids (figure 3.17).

The values of the porosity accessible for carbon dioxide adsorption are higher than that for kerogen with methane (figure 3.19), having more potential to the fluid adsorption.

However, taking the same methane probe for both matrices gives compatible evolution of the accessible porosity (figure 3.19).

The volume accessible to the fluid (figure 3.20) is also larger for carbon dioxide but remaining slightly smaller for both kerogen models while accounting for an adsorbed fluid.

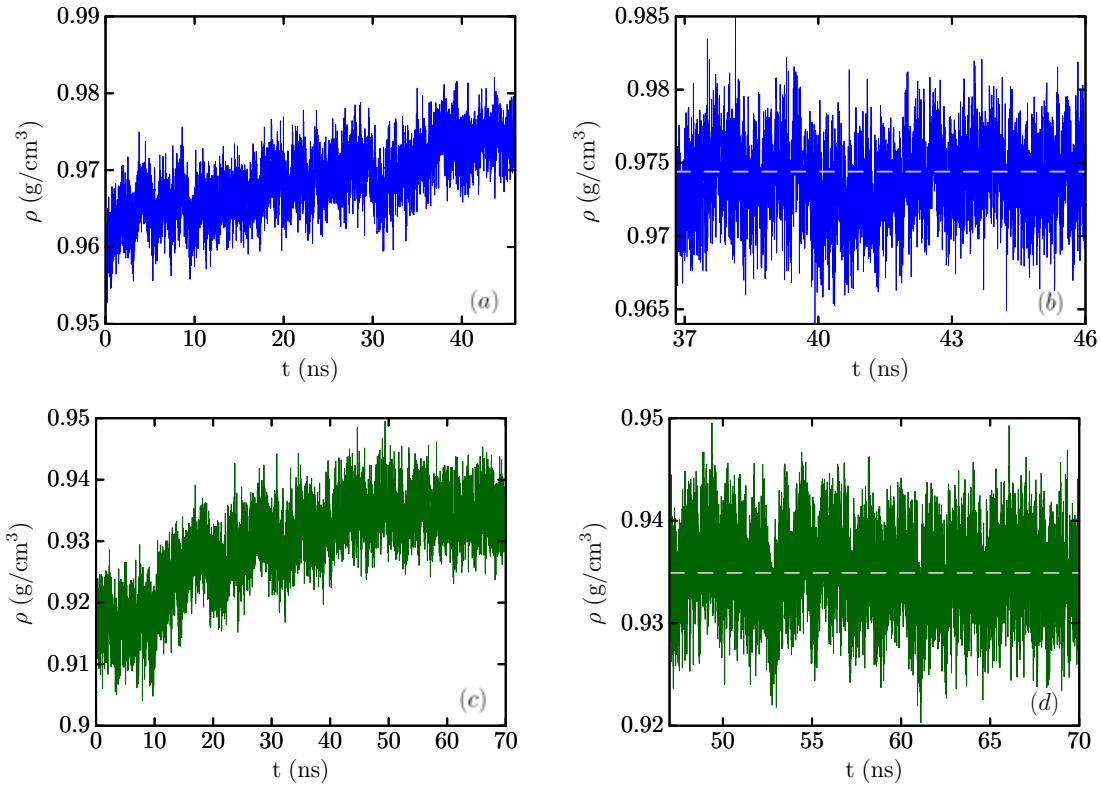

Figure 3.9 | Density evolution of the kerogen matrix during NPT MD simulation after per-molecule replacement of 80 CH_4 molecules with CO_2 molecules at a pressure of 25 MPa and temperatures of (a) 300 K and (c) 400 K and the corresponding density fluctuations of the equilibrated matrix volume – (b) and (d). Dotted lines in (b) and (d) show the average density value.

Moreover, the values deviate more broadly in comparison to the accessible porosity for a variety of thermodynamic conditions. Again, using the same methane probe for both matrices gives compatible evolution of the accessible free volume ratio (figure 3.21).

This feature allows a better description of the increase in pore volume properties and therefore the present quantity is chosen for the free volume modelling proposed to capture the transport increase due to the adsorption-induced swelling, which is discussed in the next chapter.

Non-Affine Deformations Induced by CH_4/CO_2 Replacement

The reinforced solid-fluid couplings when replacing methane with carbon dioxide at a wide range of thermodynamic conditions induce significant matrix restructuring. The internal solid's reorganization and volumetric deformations could be characterized by non-affine displacements due to the amorphous nature of the carbon matrix. In the past, the spatial correlations of nonaffinity at the nanoscale upon deformation strain were revealed in a solid glass [117–119] and microscale porous kerogen [2] models.

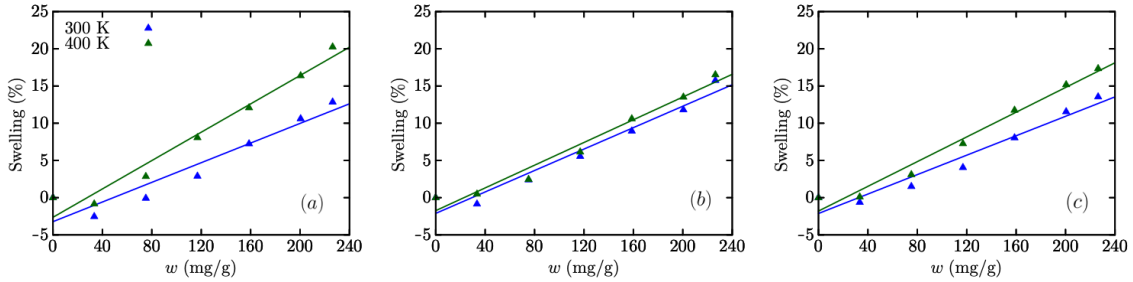

Figure 3.10 | Evolution of CO_2 swelling as a function of fluid loading w expressed in milligram of fluid per gram of the solid matrix at temperatures of 300 and 400 K and pressures of (a) 0.1 MPa, (b) 25 MPa and (c) 100 MPa. The solid curves stand for linear models of swelling evolution.

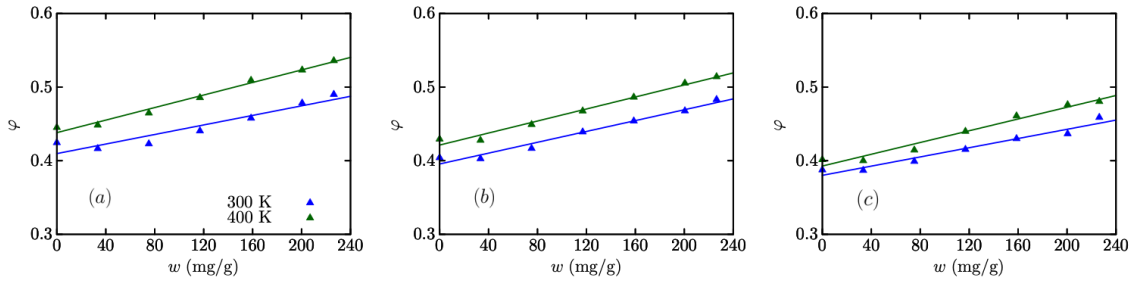

Figure 3.11 | Evolution of the total porosity for CO_2 as a function of fluid loading at pressures of (a) 0.1 MPa, (b) 25 MPa and (c) 100 MPa. The solid curves stand for linear models of CO_2 total porosity.

To capture both types of deformations, resulting from volume changes and rearrangement of matrix atoms, methane is substituted with carbon dioxide, while allowing matrix volume adaptation after this process (at constant pressure) and allowing only internal kerogen restructuring (at constant volume). The i-component (i = x, y or z) of the non-affine displacement u^{na} is defined through the averaged displacement of atoms and the affine deformation as:

$$u_{\mathrm{i}}^{\mathrm{na}} = r_{\mathrm{i}}^{\mathrm{new}} - r_{\mathrm{i}}^{\mathrm{old}} - u_{\mathrm{i}}^{\mathrm{a}} \tag{3.1}$$

where the affine displacement u^{a} is expressed in components as

$$u_{\mathrm{i}}^{\mathrm{a}} = r_{\mathrm{i}}^{\mathrm{old}} \frac{L_{\mathrm{i}}^{\mathrm{new}} - L_{\mathrm{i}}^{\mathrm{old}}}{L_{\mathrm{i}}^{\mathrm{old}}} \tag{3.2}$$

where $L_{\mathrm{i}}^{\mathrm{new}}$ and $L_{\mathrm{i}}^{\mathrm{old}}$ are the final and initial averaged matrix length, correspondingly. As shown in equation 3.2, the matrix with only allowable internal deformations does not cause affine displacements.

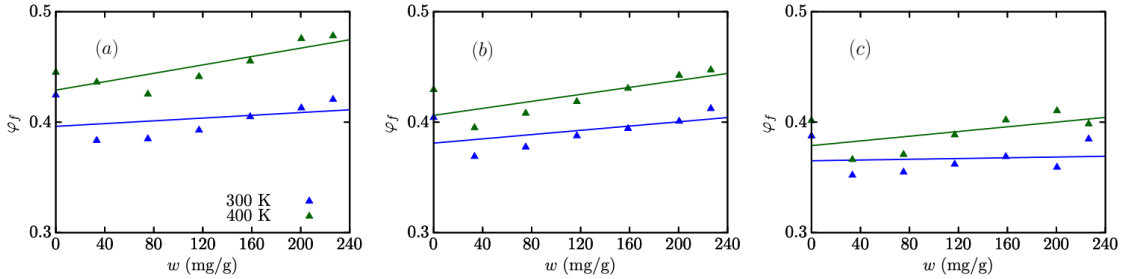

Figure 3.12 | Evolution of the free volume for CO_2 as a function of fluid loading at pressures of (a) 0.1 MPa, (b) 25 MPa and (c) 100 MPa. The solid curves stand for linear models of CO_2 free volume.

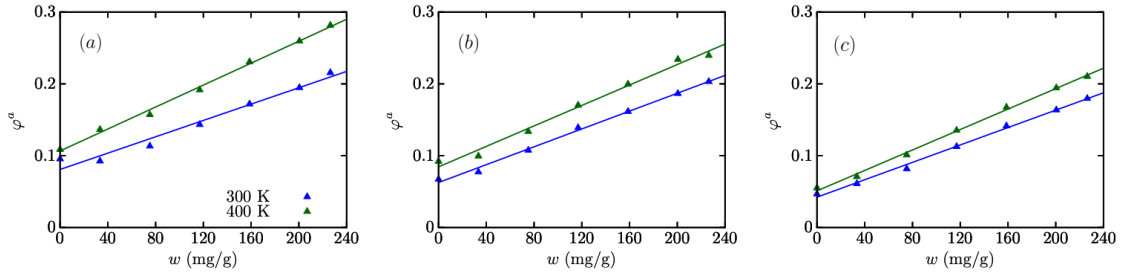

Figure 3.13 | Evolution of the accessible porosity with the CO_2 loading for the three different temperatures at pressures of (a) 0.1 MPa, (b) 25 MPa, (c) 100 MPa. The solid curves stand for linear models of the accessible porosity.

Systems with carbon dioxide substituted molecules at the maximum loading are considered at its initial and equilibrated states where one of the matrices is relaxed at the fixed initial volume corresponded to the equilibrated kerogen matrix with methane and another one - at the volume which may adapt to the presence of carbon dioxide. The solid's atoms positions are taken with respect to the center of kerogen mass for each model as averaged over 5 blocks of 600 ps and in time. For the sake of simplicity and better representativity, we consider only the carbon atoms of the solid (8032 C) and its displacements in the x and y Cartesian directions.

The deformations induced by the movement of solid atoms and volume change upon the fluid replacement are illustrated in figure 3.22 where colors are indicating the norm of the total non-affine displacement from its minimum (dark blue) to maximum (light yellow) amplitude. Adapting the volume to this change (figure 3.22 (a)) causes relatively large non-affine displacements compared to these only caused by internal rearrangements of kerogen atoms (figure 3.22 (b)). In addition, the systems show local geometric ordering which could be probed by computing the radially averaged scalar product as a function of radius.

Disregarding natural organic matter's volume contraction/swelling also leads to under-/overestimation of the transport coefficient. For instance, the diffusion of carbon dioxide is

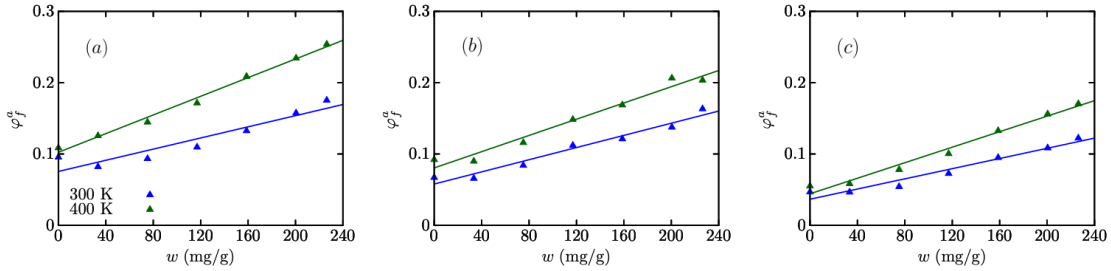

Figure 3.14 | Evolution of the accessible free volume ratio with the CO_2 loading for the three different temperatures at pressures of (a) 0.1 MPa, (b) 25 MPa, (c) 100 MPa. The solid curves stand for linear models of the accessible free volume.

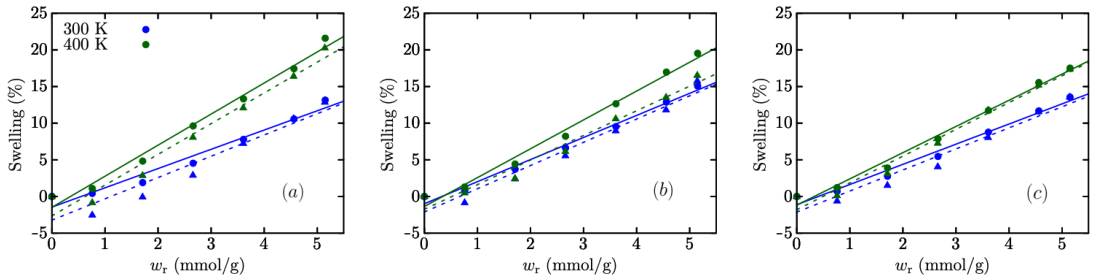

Figure 3.15 | Evolution of swelling for CH_4 (circles) and CO_2 (triangles) as a function of fluid loading at pressures of (a) 0.1 MPa, (b) 25 MPa and (c) 100 MPa. The curves stand for linear models of swelling evolution for CH_4 (solid lines) and CO_2 (dotted lines).

faster (3.29×10^{-9} m^2/s instead of 2.71×10^{-9} m^2/s) while neglecting volume deformations after CH_4 replacement by CO_2 at the maximum loading. Thus, accounting solid's flexibility is of critical importance in studying geological processes, such as CO_2 sequestration in organic matter.

The non-affine displacements correlation in disordered porous materials is characterized by various decay laws, such as exponential and power-law. The normalized Probability Distribution Function (PDF) for the non-affine deformations induced by NVT/NPT relaxation of the carbon dioxide loaded kerogen matrix is plotted in figure 3.23. For both cases, large deformations' distribution can not be captured by a Gaussian distribution, as it is the case for small displacements, while they follow a power-law decay. Overall, the PDF follows a Gaussian law for the small displacements and a power law for the largest ones, thus, providing a description of the non-affine deformations correlation in the complex microscale porous organic matter model. Such deviations from a Gaussian behaviour for large displacements indicate that important internal reorganizations in the matrix are spatially correlated.

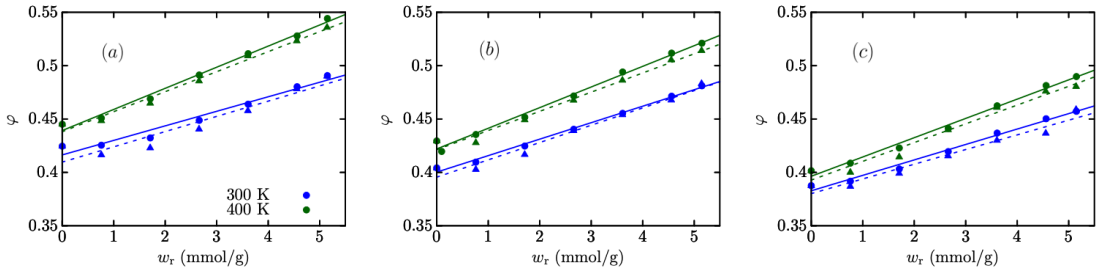

Figure 3.16 | Evolution of the total porosity for CH_4 (circles) and CO_2 (triangles) as a function of fluid loading at pressures of (a) 0.1 MPa, (b) 25 MPa and (c) 100 MPa. The curves stand for linear models of CH_4 (solid lines) and CO_2 (dotted lines) total porosity.

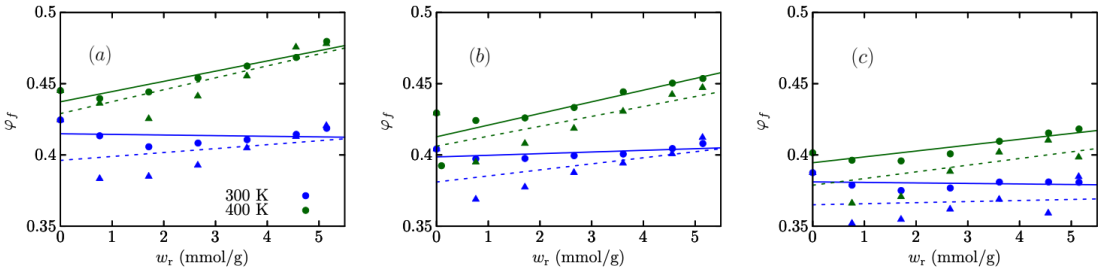

Figure 3.17 | Evolution of the free volume for CH_4 (circles) and CO_2 (triangles) as a function of fluid loading at pressures of (a) 0.1 MPa, (b) 25 MPa and (c) 100 MPa. The curves stand for linear models of the free volume evolution for CH_4 (solid lines) and CO_2 (dotted lines).

Argon Loaded Type III Mature Kerogen

The reported average accessible porosity for the mature kerogen model amounts to 0.330 ± 0.007 which is almost one order of magnitude higher despite the smaller size of the representative matrix than for the immature kerogen model and relatively low applied temperature. The average pore size of 7.09 ± 0.09 Å is also larger than in the type I kerogen model, the pore size fluctuations lie in the range of 3.4 Å (Ar probe size) – 11 Å.

Three different adsorption simulation strategies based on the MC simulations in the grand canonical ensemble (GCMC) (see section 2.6.2) were used to investigate the impact of the matrix flexibility, covering both adsorption-induced swelling and internal matrix restructuring on solid-fluid couplings.

Allowing matrix volume change leads to the volumetric strain (swelling) up to about 10 % at a low temperature of 243 K and for mechanical pressure up to 2116 bar. However, the mechanism of swelling induced porous space increase differs from that for immature kerogen. This is also caused by different applied adsorption techniques to these systems. Similarly to the type I kerogen model, the matrix seems to contract at very low fluid adsorption, despite the poor statistics.

The evolution of the accessible porosity, free volume and pore occupancy ratio χ of

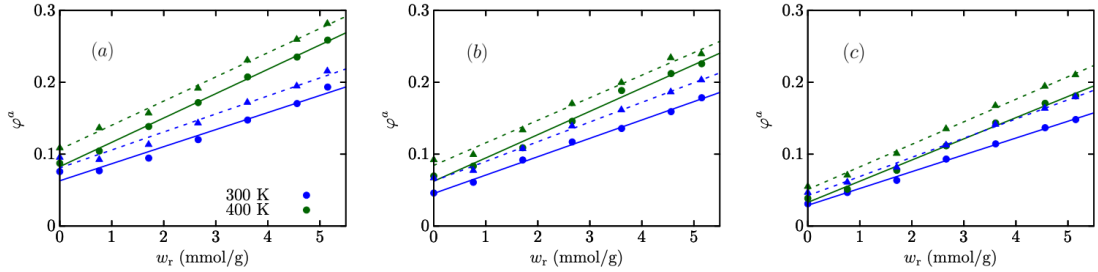

Figure 3.18 | Evolution of the accessible porosity with the CH_4 (circles) and CO_2 (triangles) loading at pressures of (a) 0.1 MPa, (b) 25 MPa and (c) 100 MPa computed using a spherical probe with a diameter of carbon dioxide. The curves stand for linear models of the accessible porosity evolution.

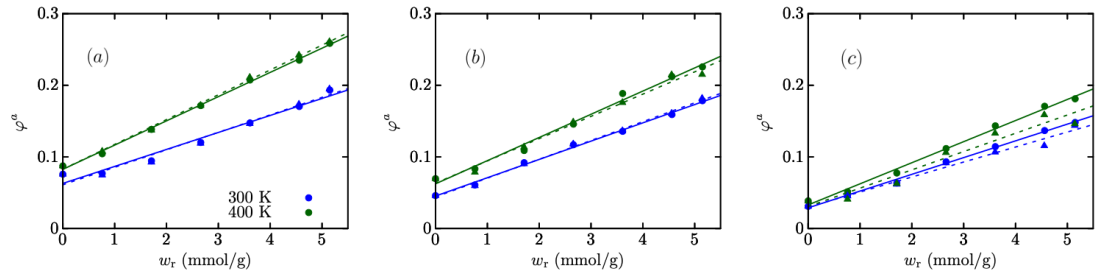

Figure 3.19 | Evolution of the accessible porosity with the CH_4 (circles) and CO_2 (triangles) loading at pressures of (a) 0.1 MPa, (b) 25 MPa and (c) 100 MPa computed with the same (methane) probe. The solid curves stand for linear models of the accessible porosity.

the mature kerogen matrix with argon pressure is illustrated in figure 3.24. The latter, as mentioned above, is simply the ratio of the volume occupied by fluid molecules adsorbed in the matrix to the porous volume potentially accessible to fluid adsorption. While the accessible porosity evolution (from $\backsim$0.33 to $\backsim$0.41) with argon adsorption at the fluid pressure follows an increasing trend, the free volume shows an inverse trend (from $\backsim$0.33 to $\backsim$0.22) because of the pores occupation by fluid molecules. As can be seen in figure 3.24, argon molecules weakly occupy the matrix pores at low pressure values up to 1 bar, whereas at stronger applied pressure χ increases sharply, indicating important matrix restructuring and volume expansion, which, however, does not contribute to the free volume, as for the immature kerogen model under ultra-confining conditions (figure 3.5).

Overall, volumetric swelling as well as internal solid's flexibility shows a great impact on the porous volume and structure change during the fluid adsorption in both immature and mature kerogen models. The significant fluctuations of pore size and internal mobility of solid atoms may affect fluid-fluid correlations which is discussed in what follows.

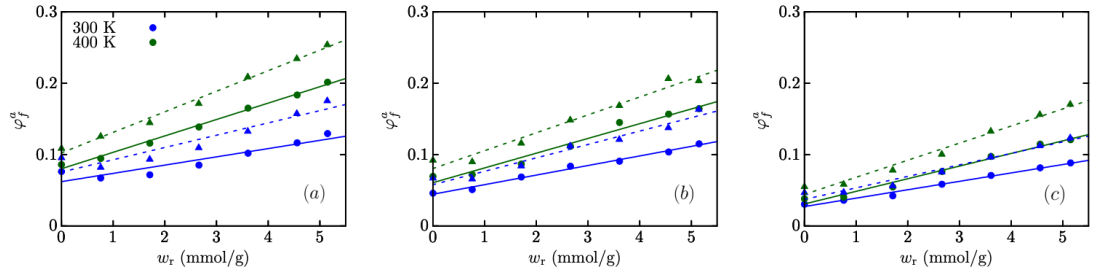

Figure 3.20 | Evolution of the accessible free volume ratio with the CH_4 (circles) and CO_2 (triangles) loading for the three different temperatures at pressures of (a) 0.1 MPa, (b) 25 MPa, (c) 100 MPa computed using a spherical probe with a diameter of carbon dioxide. The curves stand for linear models of the accessible free volume evolution.

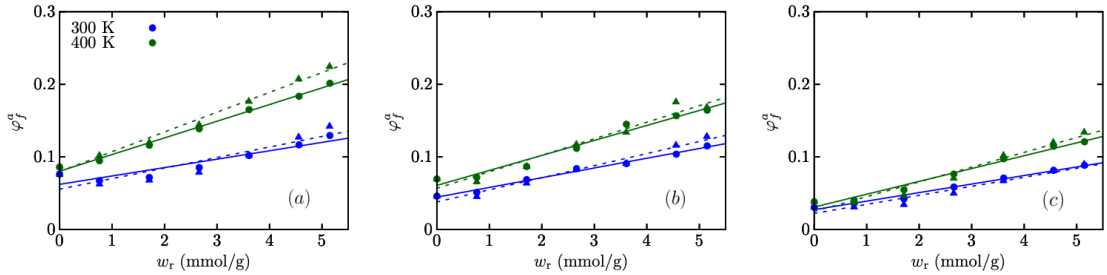

Figure 3.21 | Evolution of the accessible free volume ratio with the CH_4 (circles) and CO_2 (triangles) loading for the three different temperatures at pressures of (a) 0.1 MPa, (b) 25 MPa, (c) 100 MPa computed with the same (methane) probe. The curves stand for linear models of the accessible free volume evolution.

3.3 | Collective Diffusion in Kerogen Flexible Microporosity

As has been shown in section 3.2, microporous kerogen models from immature to over-mature types exhibit considerable swelling due to fluid adsorption. Although the mechanism of volumetric and internal restructuring of the swollen solid matrix depends on its formation stage, the kerogen poroelasticity/flexibility inherent throughout the kerogen variety, may play an important role in the nature of fluid transport while promoting/hindering collective fluid-fluid correlations. Neglecting fluid-fluid cross-correlations have been justified for the rigidified kerogen matrix [6, 14, 68]. In the present section we shed light on this aspect for the first time while accounting for the poroelastic coupling.

Since pore elasticity and expansion are manifested more strongly at early stages of kerogen thermal evolution, collective effects impacting the long term diffusion process are investigated in the framework of the liquid-quench kerogen model constructed to study the flexibility effects. The model involves two fluids with different energetic densities, methane

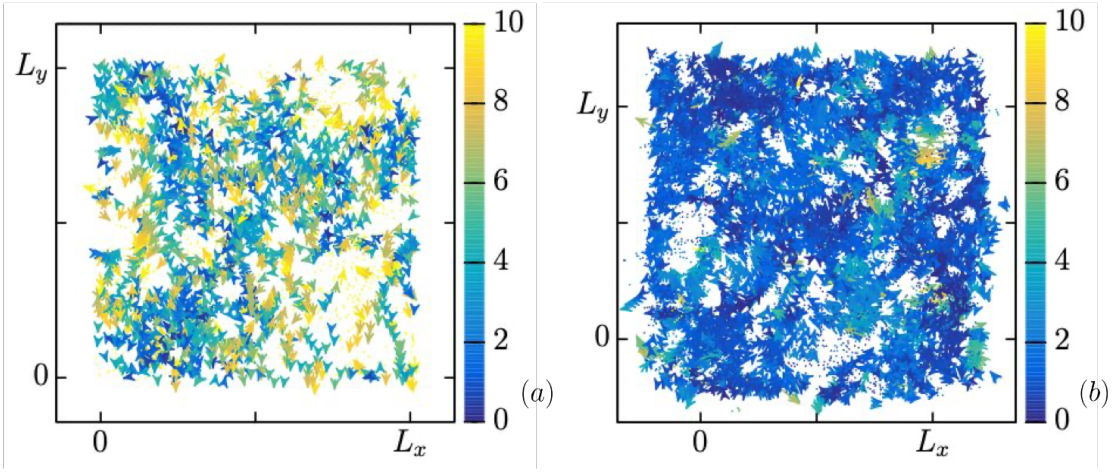

Figure 3.22 | Projection on the (x, y) plane of the non-affine displacement of the carbon atoms of the solid matrix. Arrows are rescaled with a scaling factor of 0.01 and are colored according to the norm of the non-affine displacements for the matrix equilibrated in (a) the NPT ensemble and (b) the NVT ensemble.

and carbon dioxide, at the pressure of a typical geological reservoir condition (25 MPa) over the temperature range in order to cover their supercritical states. The typical reservoir temperature (400 K), above (500 K) and below (300 K) are considered for collective methane diffusion, whereas the least representative temperature for the shale gas basin (500 K) is not included for carbon dioxide transport study. Nonetheless, modelling conditions for carbon dioxide, which forms a stronger coupling with the solid, involve a T-P range closer to its critical point ($\backsim$304 K, 7 MPa).

Quantification of the impact of solid's flexibility on collective effects is achieved by comparing the collective and self-diffusion coefficients which are distinguished by the cross correlation terms mentioned previously (equation 2.17). By independently tracking the displacement of each fluid molecule with respect to the matrix c.o.m., an approximately linear regime can be reached after a few hundred picoseconds. However, taking into account the fluid c.o.m. is more time-consuming, an approximately linear MSD trend is achieved in a few nanoseconds as illustrated for methane in figure 3.25. Thus, a trajectory of up to 10 ns is post-processed to calculate diffusivity of both fluids, and up to 50 ns to compute its collective diffusion coefficients. In addition, simulations are run for 5 different initial configurations to assess the computational accuracy.

The evolution of the self- and collective diffusion coefficients with adsorbed methane is shown in figure 3.26 for a temperature of 300 K, 400 K and 500 K and a pressure of 25 MPa. The kerogen models take into account the kerogen's viscoelastic nature. When adsorption-induced swelling is important under constant mechanical pressure, the increase of fluid loading is accompanied by an increase in accessible free volume (figure 3.7) that enhances diffusion. It is noteworthy that both the self- and collective diffusion coefficients are within the error bars of the latter for the investigated range of thermodynamic conditions.

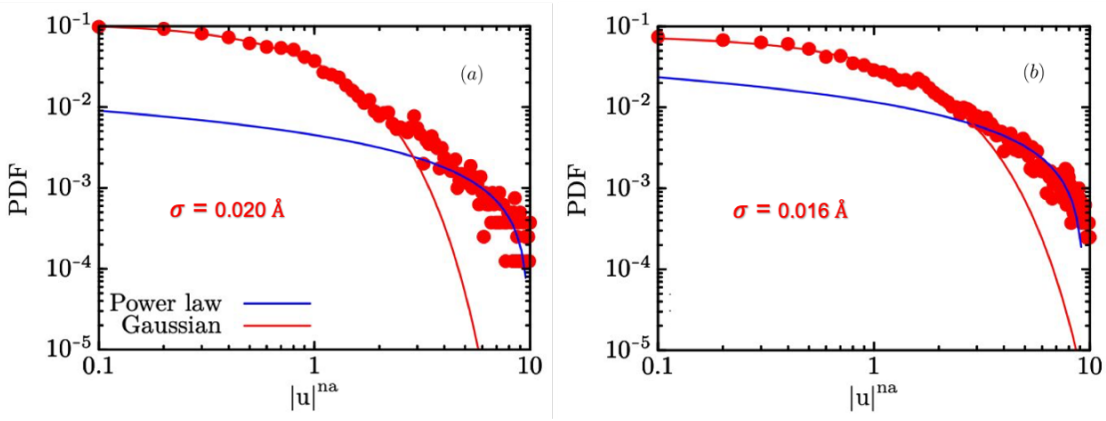

Figure 3.23 | PDF of the non-affine displacements for the matrix equilibrated in a) the NPT ensemble and b) the NVT ensemble. The red curves correspond to a Gaussian function and the blue ones to a power law, both adjusted to the numerical data.

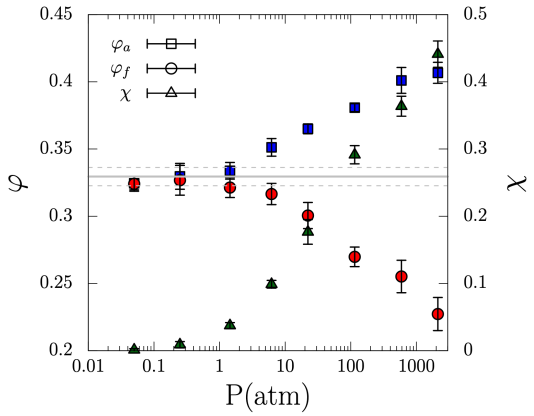

Figure 3.24 | Evolution of the accessible porosity (φ_a), free porosity (φ_f) and pore occupancy ratio (χ) with the argon bulk pressure using the hybrid NPT/GCMC method. φ_a at zero pressure is indicated with horizontal lines (thick line: mean; thin lines: standard error).

We can conclude from figure 3.26 that at a temperature of 300 K the trends are the same for both diffusion coefficients. The collective and self-diffusion coefficients should also follow the same increasing trends at a high temperature of 500 K because the difference between these transport coefficients should vanish in the infinite dilution limit. For a moderate pressure of 400 K, despite the ambiguous trend, the collective diffusion coefficient evolution should also be similar to the diffusivity, as there is no reason for it to differ from temperatures of 300 K and 500 K. The mean square displacements for the methane center of mass from single trajectories at a temperature of 400 K are illustrated in figure 3.27. We can, consequently, state that the evolution of both transport coefficients have the same increasing trends with the adsorbed fluid for the wide range of thermodynamic conditions studied in this section.This therefore leads to the fact that the cross-correlations between

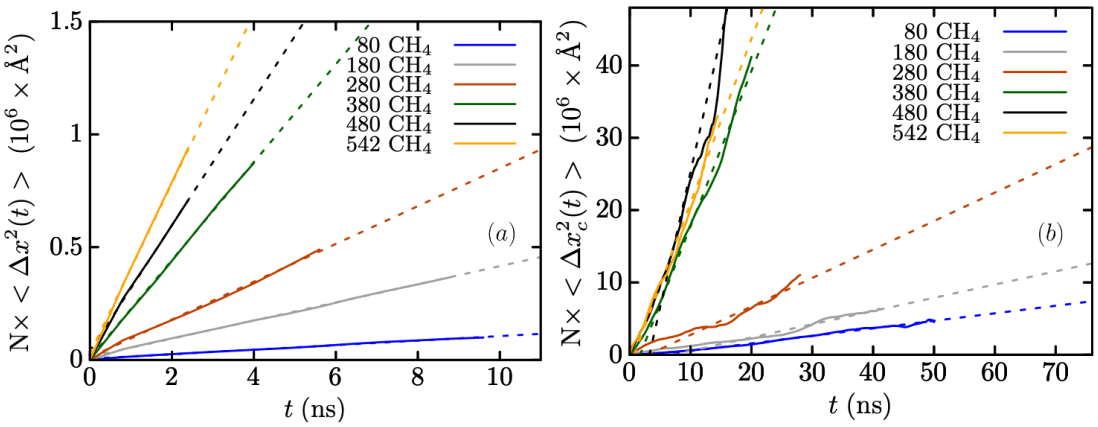

Figure 3.25 | Time evolution of the MSD of the fluid molecules (a) and the fluid c.o.m (b) multiplied by the number of fluid molecules, N (indicated in the color code), for single trajectories at a temperature of 400 K and a pressure of 25 MPa. The dashed lines correspond to the linear fits used to evaluate the self- and collective diffusion coefficients for the minimum and the maximum loading.

fluid molecules (cross terms in equations 2.17 and 2.18) do not significantly contribute to the collective diffusion coefficient.

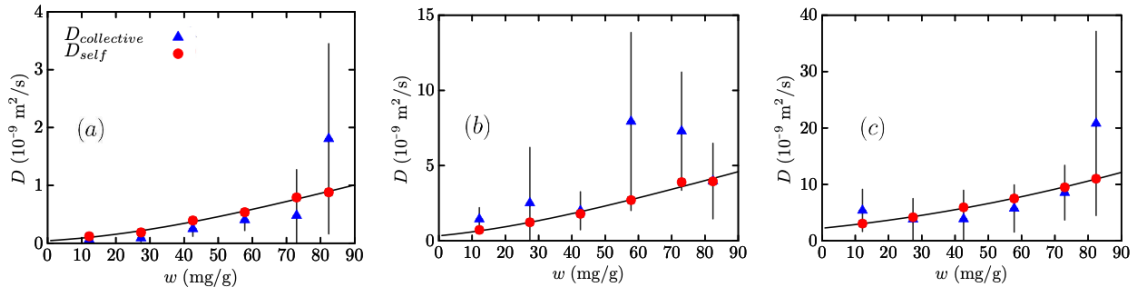

Figure 3.26 | Self- and collective diffusion coefficients as a function of methane loading for a confinement pressure of 25 MPa and three different temperatures: (a) 300 K, (b) 400 K and (c) 500 K. Larger error bars for the collective diffusion coefficients stems from the fact that only the c.o.m. of the fluid can be tracked from an MD trajectory instead of all amount of fluid molecules (ranging from 80 to 542 for the lowest to the highest loading) in the case of the self-diffusion coefficient. Solid curves aid to see the increasing trend.

Referring to the porous properties' characterization (section 3.2), carbon dioxide contracts the matrix at low fluid loading compared to methane at the same molar loading. On top of greater than for the adsorbed methane interaction with kerogen, the investigated fluid state near its critical point can affect cross-correlations between fluid molecules. It can be stated, though, that both transport coefficients of carbon dioxide shown in figure 3.28 as a function of fluid loading for a temperature of 300 K and 400 K and a pressure of 25 MPa are approximately the same confirming the totally diffusive nature of fluid transport in flexible kerogen matrices. Similar to methane diffusion, the increase in transport is clearly reflected

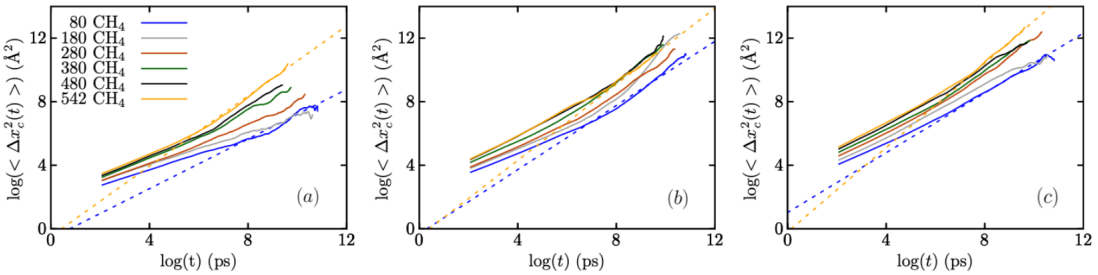

Figure 3.27 | Time evolution of the MSD of the fluid c.o.m in log-log scales for different loadings indicated in number of molecules N (color code), for single trajectories at temperatures of 300 K, 400 K and 500 K and a pressure of 25 MPa. The dashed lines correspond to the linear fits used to evaluate the collective diffusion coefficients for the minimum and the maximum loading.

for the coldest temperature, which reaffirms the common tendency of fluid diffusion to increase with the pore volume growth.

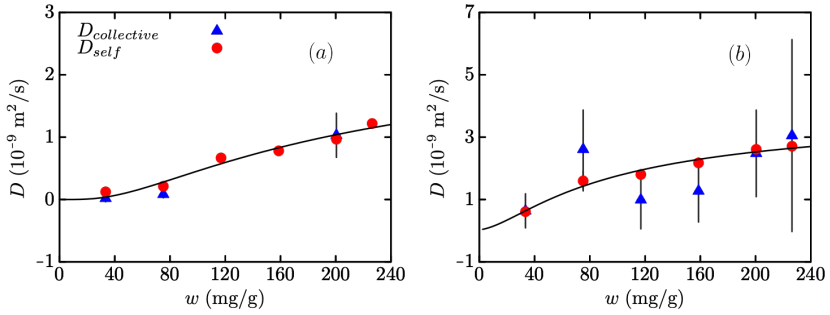

Figure 3.28 | Self- and collective diffusion coefficients as a function of carbon dioxide loading for temperatures of (a) 300 K and (b) 400 K and a pressure of 25 MPa.

Following the above comparative analysis, the promotion of cross-correlations thanks to solid's flexibility effects is not confirmed even for a more energetically dense fluid (carbon dioxide) near its critical point. This means that mature kerogen will most probably not assist fluid-fluid interactions. In a broader sense, fluid transport is purely diffusive with negligible collective effects within a microporous solid which encompasses all variety of kerogens from the middle of the oil formation window to the end of the gas formation window. Based on our findings and studies on mixture's diffusion [5, 14], we suggest, that this statement should be valid for fluids of interest in practical applications, such as light alkanes, carbon dioxide and water, as well as for their mixtures. However, this may be limited for the case of some ionic and/or larger fluid molecules. Nevertheless, we expect collective effects to be negligible in a highly disordered porous material providing a strong confinement for the fluid.

The physical meaning of obtained trends of transport coefficients is as follows: diffusion within kerogen is not affected by long-range hydrodynamic couplings since only individual

trajectories' information captured by the self-diffusion coefficient is needed. It has been recently proven [6,14] that fluid transport is purely diffusive in kerogens' microstructures arbitrarily treated as rigid, thus by neglecting both the adsorption-induced swelling and the matrix dynamics. The approximation of fully rigid kerogen microporosity may be only relevant for extremely mature kerogens. However, the majority of kerogens exhibits viscoelastic behaviour and, consequently, the atomistic models of kerogens' microporosity should be able to deform during MD calculations. Here we show for the first time that, while matrix flexibility plays a significant role on fluid transport, diffusion increases due to adsorption-induced swelling as opposed to the rigid behaviour where the shared porous volume remains constant as the fluid loading increases, the impact of the motion of the kerogen matrix do not promote significant cross-correlations between fluid molecules during diffusion within flexible matrices.

From the computational point of view, there is no need to calculate the collective diffusion coefficient that requires very long trajectories, thus effectively saving computational time since diffusion or transport can be studied by focusing on the self-diffusion properties only.

3.4 | Anisotropy in Transport Properties

While modelling nanoscale fluid dynamics in organic matter, anisotropy effects could significantly affect transport properties which have been reported in several works [120,121]. Since performing all-atoms MD calculations for atomistic models of kerogen is greatly time-consuming, the size of the systems studied is limited to a few nanometers. Size effects can arise due to this limitation complicating the understanding of the coarse-grained transport picture. Moreover, as the transport mechanism in microporous kerogen is locally dominated by the solid-fluid interactions due to the strong adsorption effects we specifically turn our attention to anisotropic effects. We verify here on the two atomistic models of kerogen - lignin based and flexible kerogen - with a different size and the ability to deform, if they lead to anisotropic transport properties.

3.4.1 | Type I Immature Kerogen

The inherent poroelasticity of kerogen at the nanoscale, as well as adsorption effects and fluid molecules' aggregation near the solid-fluid interface, may enhance the anisotropy. Though our kerogen atomistic model of about $6 \times 6 \times 6$ nm^3 is already quite large, it still has slightly anisotropic transport properties. Figure 3.29 shows the self-diffusion coefficient of methane over the x, y and z directions for a pressure of 25 MPa and different temperatures (with similar results for the other conditions, see appendix A).

We note that diffusion along the y direction stands out of diffusion in the two other directions that remains very similar while increasing the fluid loading. In order to quantitatively estimate this trend against the amount of adsorbed fluid molecules, we introduce the

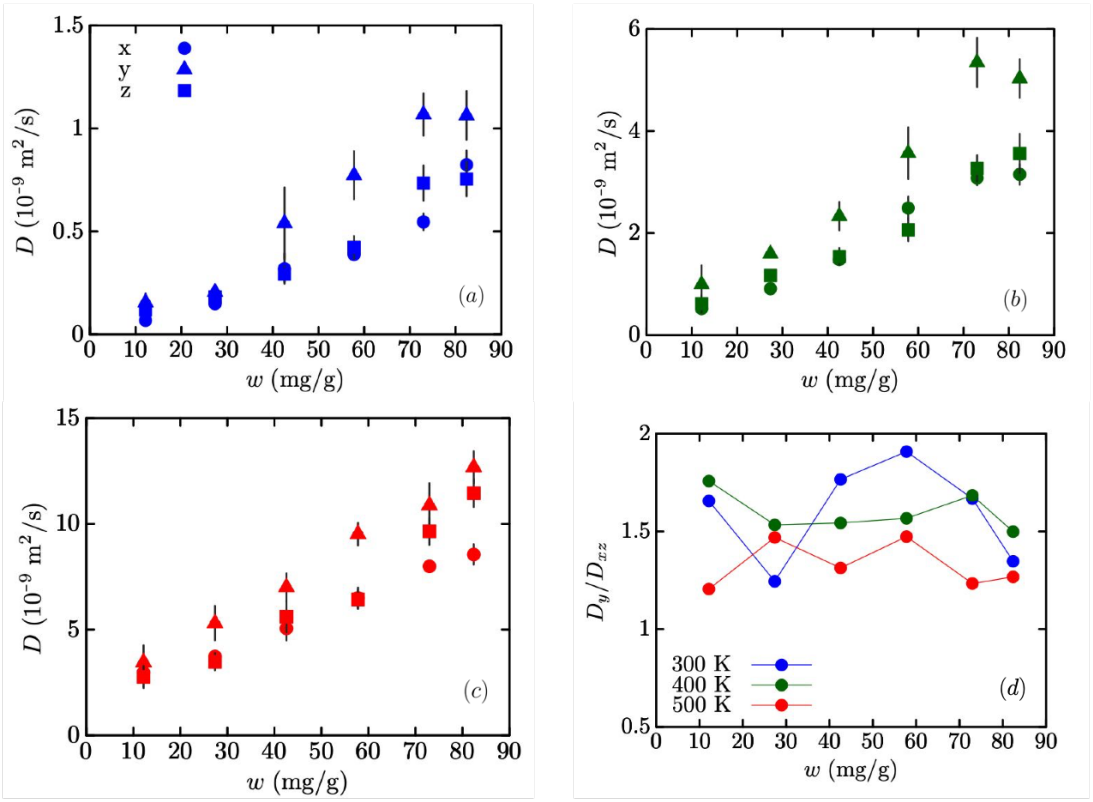

Figure 3.29 | Methane self-diffusion coefficients along the x, y and z directions at temperatures of 300 K (a),400 K (b) and 500 K (c) and at a pressure of 25 MPa (left) and anisotropic factor (d) defined as the ratio of the diffusion coefficient in the y direction over the average diffusion coefficient in the two other directions (right) as function of the fluid loading for three different temperatures and a pressure of 25 MPa.

anisotropy factor defined as the ratio between the self-diffusion coefficient in the y direction and the averaged self-diffusion coefficient over the two other directions x and z. As can be seen in figure 3.29, the anisotropy factor is approximately constant as function of the fluid loading and remains moderate (< 2) without any observable temperature effect. Then, even if the transport properties can differ in one direction, their behaviour with the fluid loading and thus with the adsorption-induced swelling is very similar. Since a small atomistic model designed to perform MD calculations cannot reproduce the true heterogeneity of the kerogen's microporous network trapped in a particular hydrocarbon reservoir, averaging the absolute value of slightly anisotropic diffusion coefficients does not represent a problem as long as the trends investigated are not impacted. Consequently, the transport properties of the kerogen matrix, averaged over the three directions, can be considered isotropic. From that, the atomistic model of kerogen with a typical size of 6 nm can be used to derive a transport model even if the absolute values of the diffusion coefficients can slightly differ over the directions. Additionally, we provide the per-component D_s and anisotropic factor for another condition and fluid type (carbon dioxide) in appendix A.

3.4.2 | Type III Mature Kerogen

As shown in figure 3.30, size effects are important in the ∼4 nm length size mature kerogen model. Allowing adsorption-induced swelling the mature kerogen matrix leads to strikingly demonstrated anisotropy in all directions, except for extremely low/high pressure where the anisotropy has the preferential z direction. It means that in the wide pressure range (6-114 bars) this model shows significant anisotropy induced by the constructed initial configuration of the kerogen model and flexibility contributing to the heterogeneity of the structure at the nanoscale. Similar anisotropic behaviour occurs in the flexible model where swelling is neglected. However, the range of kerogen models with close diffusivity values in the x and y directions expands indicating a significant reduction in the influence of matrix poroelasticity by considering only internal deformations. The rigid treatment of the kerogen matrix leads to less pronounced anisotropic transport properties due to the absolute neglect of matrix flexibility.

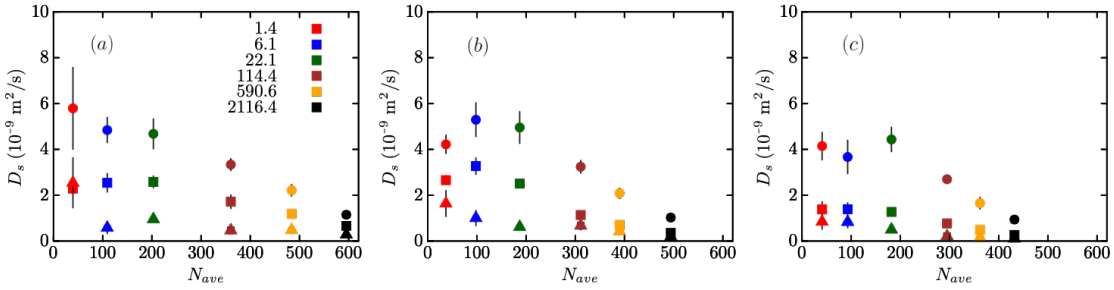

Figure 3.30 | Argon self-diffusion coefficients in the x (squares), y (triangles), and z (dots) directions, as function of the average number of fluid molecules varying through pressure changes (between 1.4 and 2116.4 bars) at a temperature of 243 K for the systems obtained from NPT/GCMC (a), NVT/GCMC (b) and GCMC (c).

Anisotropic transport seems occurring preferentially in z direction with similar transport coefficients in other two directions while not allowing the volume expansion during adsorption and in the totally frozen matrix. In contrast, the combination of adsorption-induced swelling and internal matrix flexibility seems to transform the model into a more inhomogeneous one.

Noticeably, in addition to the matrix flexibility, most of the physical processes, such as compression, fluid adsorption/desorption which induce important matrix restructuring are accompanied by non-affine deformations that may assist the emergence of anisotropy.

3.5 | Adsorption-Induced Swelling Effect on Fluid Transport

The diffusion in two kerogen atomistic models – immature and mature – is discussed here, with special attention on adsorption-induced swelling effects.

Type I Immature Kerogen

Following recent work on fluid transport accounting for matrix flexibility effects [7], the investigation of the methane and carbon dioxide self-diffusion coefficients within the flexible organic model has been performed for a large set of thermodynamic conditions. The prescribed mechanical pressures are 0.1, 25 and 100 MPa for different temperatures - 300, 400 and 500 K for methane and 300, 400 K for carbon dioxide. As mentioned in the numerical procedure section 2.6.1, we benefit from the efficient implementation of the AIREBO force field within the LAMMPS MD calculation package [100] in order to obtain accurate estimations of the self-diffusion coefficients. This can be seen in figure 3.31 which gathers the evolution of the diffusivity with the methane loading as well as the error bars (95% confidence intervals) estimated from 5 independent runs for the different confining pressures and temperatures investigated here. Such accuracy notably allows obtaining clear trends for the parameters of the free volume model detailed later.

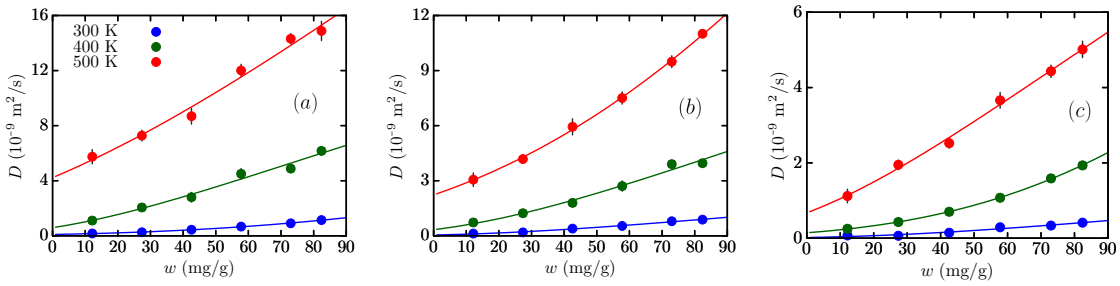

Figure 3.31 | Evolution of the self-diffusion coefficient with the methane loading for three different temperatures and pressures of (a) 0.1, (b) 25 and (c) 100 MPa. The solid curves correspond to the free volume model with the parameters $\alpha(T,P)$ and $\xi(T,P)$ estimated from a best fit procedure and collected in figure 4.3.

Contrary to the transport properties within a rigidified atomistic model of kerogen, or a kerogen model totally or partially (e.g. with so-called “virtual nails”) frozen, the more there are fluid molecules adsorbed in a flexible kerogen matrix, the greater the diffusion is. This enhancement of the transport with the fluid loading results from the matrix swelling under constant applied mechanical pressure and, consequently, the increase of the accessible free volume ratio as illustrated in figure 3.1. We note that this increase is more important for larger temperatures and for lower mechanical pressures (notice the different scales

on the three different graphs of figure 3.31). These results confirm previously obtained dependency between D_s and thermodynamic conditions for two models of type II kerogen – with adsorbed methane and carbon dioxide – from the set of three temperature (298, 340 and 380 K) and five pressure (1, 9, 15, 20 and 30 MPa) values [122].

The matrix with carbon dioxide as well exhibits the increase in transport properties with fluid adsorption (figure 3.32). Although, this increase is not as pronounced at high porosity where the effect of swelling is significant, probably because the interaction of fluid molecules with solid walls reaches its maximum. The confinement pressure in this case has a crucial impact on the transport: the last drastically decreases almost twofold after contraction upon a pressure change from 0.1 MPa to 25 MPa. From this moderate to higher applied mechanical pressure fluid motion tends to decelerate more slowly. The dependence of diffusion rate on temperature is most prominent for any thermodynamic condition which reaffirms its greater influence on transport.

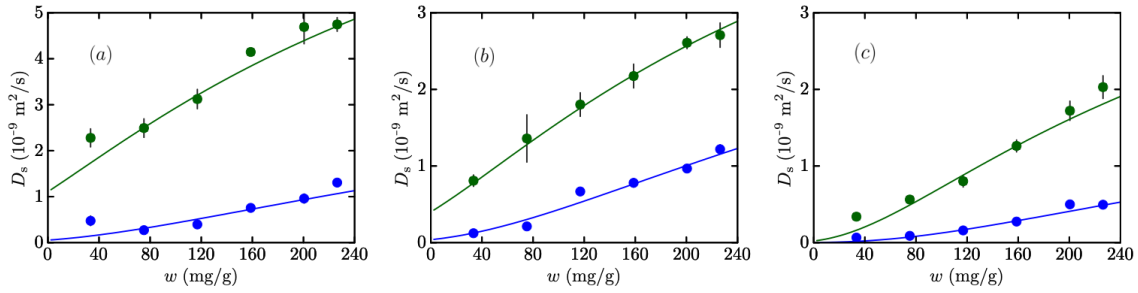

Figure 3.32 | Evolution of the self-diffusion coefficient with the carbon dioxide loading for pressures of (a) 0.1, (b) 25 and (c) 100 MPa. The solid curves correspond to the free volume model with the parameters $\alpha(T,P)$ and $\xi(T,P)$ estimated from a best fit procedure and collected in figure 4.10.

Comparing to the methane transport (figure 3.33), the diffusivity is similar for both fluids at low porosity which is ensured by a cold temperature (300 K). However, allowing relatively large volume expansion leads to the predominating diffusion of carbon dioxide despite the matrix shrinkage in the presence of the fluid. As mentioned recently, the slowdown of the carbon dioxide diffusion for the greatly swollen matrices apparently occurs as a consequence of raised solid-fluid interactions from the increase in surface area per unit volume which according to the scaling laws could notably decrease the matrix porosity. This phenomena is manifested most for carbon dioxide because of the stronger coupling between the solid and the fluid. Conversely, keeping the matrix volume for higher methane loading while performing molecule-to-molecule replacement leads to the acceleration of carbon dioxide by providing new paths for fluid molecules (black triangle in figure 3.33).

Based on previous works [5, 14], it can be assumed that the mixture of the studied fluids in immature kerogen will have little effect on the transport of each component. As it was revealed by Collell et al. [4] and Obliger et al. [14], the cross-correlations between the different species are negligible, so that if the available free volume is constant, methane

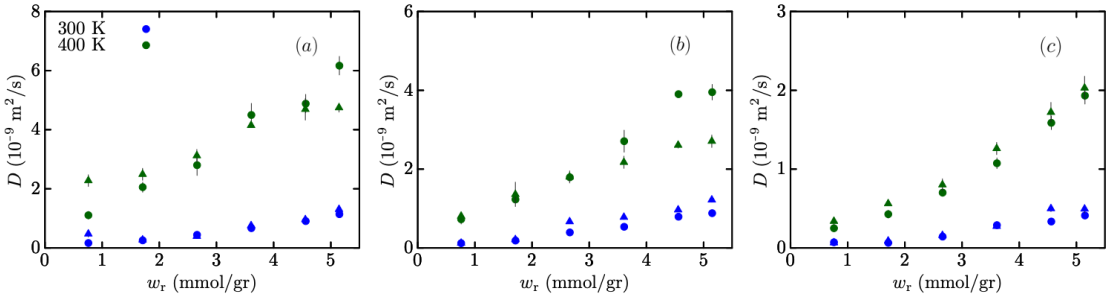

Figure 3.33 | Evolution of the self-diffusion coefficient with the methane (circles) and carbon dioxide (triangles) loading for pressures of (a) 0.1, (b) 25 and (c) 100 MPa.

and carbon dioxide molecules will diffuse at the same rate, regardless of the mixture's composition. At constant mechanical pressure, the resulting accessible free volume will vary with the molar fraction of the mixture in between the pure fluids results, decreasing diffusion for methane and increasing diffusion for carbon diffusion with respect to their pure fluid counterparts.

Type III Mature Kerogen

The small size of the mature kerogen matrix ($\sim 4.8 \times 3.9 \times 3.4\ \mathrm{nm}^3$) having an orthorhombic form implies anisotropic effects. Thus, the argon diffusivity is computed independently for each Cartesian direction (x, y, z) and shown in figure 3.34 for systems taken from all adsorption schemes (NPT/GCMC, NVT/GCMC and GCMC).

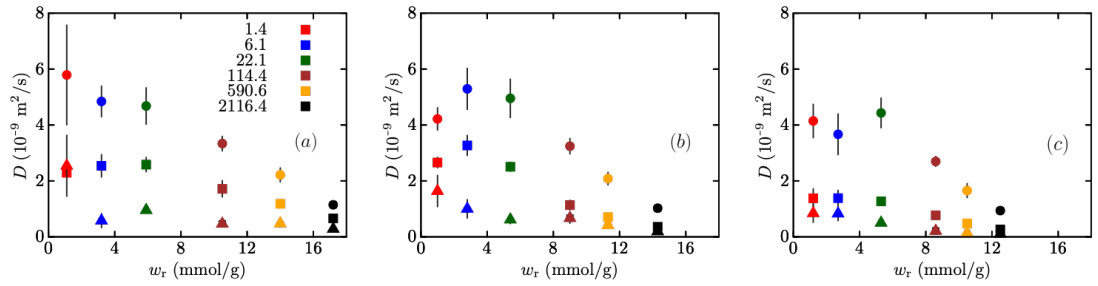

Figure 3.34 | Evolution of the argon self diffusivity along the x (dots), y (squares), and z (triangles) directions as functions of molar loading computed using the NPT (a), NVT (b) and RIGID (c) schemes. The hydrostatic pressure is indicated by the colour code in bar.

Based on the pore-volume characteristics of the swollen models at the cold temperature (243 K) (section 3.2.2), the transport tends to decrease with fluid adsorption despite significant swelling. Whilst the analysis of the accessible porosity is not able to explain this decrease, the free volume calculations show that the lack of the volume which may be occupied by fluid induces the slowdown of the argon molecules motion. The transport within three considered adsorption schemes is compared despite the non-negligible error

bars. As expected, neglecting adsorption-induced swelling and solid's flexibility within the rigid solid approximation leads to underestimated diffusivity values. In the most plausible between these three adsorption schemes - NPT/GCMC - the diffusion is more rapid than for the model with prevented volume change (NPT/GCMC).

3.6 | Conclusion

We have extended the previous studies of transport in microporous organic matter [5, 6, 14], which have been mostly performed within an approximation that kerogen is a completely rigid solid, by accounting for flexibility effects from equilibrium molecular dynamics simulations of two models representing kerogen in the middle of the oil formation window and at the end of the gas formation window, thereby covering the full diversity of kerogens valuable for gas and oil production. We have proven for the first time on the basis of very long dynamics (tens of nanoseconds) that transport in micropores of kerogen, which exhibits strong flexibility, is purely diffusive, and it is sufficient to use the self-diffusion coefficient to estimate transport properties, since kerogen flexibility does not contribute to fluid-fluid cross correlations.

The analysis of porous properties has shown that for both kerogen models significant adsorption-induced swelling is observed, which leads to an increase in the porosity even under ultra-confining thermodynamic conditions and even when mature kerogen is considered at a very low temperature. We demonstrate that this strain (swelling) increases to a lesser extent for carbon dioxide than for methane, since the former exhibits a stronger interaction with the solid walls. Moreover, we have observed a contraction of the kerogen matrix when methane is replaced by carbon dioxide, accompanied by important non-affine deformations. At low fluid loading, carbon dioxide has shown decreased porosity relative to the unloaded solid matrix in contrast to adsorbed methane. Despite the lack of time to study fluid mixtures in kerogen, from works on this topic [5, 14], we assume that the impact of one fluid on another in a mixture containing, for example, light hydrocarbons, water, carbon dioxide will be negligible, and, therefore, all our conclusions will be valid for mixtures as well.

Overall, the general increase in the porous properties of kerogen thanks to adsorption-induced swelling has led to an increase in transport in the immature model. This transport enhancement has been well explained by the accessible free volume increase, which prompted us to choose this property for fluid transport modeling, which will be presented in the next chapter. In addition, we raised the question of the size of representative atomistic models. We have determined that models of 6 nm and larger should be used to yield isotropic transport properties.

In summary, this chapter on transport in microporous kerogen is indeed closely related to the study of transport in similar structurally and/or mechanically micro- and nanoporous

media such as carbon materials, polymers, zeolites, etc., and thus has a contribution to wide industrial applications.

Chapter 4

Fluid Transport Modelling

Contents

4.1 | Introduction

The classical Darcy's transport description works well for macro- and some nano- porous media linearly coupling the fluid flux to the pressure gradient by mobilizing well-defined concepts, the fluid viscosity and solid permeability, which characterize independently the fluid and the solid phases, respectively. However, when permeability becomes ultra-low, as in kerogen, strong adsorption effects change the nature of fluid dynamics and thermodynamics, making the distinct phases' characterization obsolete. The conventional phenomenological law can thus no longer be applied. On the basis of molecular simulations, several attempts have been proposed to rationalise fluid transport in materials with extremely low porosity. A model of nanoscale hydrocarbon dynamics in a rigidified solid has been proposed through a linear dependence of fluid transport on the pressure gradient [6, 14]. In contrast with the Darcy's equation, the introduced permeance, replacing the permeability in this model relates to the adsorbed fluid and loading. Studying the velocity profile in micropores reaffirms a not simple dependence of fluid rate on solid-fluid couplings [123].

Earlier advances in fluid transport modeling have been obtained within the framework of the frozen solid approximation. Flexibility effects have only begun to be taken into account in modelling fluid transport in kerogen very recently [7, 124]. The free volume theory was found to be well suited to capture the increase in diffusion rate due to adsorption-induced swelling. Established initially for prediction of diffusion in swollen polymers by Fujita and Kishimoto [125–128], it uses the available volume for fluid molecules as potential space for fluid motion. A similar description has been done for diffusion in liquid and glassy states of matter [129, 130].

Inspired by the free volume approach and the fact that the transport increase is attributed to an increase in accessible space, we involved it in modelling the coupling between transport and the poromechanical properties of flexible kerogen. Thus, the chapter is structured in the following order:

- The first section gives a basic idea of the implementation of the Fujita-Kishimoto free volume theory to MD data.
- The second section introduces the transport model for methane involving the accessible free volume.
- In the third section the free volume model of the carbon dioxide transport is discussed.

4.2 | Free Volume Modelling Procedure

The transport enhancement with the fluid loading results from the matrix swelling under constant applied mechanical pressure and, consequently, the increase of the accessible free

volume ratio, φ_f which has been quantified in section 3.2. The large set of immature models swollen with different amount of fluid (methane and carbon dioxide) under a wide range of thermodynamic conditions has allowed to accurately model the fluid diffusion in kerogen. In this regard we proposed a two-step fitting technique. Primarily, the evolution of φ_f^a which is characterized as linear with the fluid loading w as follows,

$$\varphi_f^a(w) = \varphi_0^a + \beta w \tag{4.1}$$

is fitted to get the accessible porosity with no fluid adsorbed φ_0^a and a coefficient capturing the increase of free volume under adsorption-induced swelling β. The subsequent step implies the use of the Fujita-Kishimoto free volume equation describing the strong dependence of the diffusion coefficient on the accessible free volume increase,

$$D(w) = D_0 \exp\left[\alpha \frac{\varphi_f^a(w) - \varphi_0^a}{\varphi_0^a \varphi_f^a(w)}\right] \tag{4.2}$$

where the diffusion coefficient in the zero loading limit is introduced as $D_0 = \frac{k_B T}{\xi_0}$ with ξ_0 the friction coefficient and α the free volume coefficient that reflects on the ability of the fluid molecules to take advantage of the increasing accessible free volume to diffuse faster. Developing this equation (equation 4.2) with D_0 and the linear expression 4.1 for the accessible free volume ratio gives

$$D(w) = \frac{k_B T}{\xi_0} \exp\left[\alpha \frac{\beta w}{\varphi_0^a(\varphi_0^a + \beta w)}\right], \tag{4.3}$$

a model that is confronted here to the computed diffusion coefficients. Thus, the parameters α and ξ_0 are fitted against those diffusion coefficients with the parameters related to the free volume evolution, φ_0^a and β, imposed and taken from the first step.

The presented model captures the dependence of transport on solid-fluid couplings for a carbon matrix with different adsorbed fluids at a broad set of temperature and pressure values.

4.3 | Free Volume Model for Methane Transport in Immature Kerogen

A linear characterization of the free volume accessible to methane molecules with loading (figure 3.7) has enabled to capture the evolutions of the free volume parameters, φ_0^a and β, with the thermodynamic conditions which are summarized in figure 4.1.

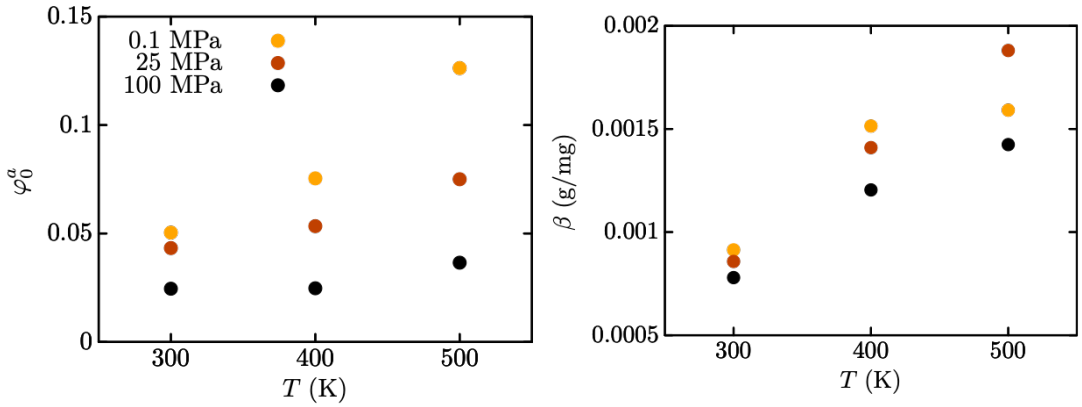

Figure 4.1 | Accessible free volume ratio of the empty matrix φ_0^a (left) and the linearity coefficient β (right) capturing the increase of the accessible free volume with methane loading under constant applied mechanical pressure shown in figure 3.7.

The negligible temperature variation of φ_0^a at the largest pressure investigated (100 MPa) along with the linear evolution of β with the temperature shows that thermal expansion at this pressure develops only when fluid is adsorbed in the matrix. Otherwise, decreasing the mechanical pressure allows for important thermal expansion even at zero loading. This expansion is more pronounced when the pressure is reduced by 75 MPa (from 100 MPa to 25 MPa) than by 25 MPa (from 25 MPa to 0.1 MPa) at regular reservoir pressure (∼300 K to ∼400 K) while at high temperature (500 K) it is reversed which may be explained by the fact that the matrix, from a certain low density, tends to expand more with lower pressure. In general, the matrix expansion is not linear as a function of temperature, which might be due to the structural features of the matrix affected by temperature effects. Finally, we notice that the coefficient β mostly depends on the temperature and not that much on the pressure.

Now that the accessible free volume increase is quantified by a linear model, we thus turn on the determination of the friction coefficient ξ and the free volume parameter α. To do so, equation 4.3 has been fitted against the self-diffusion coefficient data, the adjusted free volume model is plotted in figure 3.31 with the self-diffusion coefficients.

As can be clearly seen, the resulting model is in very good agreement with the data and can be used to capture the increasing trend of the transport properties with the fluid loading caused by the swelling. The obtained values for the free volume parameters, ξ_0 and α, are reported as a function of the temperature and pressure in figure 4.3.

The friction coefficient ξ_0 decreases with the temperature because of thermal expansion that leads to an increase of the accessible free volume that is also accompanied by a lowering of the local energy barriers in the limit of very low fluid loading. In such conditions, the adsorption-induced swelling is critical since the pore space is mostly closed and diffusion is heavily impacted by the local matrix fluctuations [7]. On the contrary, when the swelling is important, the connectivity of the pore space is better and pore size fluctuations become

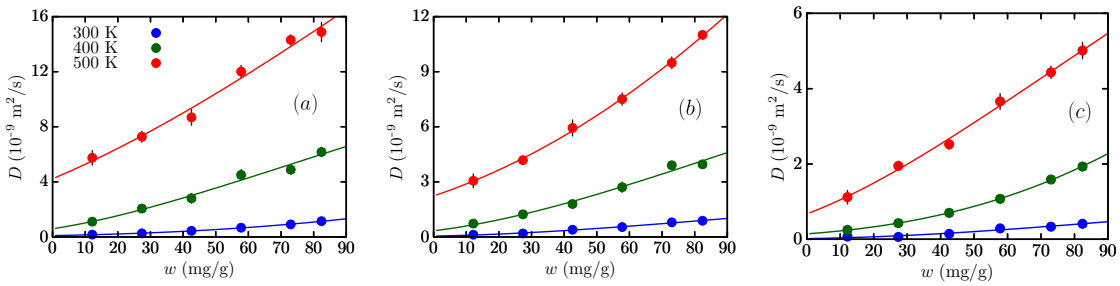

Figure 4.2 | Evolution of the self-diffusion coefficient with the methane loading for three different temperatures and pressures, (a) 0.1, (b) 25 and (c) 100 MPa. The solid curves correspond to the free volume model with the parameters $\alpha(T,P)$ and $\xi(T,P)$ estimated from a best fit procedure and collected in figure 4.3.

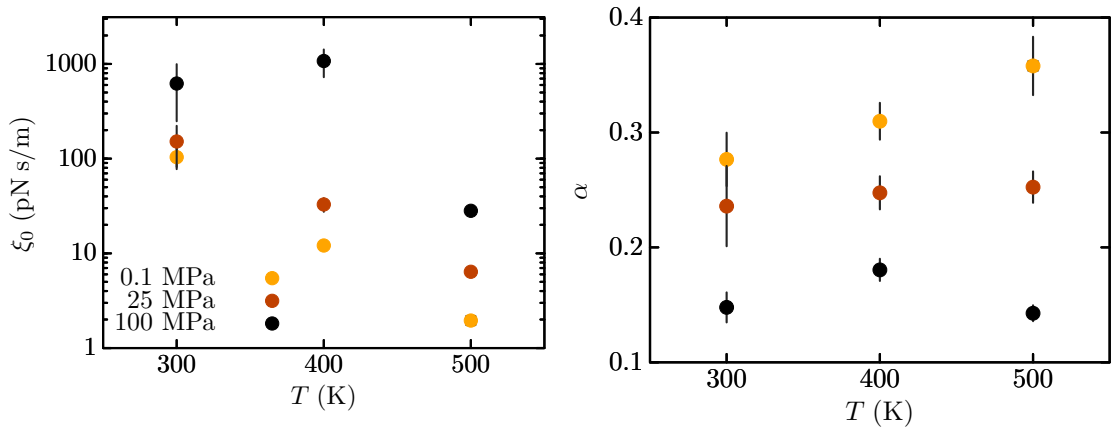

Figure 4.3 | Temperature evolution of the friction coefficient ξ_0 (left) and the free volume parameter α (right) obtained from a best fit procedure with the parameters φ_0^a and β corresponding to the different conditions taken from figure 4.1.

less influential. Globally, the friction coefficient increases with mechanical pressure, which correlates with the restriction of swelling with increasing pressure. We see at large pressure (100 MPa) that the friction does not evolve between 300 and 400 K because the accessible free volume ratio remains constant (figure 4.1). In turn, the free volume coefficient α (figure 4.3) is relatively unaffected by the thermal expansion. Though, at very low mechanical pressure, 0.1 MPa, the coefficient α is slightly increasing. Overall, this parameter is not that sensitive to the pressure, its value is going on average from around 0.15 to above 0.31 for a pressure spanning three orders of magnitude. To test the sensitivity of the model to α we performed the same modeling while implying the averaged values of α for each pressure and not changing ξ_0. Figure 4.4 shows that this approximation is valid only for the intermediate pressure of 25 MPa and for 400 K, 0.1 MPa while being quite sensitive to α for the highest pressure (100 MPa) and temperatures of 400 K and 500 K.

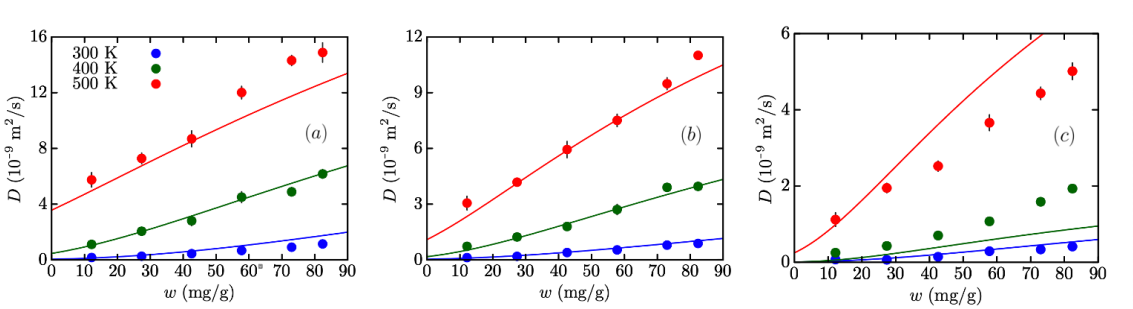

Figure 4.4 | Evolution of the self-diffusion coefficient with methane loading for three different temperatures at pressures, (a) 0.1, (b) 25 and (c) 100 MPa. The solid curves correspond to the free volume model with the parameters α(P) averaged over the three different temperatures and ξ_0(T,P) taken from figure 4.3.

4.4 | Free Volume Model for Carbon Dioxide Transport in Immature Kerogen

Only the temperature range close to the typical reservoir state (~300-400 K) is involved to model carbon dioxide diffusion affected by poroelastic coupling with the solid dynamics. To confirm the free volume model and fully compare it with its version for methane transport, an analysis similar to that described above is performed while considering two probes radii — 3.73 Å and 3.3 Å corresponding to the kinetic radii of methane and carbon dioxide, respectively.

The increase in the free volume accessible to carbon dioxide molecules (figure 3.14 has allowed to yield the evolution of φ_0^a and β shown in figure 4.5.

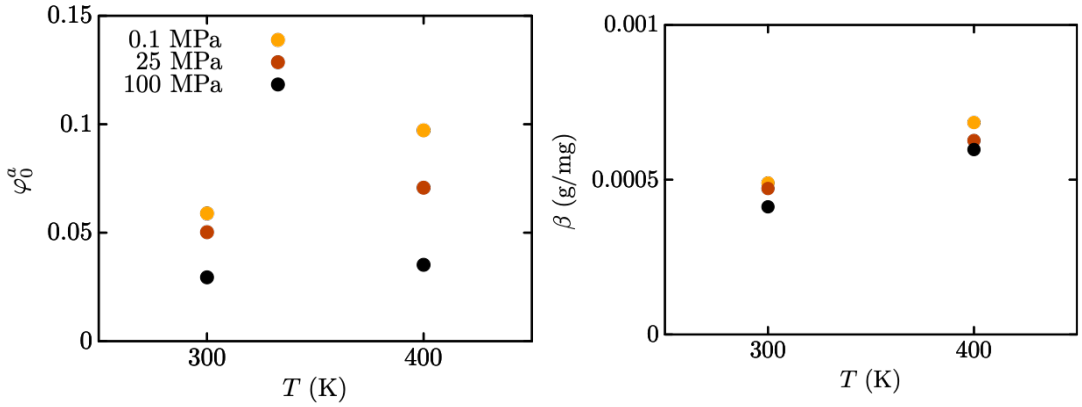

Figure 4.5 | Accessible porosity of the empty matrix φ_0^a (left) computed with carbon dioxide as a probe and the linearity coefficient β (right) capturing the increase of the accessible free volume with the carbon dioxide adsorption for a wide range of T-P conditions shown in figure 3.14.

The porosity of the empty matrix obtained using the carbon dioxide probe for the accessible free volume data is quite similar to that in the case of methane (figure 4.1) but slightly higher as expected because the size of the carbon dioxide sphere is smaller than that of methane. φ_0^a evolution follows the same increasing trend and reaffirms its small dependence on temperature at the highest confining pressure. However, the linearity coefficient β (figure 4.5) is much smaller indicating lower pore enlargement due to limited pore space (see shrinkage of the matrix with CO_2 replacement in figure 3.15). This parameter increases more with temperature, as has been shown for adsorbed methane (figure 4.1).

Here we follow the same steps to model the impact of swelling on diffusion with the free volume model used above for adsorbed methane. Collecting the obtained parameters, φ_0^a and β, has allowed to model a set of carbon dioxide transport coefficients by imposing the free volume parameter $\alpha(T,P)$ and friction coefficient $\xi(T,P)$, according to equation 4.3. Figure 4.6 illustrates the result of this modelling allowing for characterization of the transport increase due to carbon dioxide adsorption.

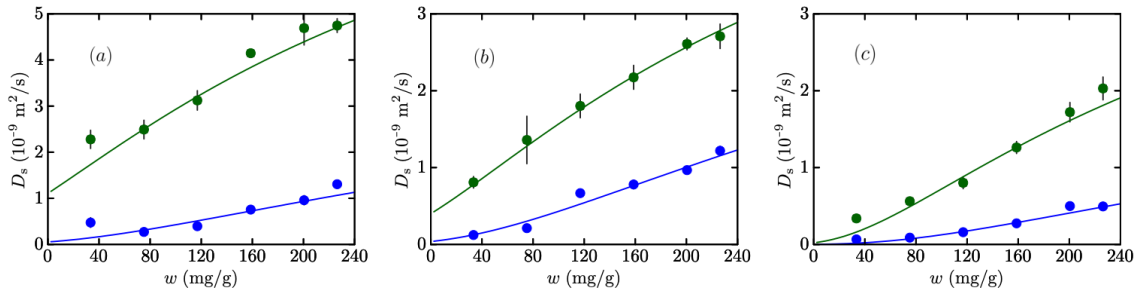

Figure 4.6 | Evolution of the self-diffusion coefficient with the carbon dioxide loading for 300 and 400 K and three different pressures: (a) 0.1, (b) 25 and (c) 100 MPa. The solid curves correspond to the free volume model based on the obtained parameters (figure 4.5) and the parameters $\alpha(T,P)$ and $\xi(T,P)$ estimated from a best fit procedure and collected in figure 4.7. For an ultra-confining pressure of 100 MPa, one of the five curves has been eliminated in an arithmetic averaging procedure to obtain the proper average fitting curve.

As seen for all confining pressures, the diffusion enhancement for adsorption-induced swelling is in good agreement with the model, despite that carbon dioxide is a more interacting with solid and dissymetric molecule than methane. The free volume model works well even when the transport trends are less regular for adsorbed CO_2 than for CH_4. It also seems to capture changes in curvature for CO_2, especially at a temperature of 400 K and a pressure of 0.1 MPa. Such curvature changes were not present for CH_4. For a temperature of 300 K and pressure of 0.1 MPa, the evolution of the diffusivity with carbon dioxide loading is not monotonic, which is not well captured by the free-volume model probably because the approximation of the accessible free volume ratio evolution as linear is no longer accurate in this case. Whereas at ultra-confining pressure, which induces an increase in the strong solid-fluid couplings and adsorption effects, the free volume model still captures the transport increase. It should be noted that, under these conditions, the model curve has

been obtained by arithmetically averaging the free volume parameters while excluding one of the five independent parameter determinations because of the nonlinearity of the model. However, this exclusion does not extend to the estimates of the parameter values shown in figure 4.7.

The temperature evolution of the corresponding friction coefficient in the zero loading limit ξ_0 and the free volume parameter α obtained by applying the free volume model to the carbon dioxide transport evolution are presented in figure 4.7 for the three different pressures investigated.

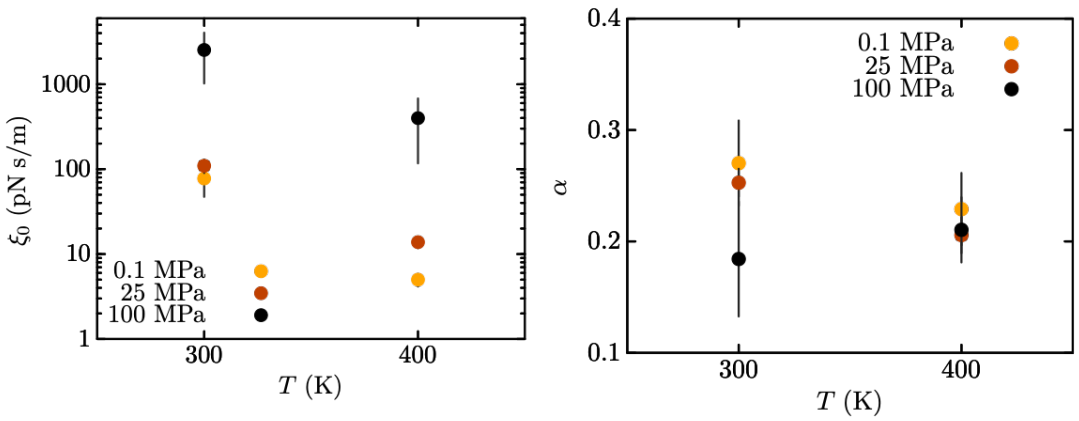

Figure 4.7 | Friction coefficient ξ_0 (left) and the free volume parameter α (right) obtained from a fit procedure with the parameters φ_0^a and β corresponding to the different conditions taken from figure 4.5.

$\xi(T,P)$ confirms the previously established temperature and pressure dependence obtained for adsorbed methane. However, it seems quite sensitive to the value of the free volume parameter α. Since this parameter seems lower than for methane, as the accessible free volume expansion is limited in the carbon dioxide case, and because of the curvature changes for some thermodynamic conditions, the friction coefficient in the zero loading limit tends to decrease in comparison to methane. The exception is the ultra-low porosity matrix (at 300 K, 100 MPa) where stronger solid-fluid interactions for carbon dioxide are reflected. As illustrated in the left graph of figure 4.7, the temperature evolution of α appears to be limited despite large error bars for the three different pressures, as it was reported for methane. In contrast to methane, however, mechanical pressure does not have a strong influence, if the ultra-confinement condition at 300 K and 100 MPa is discarded. Since this condition is not realistic geologically speaking, we conclude that for geological conditions, the mechanical pressure does not influence the parameter α in the case of adsorbed CO_2.

The next step was to verify the free volume model robustness to the probe radius by using the methane probe. The porosity of the empty kerogen matrix available to methane molecules which were obtained from the linear model shown in equation 4.1 using the data

on the porous properties for the carbon dioxide loaded kerogen systems (figure 3.21) is given in figure 4.8.

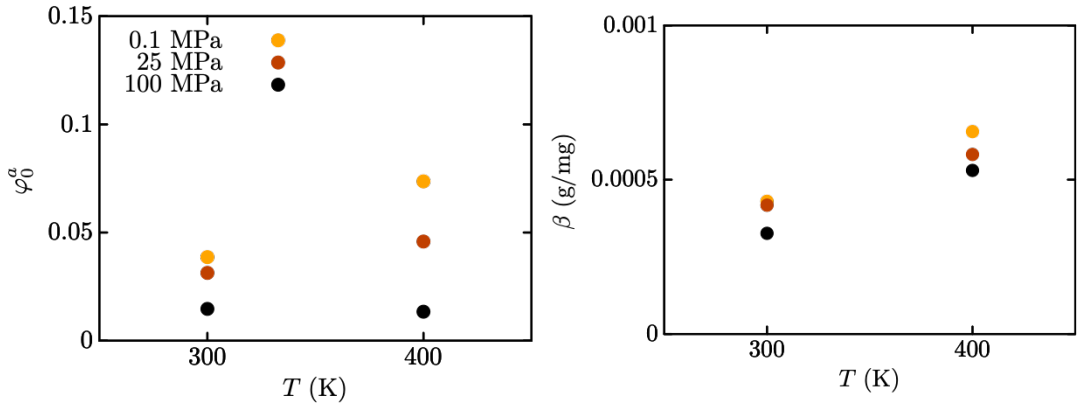

Figure 4.8 | Accessible porosity of the empty matrix φ_0^a (left) computed with methane as a probe and the linearity coefficient β (right) capturing the increase of the accessible free volume with the carbon dioxide adsorption for a wide range of T-P conditions shown in figure 3.14.

Accessible porosity of the empty matrix φ_0^a and the linearity coefficient β follow the same trends with temperature and pressure evolution as for adsorbed methane (figure 4.1). Nevertheless, they are smaller because accessible volume was not adapted to such larger molecules. β also shows the lack of the free volume comparing to previous results for this parameter obtained with a carbon dioxide probe.

Fitting the diffusion data to the free volume equation yields almost identical characteristic curves for both probes (figure 4.9). Compared to the previous fitting procedure, the model curve for the ultra-confining conditions has been obtained by logarithmically averaging the free volume parameters while excluding one of the five independent parameter determinations due to the nonlinearity of the model used. Recall that this exclusion does not apply to the estimates of the parameter values shown in figure 4.10. Thus, it is validated that this model is applicable to the case of a fluid characterized by strong solid-fluid interactions such as carbon dioxide at all thermodynamic conditions.

Two parameters, the friction coefficient at the zero loading limit ξ_0 and the free volume parameter α have been obtained by applying the free volume model (figure 4.10).

Although the trends of the free volume parameters evolution are similar between the two probes, the values of α are lower, in spite of the large error bars, because the accessible free volume decreases for larger molecules. It can be seen that this is arguably independent of temperature and poorly dependent on pressure. The evolution of the parameter ξ due to its sensitivity to α leads also to its diminution compared to methane. It should be noted that the proposed method for computing the accessible free volume may underestimate the results owing to the probe geometry, especially for carbon dioxide, which may affect the application of the free volume model as well.

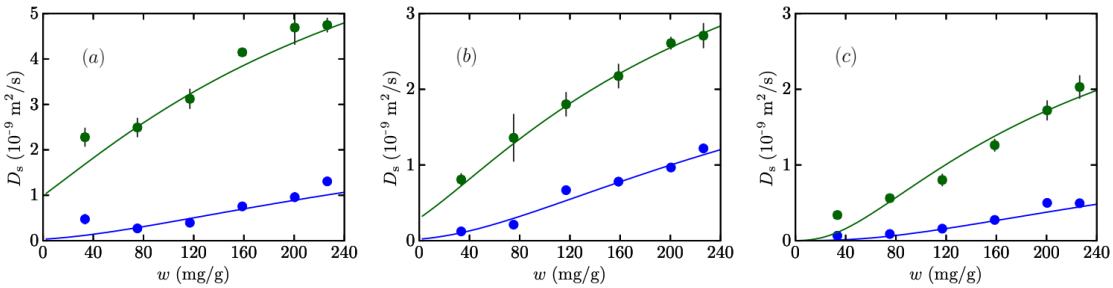

Figure 4.9 | Evolution of the self-diffusion coefficient with the carbon dioxide loading for 300 and 400 K and three different pressures: (a) 0.1, (b) 25 and (c) 100 MPa. The solid curves correspond to the free volume model based on the obtained parameters (figure 4.8) and the parameters $\alpha(T,P)$ and $\xi(T,P)$ estimated from a best fit procedure and collected in figure 4.10. For an ultra-confining pressure of 100 MPa, one of the five curves has been eliminated in a logarithmic averaging procedure to obtain the proper average fitting curve.

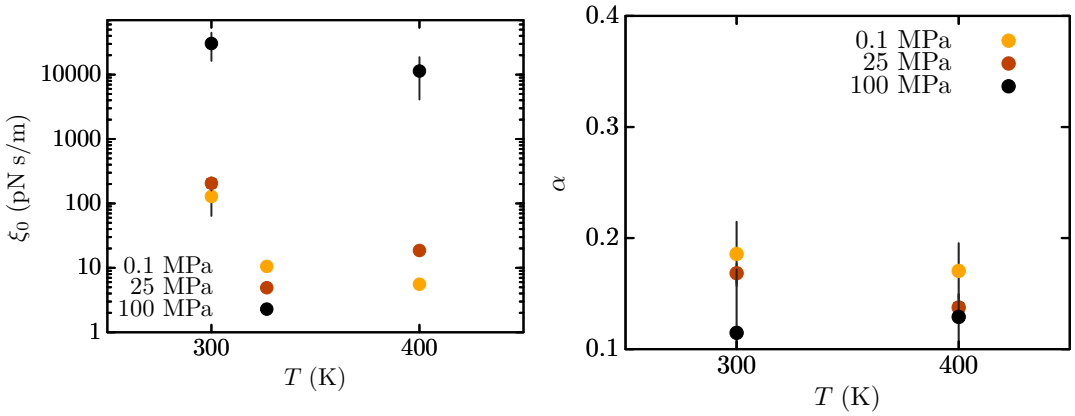

Figure 4.10 | Friction coefficient ξ_0 (left) and the free volume parameter α (right) obtained from a best fit procedure with the parameters φ_0^a and β corresponding to the different conditions taken from figure 4.8.

4.5 | Conclusion

In this chapter, the free volume theory has been proposed to model transport properties in microporous kerogen, which exhibits flexibility effects, through a description of the diffusion increase with adsorption-induced swelling based on the accessible free volume expansion. A complete analysis of the free volume model and its parameters has been performed, involving improved statistics and extending for a large range of thermodynamic conditions. Its robustness has also been verified on two different fluids, methane and carbon dioxide.

I have shown that it perfectly models the diffusivity evolution with fluid loading for the case of adsorbed methane for a broad set of thermodynamic conditions, including those

close to the typical geological ones. In this context, it was important to take into account the evolution of a large set of temperatures and pressures to fully characterize the transport dynamics, since in geological conditions they both increase with burial depth. Application of the model to kerogen with a more energetically dense fluid, carbon dioxide, has resulted in a well- captured increase in diffusion with CO_2 loading and shown similar dependence of the free volume parameters on temperature and pressure, thus proving that this model is robust in describing the transport of a confined fluid affected by adsorption effects. Furthermore, it captures well the nonmonotonic tendency of increasing fluid transport for the case of carbon dioxide for geological conditions. Even at ultra-high confining pressure of 100 MPa, when the adsorption effects are strong and the solid-fluid interaction is quite pronounced, the free volume model has proven to be accurate when considering a more energetically dense fluid such as carbon dioxide.

The results obtained on transport modeling based on the free volume theory can be directly applied to molecular modeling of multicomponent diffusion. Regarding some recent propositions to rationalize the fluid transport in kerogen, such as those of Collell and colleagues [5, 68] on a correction factor and those of Obliger and colleagues [14] on the application of the accessible free volume to model transport, they have neglected the flexibility effects of the solid, considering it as a rigidified matrix. Based on the previously introduced single-component diffusion model, we suggest that ethane, propane and even butane, for which isosteric heats of adsorption are between those of methane and carbon dioxide, will behave intermediately and thus can be modeled by the proposed free volume model. However, many additional questions arise, such as whether the pressure dependence of the free volume parameter α would be even more negligible for hydrocarbons heavier than butane or whether the free volume model would work for heavier than carbon dioxide fluids if some correction factor were imposed to account for the deviation from theory. All of these challenges must be proven, therefore we address these questions to a future research.

In conclusion, accounting for the dependence of solid-fluid couplings on temperature, pressure and fluid loading through the strong link between the accessible free volume and transport, the free volume model has the potential to be an advanced step for building a general theory of transport in microscale porous solids.

CHAPTER 5

Molecular Fluid Dynamics from Memory Kernels

Contents

5.1 | Introduction

Microscale fluid diffusion is generally impacted by non-Markovian effects since memory of past dynamics is preserved and affects further evolution of the system where solid-fluid and/or fluid-fluid interactions are significant [131,132]. Such memory effects are intimately related to the nature of the friction at the microscopic scale that becomes time dependent. In the insightful framework of the generalized Langevin equation, the so-called memory kernel, which is the key quantity capturing this complex time dependence, is often neglected because of the difficulty of its proper evaluation from the thermal fluctuations of the microscopic details. Albeit it can provide valuable information on the impact of solid-fluid couplings on the molecular fluid dynamics which was shown to be crucial in the previous chapters 3 and 4 on fluid transport in kerogen. Whereas these studies on the adsorption and flexibility effects that induce transport increase have been carried out to extract late-time quantities from molecular trajectories, i.e. the diffusion coefficients that characterise the Fickian regime where the mean square displacements scale linearly in time, valuable information on molecular fluid dynamics could also be obtained at short and intermediary timescales. As a first step toward this goal, I employed recent and promising coarse-graining approaches (by decreasing the model's degrees of freedom) based on iterative reconstructions of the memory kernel which incorporates the feedback of the environment, such as the kerogen matrix, on the fluid dynamics. I tested two algorithms: one based on the inversion of the Volterra equation of the second kind [133] and the other one based on the reconstruction of the forward orthogonal dynamics [9].

In this regard, the aim of this chapter is to extend the understanding of the fluid dynamics mechanism in kerogen involving the correlation functions and memory kernel analysis from molecular simulations.

Previously, the study of such memory effects has been done mainly for fluid dynamics based on hydrodynamics [134–137]. Recently, this approach has been applied to a monoatomic fluid using molecular simulation trajectories [9] where hydrodynamic governed modes have been successfully identified from long-term decays of correlation functions. In the present chapter we first reproduce the results of Lesnicki et al. [9] in order to test the implementations of the two iterative techniques used in the present work and expand this study to confined fluids in order to directly estimate the influence of the viscoelastic nature of the kerogen structure on the fluid dynamics at the short and intermediary time scales.

Furthermore, I characterized the impact of flexibility and loading effects on diffusion at long times through memory kernel and correlation functions which are simply obtained by averaging over time the fluctuating parameters of interest at two distinct times. Of particular importance for the computation of these correlation functions and memory kernel is their direct relation with the diffusion coefficient, which will also be shown in the following sections of the present chapter.

Thus, this chapter is organised as follows:

- The first section provides a presentation of the generalized Langevin Equation framework for fluid diffusion.
- In the second section I describe the molecular simulation setups for which memory kernels are computed.
- The third section introduces the two computational algorithms used for the reconstruction of the memory kernel.
- In the fourth section, molecular simulations of a bulk fluid are carried out to test our implementations of the two algorithms used to extract the memory kernel.
- The fifth section is devoted to an investigation of small and intermediate time couplings between the dynamics of the solid and fluid within a kerogen model. This section also addresses the evaluation of diffusion coefficients based on the ACFs.

5.2 | Generalized Langevin Equation Framework

The original Langevin equation has been introduced to understand the erratic motion of macroscopic objects, say colloids, in suspension, such as the pollen grains observed by Brown in water. In the framework of the Langevin equation, the forces acting on a colloid are splitted in two parts, (i) a dissipative part reflecting on the hydrodynamics resistance of the surrounding water molecules opposing the motion of the colloid, and (ii) a fluctuating part reflecting on the total average of the instantaneous microscopic collisions between the environment molecules and the colloids that is supposed to be random and decorrelated. One of the most important hypotheses made is the separation of time scales, that is, the time needed for the microscopic degrees of freedom to equilibrate is negligible compared to the time scales of the observed colloid's motion. This is otherwise known as the Markovian approximation. In the end, the Langevin equation is a stochastic differential equation based on the Newton equation of motion for the coarse-grained velocity v of the observed particle of mass m as

$$m\frac{\mathrm{d}v}{\mathrm{d}t} = -\xi v(t) + \eta(t)\,, \tag{5.1}$$

where ξ is a friction coefficient related to the dissipative force simply opposed to the particle velocity, and $\eta(t)$ is a white noise modeling the random microscopic degrees of freedom acting on the particle. This force is said to be stochastic, it is a random quantity that is not evolving continuously in time, and its statistics is imposed by its two first moments, (i) on average this force is not supposed to bias the particle motion in a particular direction,

leading to

$$\langle \eta(t) \rangle = 0\,, \tag{5.2}$$

and (ii) its variance (or magnitude) is given via the fluctuation-dissipation theorem as

$$\langle \eta^2(t) \rangle = 2k_B T \xi\,. \tag{5.3}$$

Because only the two first moments of the distributions are constrained, the white noise is said to be a Gaussian white noise even though a uniform distribution symmetric around zero can be considered. Also, the noise is not correlated to the velocity, we thus have

$$\langle \eta(t)\, v(0) \rangle = 0\,, \tag{5.4}$$

and is not correlated with itself, that is

$$\langle \eta(t)\, \eta(0) \rangle = 0 \tag{5.5}$$

for $t > 0$, where we simply take $t = 0$ as the starting point. Another consequence of the fluctuation-dissipation theorem is that the diffusion coefficient in the long time limit is directly given by the friction coefficient ξ through the Einstein-Smoluchowski relation:

$$D = \frac{k_B T}{\xi}. \tag{5.6}$$

It is to be noted that, in the case of large spherical colloids of radius R suspended in a solvent of viscosity μ, the friction coefficient reads as $\xi = c\pi\mu R$, where $c = 6$ or 4 for the "stick" or "slip" boundary conditions, respectively [138]. In fact, this relation appears to be very robust as it remains approximately valid even for tracer molecules that are not much bigger than the solvent molecules [138].

However, when the separation of time scales is not valid because the characteristic time of equilibration of the microscopic degrees of freedom is of the same order of magnitude as the typical observation time, the friction may become dependent on the time and the noise correlated in time (not proportional to the delta-function as implied by equation 5.5). In other words, memory or non-Markovian effects may arise. In such cases Mori H. and Zwanzig R. proposed a new formalism which can capture these delay effects through the introduction of projection operators [139–141]. Such formalism allows to construct the Generalized Langevin Equation (GLE) from the microscopic degrees of freedom via a rigorous coarse-graining procedure that integrates out irrelevant microscopic details. In summary, the projection operator technique introduces the so-called memory kernel $K(t)$, that can be seen as a generalized time dependent friction coefficient, to obtain a more

insightful version of the Langevin equation 5.1, that incorporates the memory effects:

$$m\frac{\mathrm{d}v(t)}{\mathrm{d}t} = -\int_0^t K(t-u)v(u)\mathrm{d}u + \eta(t)\,. \tag{5.7}$$

Specifically, the friction term now convolutes in time the velocity and the "time-dependent friction coefficient" to account for the time correlations of the past on the instantaneous configuration. As for the original Langevin equation, the fluctuation-dissipation theorem can be used to derive the following relation between the memory kernel $K(t)$ and the time correlation of the noise $\eta(t)$ [133]:

$$K(t) = \frac{1}{k_B T}\langle \eta(t)\eta(0)\rangle\,. \tag{5.8}$$

This expression replaces equations 5.3 and 5.5 that can be obtained again by introducing a delta-correlated noise ($K(t) = \xi\delta(t)$). In the GLE framework, the separation of time scales occurs when the time needed for the memory kernel to vanish is negligible compared to the observation time scale. As we are now interested in the intermediary time scale, i.e. before the fluid diffusion becomes Fickian and where only the friction coefficient ξ is required to quantify the confined fluid dynamics, the Markovian assumption does not hold anymore and the memory kernel will become the central quantity of interest. I will rely on recently developed methods based on stable algorithms, that are detailed below, to extract from equilibrium MD simulations the memory kernels of fluid confined in the immature type I kerogen structure. This comes at the price of investigating long MD trajectories to obtain significant statistics.

5.3 | Molecular Simulation Setup

As a first step, a bulk Lennard-Jones fluid is simulated to reproduce the memory kernel evaluation reported in [9] to test the validity of the hydrodynamic scaling on the long time decays of the memory kernel for a tagged molecule that is part of the solvent itself. In this case, unlike the usual case of a macroscopic colloid diffusing in a solvent, there is no separation of scales between the tagged particle and the solvent molecules. We thus more generally speak about molecular hydrodynamics. To reproduce the hydrodynamic scaling of the auto-correlation functions obtained for the bulk fluid, I followed exactly the same steps as in [9], (i) the first step consists in creating a cubic box with randomly inserted fluid atoms, (ii) relaxation of the model in the NVT ensemble is done to minimize its free energy, and (iii) production run is performed in the NVE ensemble to eliminate any spurious coupling between the thermostat and the time correlations.

Per-molecule information (velocity and force) is gathered for only one direction out of three to limit the memory usage. Block averaging is performed when calculating proper-

ties, dividing the total trajectory into 10 parts. Lennard-Jones (LJ) reduced units are used throughout this study to describe simulation details. In this regard, for consistency with further memory kernel analyses, the LJ parameters taken from [142] for argon and from [2] for methane is listed in table 5.1 below. The LJ time t^* is 1.35 ps for CH_4 and 2.17 ps for Ar. More detailed characteristics of the MD simulation stages in LJ units for these models are collected in table 5.2 where τ^*_{eq} is the time step and κ^*_{eq} is the time constant for the thermostat at the equilibration stage.

Ar		CH_4	
$\epsilon/k_B(K)$	σ (Å)	$\epsilon/k_B(K)$	σ (Å)
119.8	3.4	147.9	3.7

Table 5.1 | LJ parameters for argon and methane, respectively.

Parameters	Models	
	bulk fluid №1 [142]	bulk fluid №2
N of fluid molecules	10 000	10 000
L^*_{box}	27	27
ρ^*	0.5	0.5
T^*	1.5	1.5
t^*_{eq}	230.4	230.9
τ^*_{eq}	$9.2 \cdot 10^{-4}$	$9.2 \cdot 10^{-4}$
κ^*_{eq}	0.9	0.9
t^*_{run}	230.4	230.9
τ^*_{run}	$4.6 \cdot 10^{-4}$	$4.6 \cdot 10^{-4}$

Table 5.2 | MD simulation parameters for the bulk LJ fluid.

The second part of this study was performed for methane confined in the type I immature kerogen model at 400 K, 25 MPa to investigate the impact of adsorption and flexibility on fluid dynamics in terms of correlation and memory effects. Only the highest fluid content (82.4 mg/g) is considered within the rigid solid approximation, since the majority ($\sim$ 80 %) of molecules diffuse, while for the lowest fluid loading they mostly remain trapped over very long times. Very long simulations were performed to accumulate enough statistics for correctly reflecting the long time decays of the correlation functions. For this purpose, trajectories of 100 ns long with a 10 fs resolution have been generated, and divided into 5 blocks of 20 ns long for post-processing analysis. Five different solid configurations separated by at least 2 ns from the all-atom run have been stored to perform the rigid runs. The lowest loading (12.1 mg/g) has also been considered to investigate the swelling effect on the memory kernel while accounting for the flexibility of the matrix.

5.4 | Memory Kernel Calculation Algorithms

5.4.1 | Inversion of the Volterra equation of the second kind

Various methods have been reported in the literature to compute memory kernel [9, 133, 141, 143, 144] among which the inverse Volterra equation of second kind has shown the highest efficiency [143, 145]. Developed for a one dimensional and one particle system, it was recently revised for many-particle systems while remaining computationally efficient [145]. Here I present this simple derivation from the GLE. The GLE (equation 5.7) is simplified by excluding the noise due to its orthogonality with the velocity and multiplying the equation with the initial velocity $v(0)$ and taking the thermal equilibrium average ($\langle\cdot\rangle$), which gives the Volterra equation of the first kind

$$m\frac{\mathrm{d}\langle v(t)v(0)\rangle}{\mathrm{d}t} = -\int_0^t K(t-u)\langle v(u)v(0)\rangle\,\mathrm{d}u\,. \tag{5.9}$$

Numerically inverting it into the second kind form gives a more stable algorithm. Taking the time derivative of this equation then leads to

$$m\frac{\mathrm{d}^2\langle v(t)v(0)\rangle}{\mathrm{d}t^2} = -\langle v(0)^2\rangle\,K(t) - \int_0^t K(u)\frac{\mathrm{d}\langle v(t-u)v(0)\rangle}{\mathrm{d}t}\mathrm{d}u \tag{5.10}$$

that can be further simplifed by noting the relations between the velocity auto-correlation time derivatives and the force auto-correlation function

$$\frac{\mathrm{d}^2\langle v(t)v(0)\rangle}{\mathrm{d}t^2} = -\frac{1}{m^2}\langle f(t)f(0)\rangle \tag{5.11}$$

as well as the velocity-force cross-correlation function

$$\frac{\mathrm{d}\langle v(t)v(0)\rangle}{\mathrm{d}t} = \frac{1}{m}\langle f(t)v(0)\rangle\,, \tag{5.12}$$

where f is the total force acting on the particle, leading to

$$\frac{1}{m}\langle f(t)f(0)\rangle\ = \langle v(0)^2\rangle\,K(t) + \frac{1}{m}\int_0^t K(u)\langle f(t-u)v(0)\rangle\,\mathrm{d}u \tag{5.13}$$

which is the Volterra equation of the second kind. In passing, because the system is at thermal equilibrium, we have $\langle v(0)^2\rangle = \langle v(t)^2\rangle = v_{\mathrm{th}}^2$ with $v_{\mathrm{th}} = \sqrt{k_B T/m}$ the thermal velocity. To ease the readability in what follows, we now introduce the notation

$$C^{ab}(t) = \langle a(t)b(0)\rangle \tag{5.14}$$

for the time auto- and cross-correlation functions involving the dynamical quantities a or $b = v, f, \eta$, so that we can recast the previous equation as

$$C^{ff}(t) = mC^{vv}(0)\,K(t) + \int_0^t K(u)\,C^{fv}(t-u)\,\mathrm{d}u\,. \tag{5.15}$$

This equation can be discretized in time in order to invert it numerically and to obtain the memory kernel. The time series of the quantities obtained for the molecular dynamics trajectories with a time resolution δt are represented such as $f(i\delta t) = f_i$ for the total force, for instance, with the index i running over all the N_t available timeframes ($i \in [\![0, N_t - 1]\!]$), which leads to the discretization of the time correlation functions (equation 5.14) as

$$C_i^{ab} = \langle a_i b_0 \rangle \quad \text{for} \quad t = i\delta t\,. \tag{5.16}$$

The integral term of equation 5.15 is discretized using the simple rectangle rule as

$$\int_0^t K(u)\,C^{fv}(t-u)\,\mathrm{d}u = \sum_{j=0}^{i} \psi_j K_j\,C_{i-j}^{fv}\,\delta t\,, \tag{5.17}$$

where $\psi_j = 1 - \delta_{0j}$ are constants, with the last term of the sum that is separated to invert the time discretized version of the Volterra equation of the second kind (equation 5.15) as

$$K_i = \frac{C_i^{ff} - \delta t \sum_{j=0}^{i-1} \psi_j K_j\,C_{i-j}^{fv}}{mC_0^{vv} + \psi_i \delta t C_0^{fv}} \tag{5.18}$$

with the initial condition

$$K_0 = \frac{C_0^{ff}}{mC_0^{vv}} \tag{5.19}$$

established from equation 5.15. This integration scheme allows to iteratively reconstruct the memory kernel, that is essentially the noise auto-correlation function, from the total force auto-correlation function and the velocity-force cross correlation function. Both these functions can simply and reliably be obtained from molecular dynamics trajectories. Then, for a single fluid system, only one time series is numerically evaluated from the correlation functions that are already averaged over the fluid molecules of the system.

From a physical side, the memory kernel corresponds to the force auto-correlations removed from the contributions coming from the correlations between the force and the velocity. In the end, the noise is a stochastic force that is, by construction, decorrelated from the velocity. The second algorithm reproduced below follows a more involved path as its strategy consists in first reconstructing the noise for the trajectory of each molecule and

then computing its time auto-correlation function before averaging over the molecules. The advantage is that it also gives access to the "orthogonal" dynamics, in the wording of the projection operator formalism, as the noise is decorrelated from the velocity.

5.4.2 | Reconstruction of the Forward Orthogonal Dynamics

The second method is based on the reconstruction of the forward orthogonal dynamics [9] from the knowledge of the MD trajectory. While the previous method directly deals with the correlation functions, the present one works on reconstructing the noise $\eta(t)$ for each molecule trajectory, and then computing their time auto-correlation function to finish in practice by averaging them over the molecules. The memory kernel is then readily available from equation 5.8 ($K(t) = \beta\langle\eta(0)\eta(t)\rangle$). Noting that this relation can be expressed using the total force f, injecting the GLE (equation 5.7) in the just recalled relation leads us to

$$K(t) = \beta\langle f(0)\eta(t)\rangle \tag{5.20}$$

because the noise is orthogonal to the velocity at all time. Starting back from the Mori-Zwanzig (MZ) projection operator formalism, that can be used to derive the GLE, the memory kernel can be formally expressed only with the force. Introducing $\mathcal{P}$, the Mori projection operator along the velocity v through its action on a variable a

$$\mathcal{P}a = \frac{\langle a(0)v(0)\rangle}{\langle v^2\rangle}v(0) \tag{5.21}$$

where all the variables have been evaluated at the same time since the projector does not depend on time – $\langle v^2\rangle = v_T^2$ because the system is in thermal equilibrium –, the noise can be expressed as

$$\eta(t) = \mathrm{e}^{i(I-\mathcal{P})\mathcal{L}t}(I-\mathcal{P})f(0) \tag{5.22}$$

where I and $\mathcal{L}$ are the identity and the Lagrangian operators, respectively, or, by introducing the orthogonal projection operator $\mathcal{Q} = I - \mathcal{P}$, we obtain in a more compact manner

$$\eta(t) = \mathrm{e}^{i\mathcal{Q}\mathcal{L}t}\,\mathcal{Q}f(0)\,. \tag{5.23}$$

This definition of the noise ensures its orthogonality with the velocity, i.e. $\langle\eta(t)v(0)\rangle = 0$. This expression directly comes from the derivation of the GLE using the MZ projection operator formalism. Without entering in too much details, for an Hamiltonian dynamics, the time evolution of a variable is given through the Lagrangian operator as $a(t) = \mathrm{e}^{i\mathcal{L}t}\,a(0)$, which formally expresses what is happening in a MD simulation in the NVE ensemble, and in the NVT ensemble under certain conditions. Comparatively, the operator $\mathrm{e}^{i\mathcal{Q}\mathcal{L}t}$ entering the definition of the noise gives rise to the orthogonal dynamics of a variable. The time

evolution of the noise can be interpreted as the orthogonal dynamics of $\mathcal{Q}f(0)$ the orthogonal projection of the force $f(0)$. The memory kernel can be expressed as

$$K(t) = \beta\langle f(0)\, \mathrm{e}^{i\mathcal{Q}\mathcal{L}t}\, \mathcal{Q}f(0)\rangle\,. \tag{5.24}$$

In order to branch with the notations of the generic derivation of the original paper of Carof et al. [144], and more specifically those of section B which *differ* from section A, we note $\mathbf{A}(0) = f(0)$ and $\mathbf{B}(0) = \mathcal{Q}f(0)$ so that $K(t) = \beta\bar{C}_{AB}(t)$. On our side, to ease the notation, we introduce $g(0) = \mathcal{Q}f(0)$. The former expression for the memory kernel can be recast as

$$K(t) = \beta\langle f(0)\, \mathrm{e}^{i\mathcal{Q}\mathcal{L}t}\, g(0)\rangle \tag{5.25}$$

and, as in [144], we highlight that the memory kernel can also be expressed as

$$K(t) = \beta\langle g(0)\, \mathrm{e}^{-i\mathcal{L}\mathcal{Q}t}\, f(0)\rangle\,. \tag{5.26}$$

In this last expression, a new dynamical quantity $\eta^-(t) = \mathrm{e}^{-i\mathcal{L}\mathcal{Q}t}\, f(0)$ appears, as a strange "time reversal" alternative to the noise $\eta(t) = \eta^+(t) = \mathrm{e}^{i\mathcal{Q}\mathcal{L}t}\, g(0)$. The superscripts indicate if the orthogonal dynamics is propagated forward $(+)$ or backward $(-)$ in time. Two algorithms were developed by Carof et al. [144], the forward and the backward ones, considering either the noise $\eta(t)$ or its time reversal counterpart $\eta^-(t)$, respectively. Later on, Lesnicki et al. [9] improved the stability of the method proposed originally in [144] as well as its numerical memory management, leading to a quite complex numerical scheme. We detail now the forward orthogonal algorithm dedicated to the reconstruction of the dynamical quantity $\eta(t)$ from the MD trajectories – for one molecule: $v(t)$ and $f(t)$ via $g(t)$ – that allows upon time cross-correlation (equation 5.26) to get the memory kernel using the more stable version of [9] but in a simpler form.

From the definition of η,

$$\eta(t) = \mathrm{e}^{i\mathcal{Q}\mathcal{L}t}\, g(0)\,, \tag{5.27}$$

one deduces that its dynamics equation is given by

$$\frac{\mathrm{d}\eta}{\mathrm{d}t} = i\mathcal{L}\eta - i\mathcal{P}\mathcal{L}\eta\,, \tag{5.28}$$

instead of the regular Hamiltonian dynamics $\dot{a} = i\mathcal{L}a$ for a dynamical quantity $a(t) = v(t)$ or $f(t)$ generated by MD. It is specifically derived [144] that the noise dynamics deviates from the normal dynamics of $g(t)$ as

$$\eta(t) = g(t) + \int_0^t v(u)\frac{\langle\eta(t-u)f(0)\rangle}{m\langle v(0)^2\rangle}\,\mathrm{d}u \tag{5.29}$$

Considering the dynamics over a timestep δt, after some algebra and noting that for any Hamiltonian quantity $a(t)$ the stationarity ensures that $a(t+\delta t)[\Gamma_0] = a(t)[\Gamma_{\delta t}]$ – which is not the case for the orthogonal variables – with Γ_t denoting the phase space configuration at a time t, we have

$$\eta(t+\delta t)[\Gamma_t] = g(t+\delta t)[\Gamma_{t+\delta t}] + \int_0^{\delta t} v(-u)[\Gamma_{t+\delta t}] \frac{\langle \eta(t+u) f(0) \rangle}{m \langle v(0)^2 \rangle} \mathrm{d}u \,. \tag{5.30}$$

We emphasize that because of its orthogonal dynamics, the noise is not stationary, i.e. $\eta(t+\delta t)[\Gamma_0] \neq \eta(t)[\Gamma_{\delta t}]$, in line with the fact that it precisely encodes memory effects. From there, the integral term can be discretized using a simple first order scheme, but prone to numerical instability, or a second order scheme leading to a stable algorithm [9, 142]. We reproduce the iterative scheme obtained from the second order development to reconstruct the discretized noise dynamics:

$$\eta_{n+1}[l] = g_n[l+1] + \left[\omega_n v_n[l] + \frac{v_n[l-1]}{2 - \delta t \kappa_n} (2\vartheta_n + \zeta_n \omega_n \delta t) \right] \frac{\delta t}{2}, \tag{5.31}$$

for n running from 0 to $N_t - 1$, where $\omega, \kappa, \vartheta$, and ζ corresponds to the following discretized correlation functions

$$\omega_n = \frac{\sum_{l=0}^{N_t-1-n} f_n[l] \eta_n[l]}{m \sum_{l=0}^{N_t-1-n} v_0[l]^2}, \tag{5.32}$$

$$\kappa_n = \frac{\sum_{l=0}^{N_t-1-n} f_n[l] v_n[l]}{m \sum_{l=0}^{N_t-1-n} v_0[l]^2}, \tag{5.33}$$

$$\vartheta_n = \frac{\sum_{l=0}^{N_t-1-n} f_n[l] \eta_n[l+1]}{m \sum_{l=0}^{N_t-1-n} v_0[l]^2}, \tag{5.34}$$

and

$$\zeta_n = \frac{\sum_{l=0}^{N_t-1-n} f_n[l] v_n[l+1]}{m \sum_{l=0}^{N_t-1-n} v_0[l]^2}. \tag{5.35}$$

We stress the fact that, at each iteration n an update is required for both, the denominator and the numerator, of the four quantities. The goal is to reconstruct the dynamics of a fluctuating quantity, not to compute an averaged quantity. Though, at the end, the memory kernel can be obtained from the numerator of κ. This method is more complex and computationally

costly than the previous one, but gives the trajectory of the noise for each fluid molecule and is not restricted to the calculation of the memory kernel, i.e. contributions of the memory kernel from different pieces of the total force could be evaluated as well. Additionally, this method can be applied to obtain the orthogonal dynamics of any quantity, not just the noise.

5.5 | Hydrodynamics from Memory Kernel using Molecular Simulations

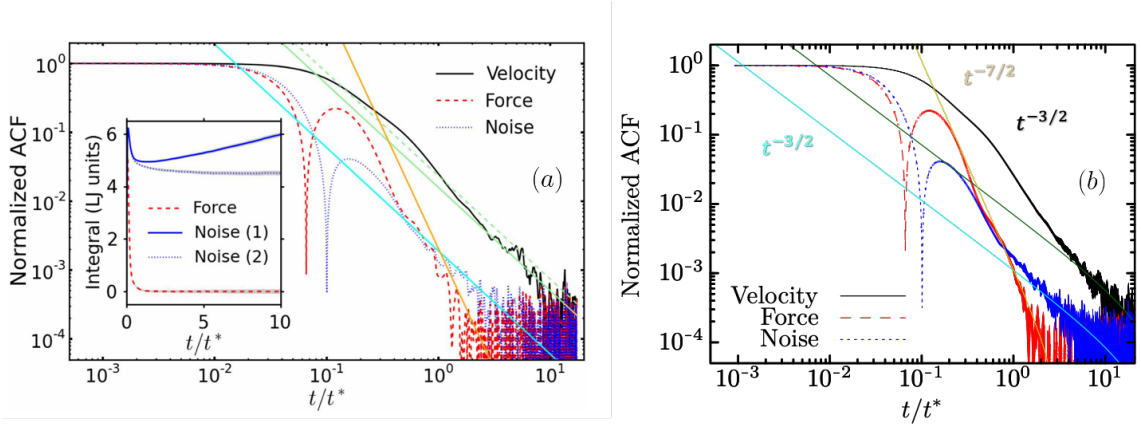

Figure 5.1 | Absolute values of the normalized Velocity, Force, and Noise Auto-Correlation Functions (VACF, FACF, and NACF or memory kernel), as functions of time in LJ units for a bulk LJ fluid. Panel (a) is taken from the work of Lesnicki et al. [9] and panel (b) corresponds to the results we obtained from the Volterra method (for the NACF). The curves correspond to the hydrodynamic theory predictions in the long time limit for the VACF (green lines), $\propto t^{-3/2}$, the FACF (orange line), $\propto t^{-7/2}$, and the NACF (cyan lines), $\propto t^{-3/2}$. The inset of (a) displays the integrals of the FACF (dashed red), converging to zero, and the NACF, diverging with the first order algorithm (solid blue line) and converging to the right value for the friction coefficient ξ with the second order one (dotted blue line). Grey area indicate the error bars. t* is the LJ time for Ar (2.17 ps) and CH_4 (1.346 ps).

Recently, a study based on the memory kernel has proved that in the case of a bulk fluid, hydrodynamic modes govern the long time fluid dynamics even for a molecule of the fluid [9]. As shown in [142], and as can be seen in figure 5.1, the Velocity Auto-Correlation Function (VACF) follows a $t^{-3/2}$ scaling at long times, attributed to hydrodynamic modes. This scaling also arises for Rouse polymer diffusion. It is expected that the Force ACF (FACF) decays faster, ($\propto t^{-7/2}$) than the VACF, being its derivative. The memory kernel, or the Noise ACF (NACF), is also decaying much slower than the FACF representing a delayed version of the total force, and follows the same scaling as the VACF. Interestingly, it follows the same scaling at long times as the VACF. The long tail decays of all the ACFs including memory kernel in the case of a solvent molecule follows the scaling predicted by hydrodynamics for macroscopic colloids diffusion [9, 146, 147].

I aimed first to reproduce their results on the hydrodynamics of a monoatomic fluid (figure 5.1), especially the memory kernel to test the implementation of the algorithms. They used first [144] and second [142] order algorithms based on the orthogonal dynamics to reconstruct the memory kernel with success, but the former did not show sufficient accuracy to compute the diffusion coefficient (inset of figure 5.1). I used the two methods described above based on the inversion of the Volterra equation of the second kind and on the reconstruction of the orthogonal dynamics with second order accuracy, yielding identical results. Later on, in the case of methane in kerogen, I use the former method for efficiency reason.

5.6 | Memory Effects on the Dynamics of a Fluid Confined in Kerogen

In this section, the dynamics of a fluid confined in a microporous kerogen matrix is examined through the ACFs decays obtained on sufficiently long trajectories (100 ns and subdivided in 20 ns long blocks) to have a better understanding of solid-fluid couplings. They are computed in the same way as for the bulk fluid case. Memory kernels are extracted using the inversion of the Volterra equation of the second kind. To investigate the impact of fluid adsorption on the ACFs behaviour, I consider the highest and the lowest methane loading in the immature type I kerogen at 400 K, 25 MPa (figure 5.6). The highly loaded case is investigated first to focus on the effect of the matrix flexibility, i.e. with comparisons between the frozen and the all-atom (flexible) setups, because freezing the matrix in the lowest loading case traps almost all molecules, due to methane adsorption-induced swelling. Then, after discussing different methods to obtain the self-diffusion coefficient from the ACFs, I look at the loading effect on the fluid dynamics with adsorption-induced swelling.

5.6.1 | Flexibility Effects at Constant Volume

Here, the solid's flexibility effects are investigated with time correlation functions and memory kernels on shorter time scales (from a few picoseconds to tens or hundreds of picoseconds) than needed to compute diffusion coefficients from the MSD (from a few nanoseconds to tens of nanoseconds), but involving more statistics. This is accomplished by comparing two treatments of the kerogen matrix at the same volume, when the solid's atoms are completely frozen or can move, by using correlation functions and memory kernel analysis. The corresponding ACFs of velocity, force and projected force (noise) and the cross-correlation function of velocity and force for the immature kerogen model exhibiting flexibility effects and for its rigidified versions are depicted in figure 5.2. The rigidified kerogen systems are obtained from five different configurations of the flexible version of the

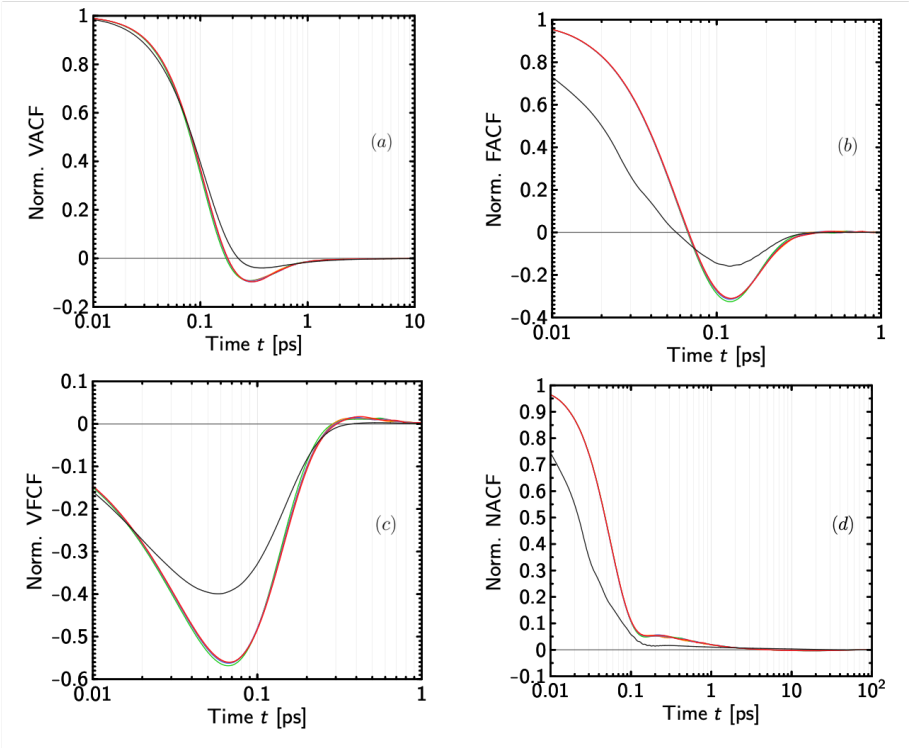

Figure 5.2 | Semi-log graphs of the normalized VACF (a), FACF (b), VFCF (c), and NACF or MK (d) in time for methane in the immature kerogen at high loading for the flexible case (black curves) and rigid case (colored curves). Each of the five different colors of the rigid runs corresponds to a solid configuration taken from the flexible run. Note the different time ranges of the graphs. Five blocks of 20 ns for each run are used for the error bars (95 % confidence interval) that are indicated by grey areas. The time resolution is 10 fs.

kerogen (separated by at least two nanoseconds). The kerogen model was deliberately taken at its maximum swelling in order to avoid pore blocking in the rigidified kerogen versions.

First of all, it can be seen in figure 5.2 that all rigid configurations show similar behavior despite the fact that they represent different geometries of the flexible structure for which the diffusion coefficients are not the same, and lower than in the flexible case. A distinctive feature of a fluid confined in a solid matrix is the negative peak in the VACF, indicating a backscattering effect caused by collisions of fluid particles with the solid walls. Contrary to the bulk fluid previously studied in the supercritical state, this backscattering might appear in the liquid state, or at least when the fluid concentration is large enough. It is less pronounced for the deformable matrix pointing to the importance of flexibility effects, which seem to hinder backscattering effects while strongly impacting the fluid dynamics mechanisms. This is affirmed by the force correlation function, which for the case of the flexible kerogen seems to show softer but slightly longer effects on fluid motions when colliding with solid walls, contributing to the faster force decorrelation. Force and velocity also decorrelate faster, with the first VFCF peak shifted slightly earlier in the flexible case, somehow in contradiction with the memory kernel peak shifted to a longer time.

Other valuable information from a comparison of the rigidified and flexible versions of the kerogen matrix can be obtained from the decays of the correlation functions. In order to comment on its long term decays, I have presented the correlation functions from figure 5.2 on logarithmic scale, taking its normalized and absolute values in the same way as has been used for the bulk fluid study in section 5.5. The different correlation functions for the flexible solid and its five different rigidified configurations are also illustrated in figure 5.3. The shift of the VACF peak is clearly noticeable in this representation compared to the previous one (figure 5.2). As mentioned, the flexibility of the matrix allows a longer interaction with the solid, which manifests itself in a peak shifted to a longer time. However, the decay seems to be identical for both cases at long times, which requires additional statistics to observe the slower decay for the flexible case. The same conditions are required for the FACF. In either case, the more time-intensive solid-fluid couplings induced by the mobility of the solid atoms, results in a faster temporal decorrelation for the force, as well as a less oscillatory pattern. The VFCF has a retarded second peak for the flexible kerogen, as in the VACF, but at the same time it decays similarly to the FACF. For the memory kernel, beyond the shift of the first peak, we note the absence of a second peak in the flexible case as it enters into rapid oscillations after 40 ps. Moreover, it follows a clear intermediary scaling between 0.3 and 8 ps, indicating pronounced flexibility effects imposed by the mechanical relaxation of the solid since the rigid case displays a totally different behaviour with a clear anti-correlation peak.

To compare the long time decays of all correlation functions for each case, flexible and rigid, graphs of these time-dependent functions for two rigidified configurations and the flexible case are shown in figure 5.4.

For the rigid case, the long time VACF decay goes as t^{-1}, which does not correspond to the hydrodynamic scaling ($t^{-3/2}$ scaling), which is shown by the gray dashed line in figure 5.4. For the flexible case, it is between these two scalings ($t^{-1.15}$ scaling, dashed green line in figure 5.4), suggesting that long time decays for fluids confined in amorphous and disordered microporous media stay in between the hydrodynamic and the elastic (rigid) behaviours for the fluid molecule environment. The force ACF obviously decays faster, since the force ACF is the second time derivative of the VACF. The VFCF decays similarly to the FACF, which is different from the memory kernel dynamics, decaying even slower ($t^{-0.43}$ scaling) in the flexible case. For the rigid case, however, the decay is undefined as a characteristic memory kernel anti-correlation peak is formed, which, as discussed below, seems to prevent diffusion coefficients from being computed.

5.6.2 | Transport Coefficient Estimation

The presented analysis of correlation functions and their decays capture well the significant impact of flexibility effects on fluid dynamics and its memory effects. On this basis, the reproducibility of the diffusion coefficient (chapter 3) from relatively small-time

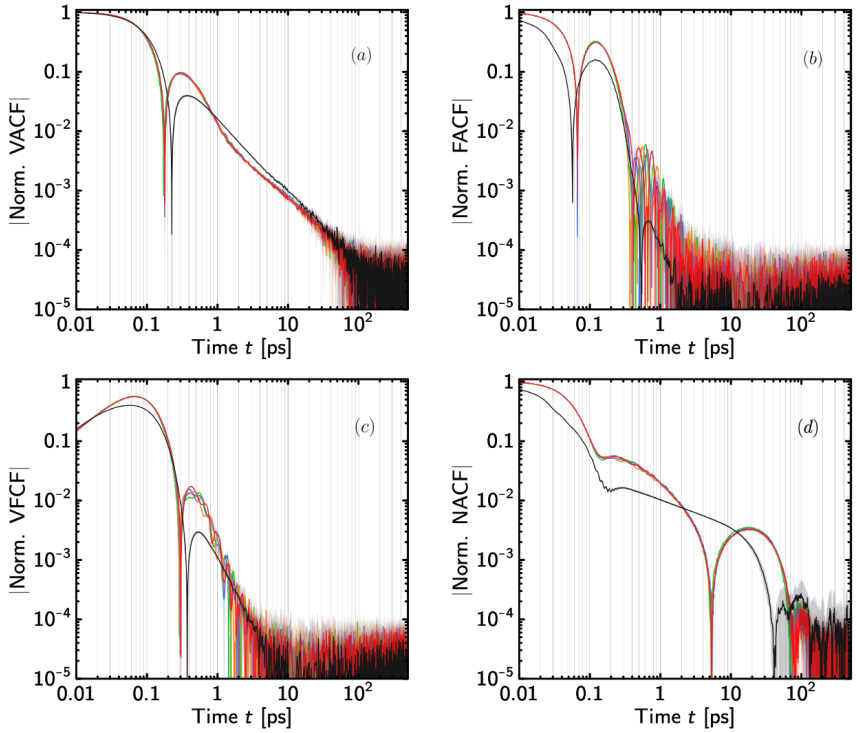

Figure 5.3 | Log-log graphs of the absolute value of the normalized VACF (a), FACF (b), VFCF (c), and NACF or MK (d) in time for methane in the immature kerogen at high loading for the flexible case (black curves) and rigid case (colored curved). The grey areas correspond to the error bars. Contrary to figure 5.2, the time ranges are the same for all the graphs, going up to 500 ps.

scales using correlation functions arises. For this purpose, the ACFs of the velocity, force and noise (projected force) have been taken to compute the diffusion coefficient. Again the rigidified and flexible cases at maximum fluid content are considered, with two rigid configurations taken for the former, showing the fastest and slowest diffusion coefficient of all five configurations.

First, I employed the more direct method of deriving the self-diffusion coefficient, i.e. from the integral of the VACF, in the one-dimensional case (equation 5.36):

$$D(t) = \int_0^t \langle v(u)v(0)\rangle \, \mathrm{d}u \,. \tag{5.36}$$

Then, the self-diffusion coefficient has been calculated as function of ξ via the Einstein relation $D(t) = \frac{k_B T}{\xi(t)}$ from the integral of the FACF as

$$\xi(t) = \frac{1}{k_B T} \int_0^t \langle f(u)f(0)\rangle \, \mathrm{d}u \,, \tag{5.37}$$

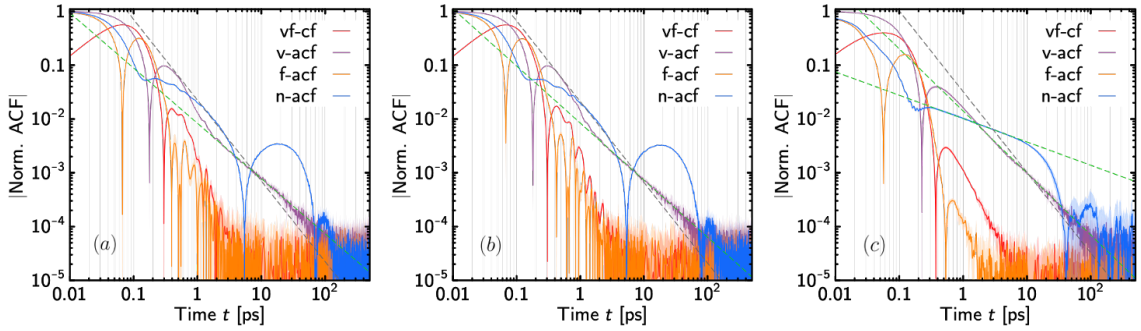

Figure 5.4 | Log-log graphs of the absolute value of the normalized VACF (purple), FACF (orange), VFCF (red), and NACF or memory kernel (blue) in time for methane in the immature kerogen at high loading for two out of the five rigidified configurations (a) and (b), and for the flexible case (c). The long time decay of the VACF follows a t^{-1} scaling for both of the rigidified solid matrix cases and a $t^{-1.15}$ scaling for the flexible case (dashed green line). The dashed grey lines indicate the hydrodynamic scaling $t^{-3/2}$ for comparison. Additionally, in (c), the memory kernel follows an intermediary $t^{-0.43}$ scaling in the flexible matrix (dashed green line).

or the memory kernel as

$$\xi(t) = \int_0^t K(u)\mathrm{d}u\,. \tag{5.38}$$

The obtained diffusion coefficients evolution with time are dispayed in figure 5.5.

The corresponding estimates of the diffusion coefficients by integrating the VACF for all models converge to the estimates obtained by fitting the MSD of the fluid molecules shown by the dashed grey lines. While the MSD evolution of methane molecules converges to a linear regime in which D can be computed after a few hundred picoseconds from trajectories of a few nanoseconds long, to converge to the proper value from the velocity ACF (purple curves in figure 5.5) obtained from trajectory of 20 nanoseconds long requires more than 1 ns for the rigidified kerogen matrices and about 500 ps for the flexible one. While the rigidified configurations exhibiting the slowest ($D = 0.06$ Å^2/ps) diffusivity come to a converging value later than the one showing the fastest ($D = 0.13$ Å^2/ps) diffusivity.

The FACF integral for the diffusion coefficient computation (orange curves in figure 5.5) is not shown for the rigid cases because it is two orders of magnitude above the NACF, which greatly underestimates ξ. However, it does not converge to zero, as in the bulk fluid case, but rather converges to a very small value, resulting in a diffusion coefficient that is too large. Contrary to the bulk fluid case, the integration of the noise ACF for both rigidified kerogen configurations does not allow to correctly estimate the diffusion coefficient. But for the flexible matrix, the memory kernel integral began to approach the proper value of the diffusion coefficient quite quickly, not fully converging within 20 ns. The memory kernel approach reproduces well the diffusion coefficient from the NACF compared to the

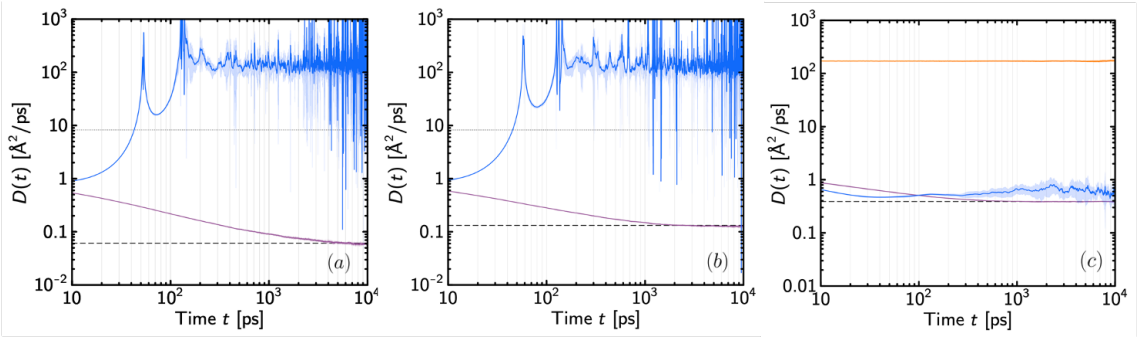

Figure 5.5 | Time evolution of the self-diffusion coefficient estimates obtained through the integration of the MK (blue), VACF (purple), and FACF (orange) for the two rigidified configurations (a) and (b), and the flexible case (c) following the same layout of figure 5.4. The corresponding diffusion coefficients previously evaluated from the mean square displacements are given by the dashed black lines. For the two rigid cases (a) and (b) the diffusion coefficient estimate given from the FACF integral are not shown, this integral going to zero. In the flexible case the corresponding value is shown but is still far off the other values.

FACF for the flexible kerogen, while the diffusion coefficient cannot be obtained at all in the rigidified case. This means that for rigified solid structures, the thermostat, only applied to the fluid, strongly affects the memory of the fluid dynamics, which is crucial to consider.

5.6.3 | Adsorption-Induced Swelling Effect

The effect of adsorption-induced swelling is studied here from the intermediate timescale analysis through the correlation functions of velocity, force and noise (memory kernel). The kerogen systems with minimum (12.1 mg/g) and maximum (82.4 mg/g) methane loading are considered in the flexible case only, including of course the adsorption-induced swelling. The corresponding time correlation functions for both systems are shown in figure 5.6.

The characteristic peak in the VACF for the least swollen case shows a backscattering effect that occurs slightly faster due to stronger interactions with solid atoms. In addition, its long time decay is characterized by larger fluctuations due to lower statistics. Qualitatively, though, the behaviour of the VACF is quite similar in both cases. The FACF and NACF (memory kernel) also show similar behaviours, while the decays are clearer for the most swollen kerogen. The intermediary scaling of the memory kernel noticed earlier also appears for the lowest loading case, but during a shorter period of time, suggesting that this distinct scaling is an intrinsic feature of the kerogen backbone even if modulated in time by the swelling. Such a salient feature is new and cannot be unraveled from the velocity and force time correlation functions. As a consequence, looking at the memory effects of the dynamics of fluids confined in microporous media could allow the investigation of the mechanical relaxation mechanisms of the solid structure. It follows that the flexibility effects

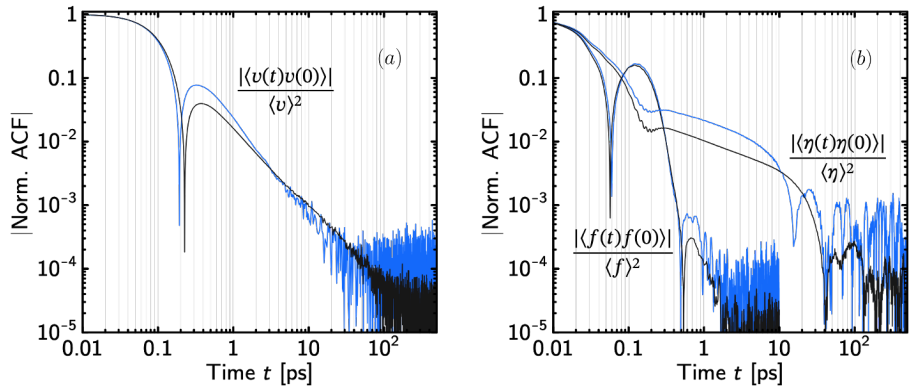

Figure 5.6 | Log-log graphs of the absolute value of the normalized VACF (a), FACF and NACF or MK (b) in time for methane in the immature kerogen at high (black) and low (blue) loading in the flexible case. The FACF is not shown after 10 ps in (b) and the error bars are not displayed for the sake of readability.

are important to account for when studying the confined fluid dynamics and calculating diffusion coefficients from the memory kernels.

5.7 | Conclusion

To better understand the poroelastic solid-fluid couplings at the microscale and, more precisely, the impact of flexibility and adsorption-induced swelling effects on the fluid dynamics, short and intermediate timescales' analysis has been employed, involving correlation functions and memory effects, which preserve information about past fluid dynamics affected by the solid dynamics.

Previously, the study of the memory kernel has been applied mainly to macrosystems, such as colloids. Only recently it has been successfully used for bulk fluid at the molecular level [142], where the authors have identified long time decays of correlation functions and memory kernel from hydrodynamics. However, they emphasized the difficulty of extracting the memory kernel. Consequently, I tested two well-established coarse-graining algorithms to reconstruct the memory kernel and, first, reproduced the results of Lesnicki et al. Both methods yielded very similar results for the memory kernel, but the method proposed in [142] proved to be not as efficient as the one proposed by Jung [133], at the cost of being less flexible.

The second part of the results has been focused on the fluid confined in the microporosity of kerogen. Large statistics accounting for 100 nanosecond long trajectories for the molecular model of kerogen swollen with methane, which has been used to study transport properties in chapter 3, have been employed to capture flexibility and adsorption-induced swelling effects from the behaviour, characteristic peak position and, more importantly, the long time decays of the correlation functions. Five rigidified kerogen configurations obtained

from the flexible one at different time intervals at maximum methane loading have been used to study flexibility effects. The kerogen matrix with adsorbed methane has shown rattling effect in contrast to the bulk fluid, which is more pronounced when the matrix is rigidified. Freezing the solid atoms has failed to quantitatively capture the memory effects, greatly overestimating the diffusion coefficients. The importance of adsorption-induced swelling has been also shown by comparing the most and the least swollen cases (for a given thermodynamic condition) with methane adsorption. Analysis of the ACFs decay has shown that ACFs do not follow the hydrodynamic scaling as opposed to a bulk fluid. The VACF scaling in the flexible kerogen case has been found to lie between the hydrodynamic scaling and the one displayed by the rigid case. The memory kernel for the flexible solid case decays much slower than the VACF and FACF, showing important memory effects that take a longer time to be integrated for the estimation of the friction coefficient.

Reproducing the diffusion coefficient from the intermediate timescale was successful from the integral of the VACF for both cases, flexible and rigidified solids. However, the rigidity of the kerogen matrix resulted in longer convergence times to the correct value. In addition, it should be noticed that although all five rigidified configurations have shown fairly similar results for the correlation functions and memory kernel analysis, the diffusion coefficients reproduced from these VACFs showed different values because of the different geometries implied from frozen snapshots of the long evolution of the flexible matrix. To test the reproducibility of the diffusion coefficient, rigid kerogen configurations were chosen that yielded the slowest and fastest diffusion. It was not possible to extract the diffusion coefficient value from the FACF, especially from the rigid configurations, which significantly overestimated their values. Integration of the memory kernel led to relatively better results for the kerogen case with frozen atoms, still significantly overestimating the diffusion coefficients by several orders of magnitude with large fluctuations. A good estimation has been obtained in the flexible case. Remarkably, it approached the correct value in ~ 20 picoseconds, which is extremely fast, albeit not converging accurately to the MSD estimate after 20 ns, as opposed to the VACF integral estimate.

This introduction of short and intermediate timescale analysis of a microscale confined fluid has raised many challenges. First of all, the presented results have provided a new insight on solid-fluid couplings affected by flexibility effects. However, it questions on the of applicability to other small fluid molecules, such as carbon dioxide, and other atomistic models of kerogen, fluid mass effects, etc. It has been shown that the efficiency of memory kernel extraction still needs to be improved, which implies the development of new and/or improved algorithms. Moreover, this analysis required a very large amount of memory in data generation and processing, but did not allow for accurate reproduction of the diffusion coefficients from the memory kernels, which should also be resolved in further research. This may also be due to size effects from the molecular models used, which will be more crucial when considering mature and overmature kerogen models. Either way, this type of coarse-graining technique based on memory kernel reconstruction, which is already widely

used for large systems, shows great promise for atomic-level systems, and we believe it will provide more fundamental information for rationalizing fluid transport in microporous materials such as kerogen in a near future. More globally, it will help to understand fluid dynamics at the atomistic level, where dynamical properties are crucial.

Chapter 6

General Conclusions and Perspectives

Contents

This chapter summarizes the main results and proposals for further research that emerge from this work, and a brief recap of the purpose of the present study is provided at the beginning.

6.1 | Motivation Recall

In the context of enhancing hydrocarbon recovery from shale and carbon dioxide sequestration in shale, most experimental and numerical studies have focused on adsorption experiments, while transport has attracted less attention, although it is a major indicator of the success of the aforementioned geological processes.

The present work addresses the most recent researches on fluid transport in kerogen, accounting for the effects of the solid flexibility, which have long been neglected. The poroelasticity of kerogen has shown important adsorption-induced swelling effects that dramatically change fluid transport behaviour. However, due to the study of mainly fluid transport trends and the lack of data for a more fundamental understanding of transport in kerogen exhibiting flexibility, we have thus aimed to shed light on this aspect by using molecular dynamics simulations involving statistically intensive atomistic calculations. In addition, in the last chapter, I presented an introduction to the memory kernel study as a first attempt to upscale microscopic fluid transport in kerogen to the mesoscale from memory effects.

6.2 | Transport within Microporous Flexible Organic Matter

Using MD simulations, I first have shown, based on the pore-volume analysis, that oil- and gas-bearing kerogens exhibit significant adsorption-induced swelling not only for immature kerogen but also for the mature one. Sufficiently long trajectories of up to 50 nanoseconds have allowed to determine the impact of important solid's flexibility effects on fluid-fluid cross-correlations. It has been proven for the first time on two kerogen models with adsorbed methane and carbon dioxide, and for a variety of thermodynamic conditions that kerogen flexibility has a minor impact on the collective effects, thereby indicating the totally diffusive nature of fluid transport. This indicates that the transport properties within the flexible kerogen microporosity can be studied while computing only the self-diffusion coefficient, which is computationally easier to obtain.

Based on the previous results, only self-diffusion coefficient have been computed to provide the transport trends. It has been shown for a wide range of conditions including statistically robust atomistic trajectories for the two kerogen models and fluid types, that adsorption-induced swelling leads to transport enhancement contrary to most studies where

kerogen has been represented as rigidified. This increase has been well explained by the increase in the accessible free volume.

The 'imitation' of carbon dioxide sequestration by replacing methane with carbon dioxide in the kerogen model has resulted in the shrinkage of the kerogen model accompanied by relatively large non-affine displacements caused by solid's deformations during volume adaptation to the adsorbed fluid. A comparison between both fluids has shown that carbon dioxide diffuses slower than methane because of the stronger solid-fluid couplings.

Finally, the representative size of atomistic models in the context of transport studies has been discussed. Our kerogen model has proven to be suitable for transport modeling, even though it induces slightly anisotropic transport properties.

6.3 | Rationalization of Transport with the Free Volume Theory

Thanks to the large set of statistically reliable diffusion data obtained and their perfect correlation with the accessible free volume, I proposed in this work to rationalize the adsorption-induced increase in transport using a free volume theory. The free volume model has perfectly captured methane transport trends with fluid loading. Moreover, it has successfully described the transport increase of the more energetically dense fluid, carbon dioxide, for conditions, relevant to those of gas shale reservoirs. The model has demonstrated good agreement for both fluids confined in kerogen through analysis of its parameters, such as the free volume parameter and the friction coefficient, suggesting its applicability to other fluids, such as longer-chain hydrocarbons and their mixtures in microporous kerogen to describe fluid transport, influenced by the solid's flexibility effects.

6.4 | Towards Transport Upscaling from Memory Kernels

Aiming to extend the study to larger-than-atomistic scales, say to mesoscopic pores, of flexibility effects affecting fluid dynamics, I introduced a memory kernel study that allows one to extract the impact of solid-state dynamics on fluid dynamics. Involving two reconstruction algorithms to compute the memory kernel, I have shown the importance of accounting for the kerogen viscoelastic nature and adsorption-induced swelling from the correlation functions analysis, again involving robust statistics (100 nanoseconds trajectories). It has been demonstrated that the rigid solid approximation leads to a significant overestimation of the diffusion coefficients from memory effects, while consideration of the kerogen flexibility yields a good estimate of it.

6.5 | General Conclusion and Outlook

Overall, this work contributes greatly to the building of a general theory of transport in microporous kerogen, accounting for flexibility effects. These results should also be applicable to fluid mixtures. Among geological applications, such as the enhanced production of gas and oil and the sequestration of greenhouse gases, the results should also be applicable to any microporous material subject to adsorption-induced deformations. Nevertheless, this work raises a number of challenges for further research, some of which are presented below.

- For simplicity and in the interest of characterizing the poromechanical properties of kerogen and its flexibility, we considered our kerogen models to be compositionally simple, i.e. containing only the carbon and hydrogen atoms. It is worth studying kerogen with more complex composition to observe the impact of other elements, such as oxygen, nitrogen, and sulfur, on adsorption-induced swelling for different types of adsorbed fluid.
- More globally, the next step in rationalizing fluid transport in kerogen would be to consider, together with flexibility effects, other transport phenomena induced by ultra-confinement, such as slippage, wettability, etc., that may arise while considering the impact of mesopores on transport.
- With respect to the raised issue about the representative size of the atomistic kerogen model, it will be valuable to have a better understanding of the anisotropic effects, balancing model realism and the resulting computational costs.
- The proper upscaling of fluid transport at the microscale to understand an impact of mesoscale inhomogenities, as well as kerogen's poroelasticity and adsorption-induced swelling at the mesoscale is another challenge.
- Finally, a promising study on fluid dynamics involving non-Markovian effects at short and intermediate timescales, which has been introduced for the first time in this work for confined fluid dynamics at the microscale, will provide insights into the effects of the solid dynamics on fluid one. However, the demonstrated introduction to this study needs to be extended. It is necessary, therefore, to test on other fluids, such as the more energetically dense carbon dioxide, and to consider the mass effect and to rationalize the computationally inefficient reproduction of transport coefficients from the memory kernel. Moreover, this requires the development of efficient memory kernel reconstruction algorithms.

Chapter A

Appendix

Contents

A.1 | Replacement of Methane with Carbon Dioxide

In order to obtain atomistic models of immature kerogen with carbon dioxide a molar replacement of methane with this fluid has been carried out for all kerogen models with adsorbed methane at temperatures 300 K and 400 K and pressures of 0.1 MPa, 25 MPa and 100 MPa. The time-equilibrated part of the density fluctuations induced after this replacement is shown for the lowest fluid loading (33.4 mg/g) at temperatures 300 K and 400 K and pressures of 0.1 MPa and 100 MPa in figure A.1.

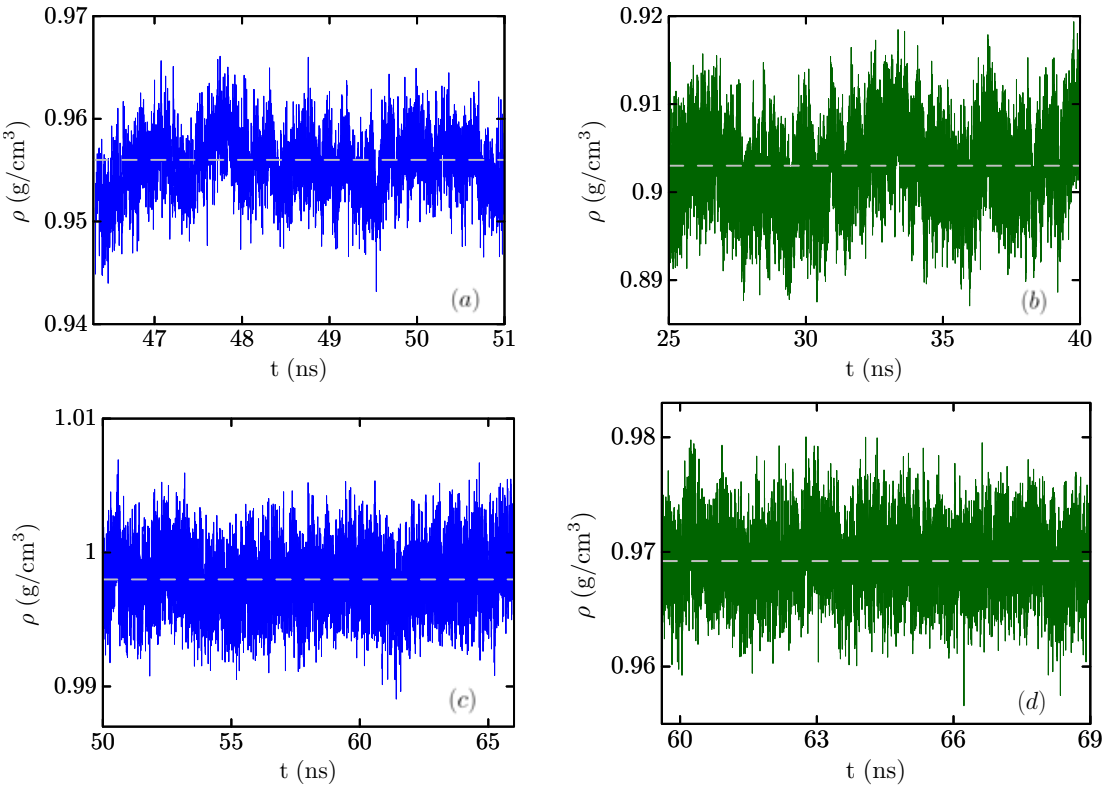

Figure A.1 | Density fluctuations of the equilibrated matrix volume of the kerogen matrix during NPT MD simulation after per-molecule replacement of 80 CH_4 molecules with CO_2 molecules at a pressure of 0.1 MPa and temperatures of (a) 300 K and (b) 400 K and a pressure of 100 MPa and temperatures of (c) 300 K and (d) 400 K. Dotted lines show the average density value.

A.2 | Fluid Transport Affected by Anisotropy

An atomistic model of immature kerogen of about $6 \times 6 \times 6\ nm^3$ shows slightly anisotropic transport properties. The effect of this anisotropy on transport is illustrated for both fluids,

methane (figure A.2) and carbon dioxide (figure A.3) with an anisotropic factor, where diffusion coefficients are considered separately along the x, y and z directions.

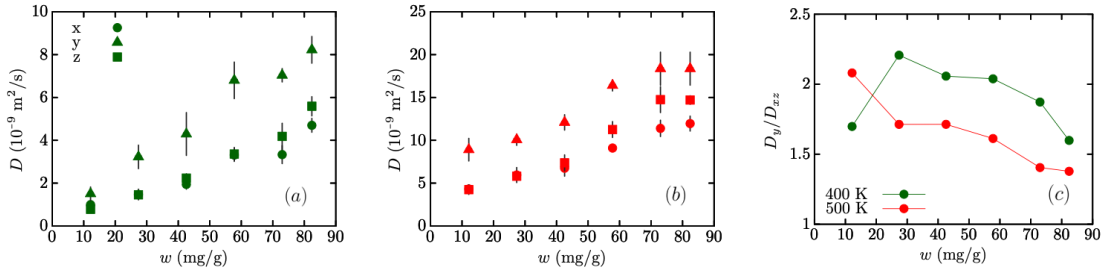

Figure A.2 | Methane self-diffusion coefficients along x, y and z directions at temperatures of 400 K (a) and 500 K (b) and at a pressure of 0.1 MPa and anisotropic factor (c) defined as the ratio of the diffusion coefficient in the y direction over the average difusion coefficient in the two other directions as function of the fluid loading for two different temperatures and a pressure of 0.1 MPa, which proves that the transport properties can be considered isotropic by averaging along x, y and z directions.

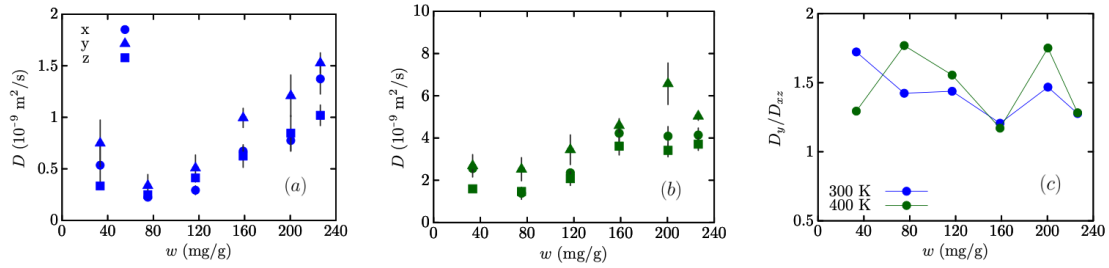

Figure A.3 | Carbon dioxide self-diffusion coefficients along x, y and z directions at temperatures of 300 K (a) and 400 K (b) and at a pressure of 0.1 MPa and anisotropic factor (c) defined as the ratio of the diffusion coefficient in the y direction over the average difusion coefficient in the two other directions as function of the fluid loading for two different temperatures and a pressure of 0.1 MPa, which proves that the transport properties can be considered isotropic by averaging along x, y and z directions.

A.3 | Free Volume Model for Carbon Dioxide Transport in Immature Kerogen

Initially, the free volume model has been applied in the implementation of an arithmetic averaging of the free volume parameters over five different system configurations. However, for an ultra-confining pressure of 100 MPa, it has not allowed the averaging curve to be correctly described as shown in figures A.4 and A.5 for the carbon dioxide and methane probes correspondingly, due to the nonlinearity of the model. This has been overcome in

the free volume modelling by excluding one of the five independent determinations of the free volume parameters in the averaging procedure.

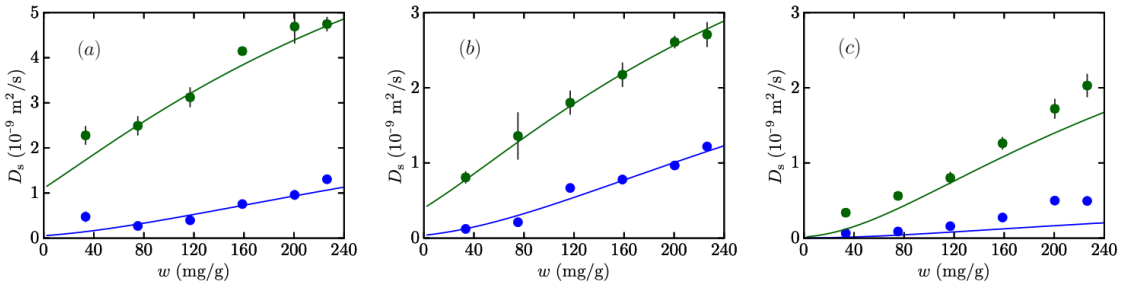

Figure A.4 | Evolution of the self-diffusion coefficient with the carbon dioxide loading for 300 and 400 K and three different pressures: (a) 0.1, (b) 25 and (c) 100 MPa. The solid curves correspond to the free volume model based on the obtained parameters (figure 4.5) and the parameters $\alpha(T,P)$ and $\xi(T,P)$ estimated from a best fit procedure and collected in figure 4.7.

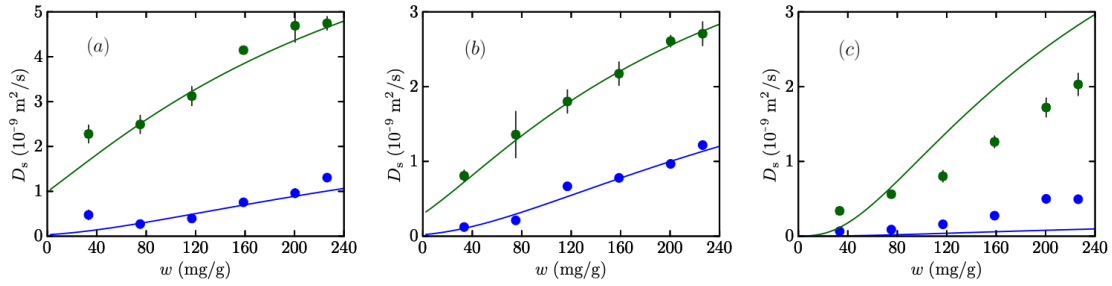

Figure A.5 | Evolution of the self-diffusion coefficient with the carbon dioxide loading for 300 and 400 K and three different pressures: (a) 0.1, (b) 25 and (c) 100 MPa. The solid curves correspond to the free volume model based on the obtained parameters (figure 4.8) and the parameters $\alpha(T,P)$ and $\xi(T,P)$ estimated from a best fit procedure and collected in figure 4.10.

A.4 | Comparison of Correlation Functions for Flexible and Rigidified Kerogen

In the framework of a memory kernel study applied to an immature kerogen model with methane adsorbed at maximum loading (82.4 mg/g), a kerogen matrix exhibiting flexibility effects and its counterpart (a totally rigid matrix) at the same volume have been compared. The correlation functions of velocity, force and projected force (noise) as well as the cross-correlation function of velocity and force for both models are demonstrated in figure A.6.

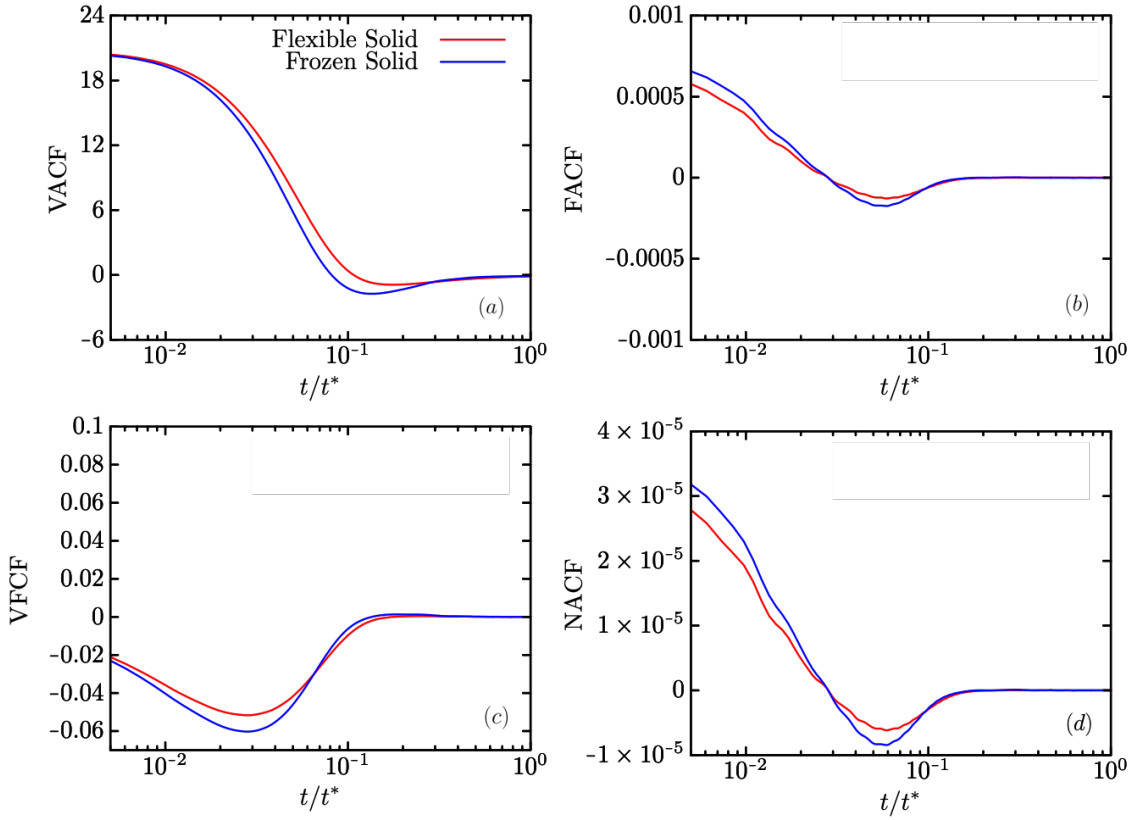

Figure A.6 | Semi-log graphs of the VACF in Å^2/ps^2 (a), FACF in eV^2/ Å^2 (b), VFCF in eV/ps (c), and NACF in g/(mole ps^2) (d) in time (LJ units) for methane in the immature kerogen at high loading for the flexible case (red) and rigid case (blue).

Bibliography

[1] Jeffrey S. Seewald. Organic–inorganic interactions in petroleum-producing sedimentary basins. Nature, 426:327–333, 2003.

[2] Amaël Obliger, Pierre-Louis Valdenaire, Nicolas Capit, Franz J. Ulm, Roland J.-M. Pellenq, and Jean-Marc Leyssale. Poroelasticity of methane-loaded mature and immature kerogen from molecular simulations. Langmuir, 34(45):13766–13780, 2018.

[3] Colin Bousige, Camélia Matei Ghimbeu, Cathie Vix-Guterl, Andrew E. Pomerantz, Assiya Suleimenova, Gavin B. M. Vaughan, Gastón Garbarino, Mikhail Feygenson, Christoph U Wildgruber, Franz-Josef Ulm, Roland J.-M. Pellenq, and Benoît Coasne. Realistic molecular model of kerogen's nanostructure. Nature materials, 15:576–82, 2016.

[4] Julien Collell, Philippe Ungerer, Guillaume Galliero, Marianna Yiannourakou, François Montel, and Magali Pujol. Molecular simulation of bulk organic matter in type II shales in the middle of the oil formation window. Energy & Fuels, 28(12):7457–7466, 2014.

[5] Julien Collell, Guillaume Galliero, Romain Vermorel, Philippe Ungerer, Marianna Yiannourakou, François Montel, and Magali Pujol. Transport of multicomponent hydrocarbon mixtures in shale organic matter by molecular simulations. Journal of Physical Chemistry C, 119(39):22587–22595, 2015.

[6] Kerstin Falk, Benoit Coasne, Roland Pellenq, Franz-Josef Ulm, and Lyderic Bocquet. Subcontinuum mass transport of condensed hydrocarbons in nanoporous media. Nature communications, 6:1–7, 2015.

[7] Amaël Obliger, Pierre-Louis Valdenaire, Franz-Josef Ulm, Roland J.-M. Pellenq, and Jean-Marc Leyssale. Methane diffusion in a flexible kerogen matrix. The Journal of Physical Chemistry B, 123(26):5635–5640, 2019.

[8] Lev D. Gelb and Keith E. Gubbins. Pore size distributions in porous glasses : A computer simulation study. Langmuir, 15:305–308, 1999.

[9] Dominika Lesnicki, Rodolphe Vuilleumier, Antoine Carof, and Benjamin Rotenberg. Molecular hydrodynamics from memory kernels. Physical review letters, 116:1–5, 2016.

[10] Lydia B. Ytzhak, Laure Cailloce, and Yaroslav Pigenet. Gas, energy of transition? CNRS International Magazine, 35:18–27, 2014.

[11] Bob Dudley. BP Statistical Review of World Energy 2014, 2014.

[12] Dirk Willem van Krevelen. Coal: Typology - Physics - Chemistry - Constitution. Elsevier, 1993.

[13] Bernard Durand. Kerogen, Insoluble Organic Matter from Sedimentary Rocks. Editions Technip, 1980.

[14] Amaël Obliger, Roland Pellenq, Franz-Josef Ulm, and Benoit Coasne. Free volume theory of hydrocarbon mixture transport in nanoporous materials. The Journal of Physical Chemistry Letters, 7(19):3712–3717, 2016.

[15] Zhouhua Wang, Yun Li, Huang Liu, Fanhua Zeng, Ping Guo, and Wei Jiang. Study on the adsorption, diffusion and permeation selectivity of shale gas in organics. Energies, 10(1):1–15, 2017.

[16] S. Reza Etminan, Farzam Javadpour, Brij B. Maini, and Zhangxin Chen. Measurement of gas storage processes in shale and of the molecular diffusion coefficient in kerogen. International Journal of Coal Geology, 123:10–19, 2014.

[17] Athumani Omari, Chao Wang, Yang Li, and Xingguang Xu. The progress of enhanced gas recovery (egr) in shale gas reservoirs: A review of theory, experiments, and simulations. Journal of Petroleum Science and Engineering, 213:110461, 2022.

[18] Tongwei Zhang, Geoffrey S. Ellis, Stephen C. Ruppel, Kitty Milliken, and Rongsheng Yang. Effect of organic-matter type and thermal maturity on methane adsorption in shale-gas systems. Organic Geochemistry, 47:120–131, 2012.

[19] Huangjing Zhao, Tianhao Wu, and Abbas Firoozabadi. High pressure sorption of various hydrocarbons and carbon dioxide in kimmeridge blackstone and isolated kerogen. Fuel, 224:412–423, 2018.

[20] Levent Ballice. Solvent swelling studies of göynük (kerogen type-i) and beypazarı oil shales (kerogen type-ii). Fuel, 82(11):1317–1321, 2003.

[21] Thomas Rexer, Eliza Mathia, Andrew Aplin, and Keith Thomas. High-pressure methane adsorption and characterization of pores in posidonia shales and isolated kerogens. Energy & Fuels, 28:2886–2901, 2014.

[22] Yue Feng, Xianming Xiao, Enze Wang, Jian Sun, and Ping Gao. Oil retention in shales: A review of the mechanism, controls and assessment. Frontiers in Earth Science, 9, 2021.

[23] Michele Moisio Thomas and Jamie A. Clouse. Primary migration by diffusion through kerogen: I. model experiments with organic-coated rocks. Geochimica et Cosmochimica Acta, 54(10):2775–2779, 1990.

[24] Michele Moisio Thomas and Jamie A. Clouse. Primary migration by diffusion through kerogen: Ii. hydrocarbon diffusivities in kerogen. Geochimica et Cosmochimica Acta, 54(10):2781–2792, 1990.

[25] Ravinath Kausik, Kamilla Fellah, Ling Feng, Denise Freed, and Gary Simpson. High- and low-field nmr relaxometry and diffusometry of the bakken petroleum system. 2016.

[26] J.-P. Korb, B. Nicot, and I. Jolivet. Dynamics and wettability of petroleum fluids in shale oil probed by 2d t1-t2 and fast field cycling nmr relaxation. Microporous and Mesoporous Materials, 269:7–11, 2018.

[27] Yanbin Yao, Jun Liu, Dameng Liu, Jiyu Chen, and Zhejun Pan. A new application of nmr in characterization of multiphase methane and adsorption capacity of shale. International Journal of Coal Geology, 201:76–85, 2019.

[28] Guangzhao Zhou, Zhiming Hu, Zhaobin Gu, Jin Chang, Xianggang Duan, Xiangui Liu, and Hongming Zhan. Low-field nmr investigation of the dynamic adsorption-desorption process of shale gas. Energy and Fuels, 35(6):4762 – 4774, 2021.

[29] Jordan R. Nelson. Determination of molecular weight between crosslinks of coals from solvent-swelling studies. Fuel, 62(1):112–116, 1983.

[30] Thomas K. Green, Jeffrey Kovac, and John W. Larsen. A rapid and convenient method for measuring the swelling of coals by solvents. Fuel, 63(7):935–938, 1984.

[31] Katarzyna Czerw, Katarzyna Zarębska, Bronisław Buczek, and Paweł Baran. Kinetic models assessment for swelling of coal induced by methane and carbon dioxide sorption. Adsorption, 22(4-6):791 – 799, 2016.

[32] Ang Liu, Peng Liu, and Shimin Liu. Gas diffusion coefficient estimation of coal: A dimensionless numerical method and its experimental validation. International Journal of Heat and Mass Transfer, 162, 2020.

[33] Peng Liu, Yongdong Jiang, and Boxue Fu. A novel approach to characterize gas flow behaviors and air leakage mechanisms in fracture-matrix coal around in-seam drainage borehole. Journal of Natural Gas Science and Engineering, 77:103243–103268, 2020.

[34] Assiya Suleimenova, Kyle D. Bake, Aysen Ozkan, John J. Valenza, Robert L. Kleinberg, Alan K. Burnham, Nicola Ferralis, and Andrew E. Pomerantz. Acid demineralization with critical point drying: A method for kerogen isolation that preserves microstructure. Fuel, 135:492–497, 2014.

[35] Hanyu Zhang, M Ahmed, and Jin Zhan. Recent advances in molecular simulation of oil shale kerogen. Fuel, 2022.

[36] Alexandru Botan, Romain Vermorel, Franz-Josef Ulm, and Roland J.-M. Pellenq. Molecular simulations of supercritical fluid permeation through disordered microporous carbons. Langmuir, 29(32):9985–9990, 2013.

[37] Lea Atmani, Christophe Bichara, Roland J.-M. Pellenq, Henri Van Damme, Adri C. T. van Duin, Zamaan Raza, Lionel A. Truflandier, Amaël Obliger, Paul G. Kralert, Franz J. Ulm, and Jean-Marc Leyssale. From cellulose to kerogen: molecular simulation of a geological process. Chemical Science, 8:8325–8335, 2017.

[38] Philippe Ungerer, Julien Collell, and Marianna Yiannourakou. Molecular modeling of the volumetric and thermodynamic properties of kerogen: Influence of organic type and maturity. Energy & Fuels, 29(1):91–105, 2015.

[39] Xin Ru, Zhiqiang Cheng, Lihua Song, Hongyan Wang, and Junfeng Li. Experimental and computational studies on the average molecular structure of chinese huadian oil shale kerogen. Journal of Molecular Structure, 1030:10–18, 2012.

[40] Xiao-Hui Guan, Yao Liu, Di Wang, Qing Wang, Ming-Shu Chi, Shuang Liu, and Chun-Guang Liu. Three-dimensional structure of a huadian oil shale kerogen model: An experimental and theoretical study. Energy & Fuels, 29:4122–4136, 2015.

[41] Liang Huang, Zhengfu Ning, Qing Wang, Rongrong Qi, Jing Li, Yan Zeng, Hongtao Ye, and Huibo Qin. Thermodynamic and structural characterization of bulk organic matter in chinese silurian shale: Experimental and molecular modeling studies. Energy & Fuels, 31:4851–4865, 2017.

[42] Yu Liu, Shimin Liu, Rui Zhang, and Yu Zhang. The molecular model of marcellus shale kerogen: Experimental characterization and structure reconstruction. International Journal of Coal Geology, 246:1–18, 2021.

[43] Shuo Pan, Huaiyu Zhou, Qing Wang, Jingru Bai, Da Cui, and Xinmin Wang. Experimental and molecular simulation studies of huadian oil shale kerogen. ACS Omega, 7(20):17253–17269, 2022.

[44] Lukáš Michalec and Martin Lísal. Molecular simulation of shale gas adsorption onto overmature type ii model kerogen with control microporosity. Molecular Physics, 115:1–18, 2016.

[45] Manolis Vasileiadis, Loukas D. Peristeras, Konstantinos D. Papavasileiou, and Ioannis G. Economou. Modeling of bulk kerogen porosity: Methods for control and characterization. Energy & Fuels, 31:6004–6018, 2017.

[46] Lea Atmani, Pierre-Louis Valdenaire, Roland Pellenq, Christophe Bichara, Henri Van Damme, Adri van Duin, Franz-Josef Ulm, and Jean-Marc Leyssale. Simulating the geological fate of terrestrial organic matter: Lignin vs cellulose. Energy & Fuels, 34(2):1537–1547, 2020.

[47] Jean-Marc Leyssale, Pierre-Louis Valdenaire, Kévin Potier, and Roland J.-M. Pellenq. Replica exchange molecular dynamics simulation of organic matter evolution: from lignin to overmature type III kerogen. Energy Fuels, 2022.

[48] Bernard P. Tissot and Dietrich H. Welte. Petroleum Formation and Occurrence. Springer Berlin, 1984.

[49] Dandan Duan, Dainan Zhang, Xiaoxuan Ma, Yu Yang, Yong Ran, and Jingdong Mao. Chemical and structural characterization of thermally simulated kerogen and its relationship with microporosity. Marine and Petroleum Geology, 89:4–13, 2018.

[50] Jeremie Berthonneau, Amaël Obliger, Pierre-Louis Valdenaire, Olivier Grauby, Daniel Ferry, Damien Chaudanson, Pierre Levitz, Jae Kim, Franz-Josef Ulm, and Roland Pellenq. Mesoscale structure, mechanics, and transport properties of source rocks' organic pore networks. Proceedings of the National Academy of Sciences, 115:12365–12370, 2018.

[51] Julien Collell, Guillaume Galliéro, Francois Michel Gouth, Franċois Montel, Magali Pujol, Philippe Ungerer, and Marianna Yiannourakou. Molecular simulation and modelisation of methane/ethane mixtures adsorption onto a microporous molecular model of kerogen under typical reservoir conditions. Microporous and Mesoporous Materials, 197:194–203, 2014.

[52] Shuai He, Yang Jiang, Jacinta C. Conrad, and Guan Qin. Molecular simulation of natural gas transport and storage in shale rocks with heterogeneous nano-pore structures. Journal of Petroleum Science and Engineering, 133:401–409, 2015.

[53] Kerstin Falk, Roland Pellenq, Franz Josef Ulm, and Benoît Coasne. Effect of chain length and pore accessibility on alkane adsorption in kerogen. Energy & Fuels, 29(12):7889–7896, 2015.

[54] Tuan Anh Ho, Yifeng Wang, and Louise J. Criscenti. Chemo-mechanical coupling in kerogen gas adsorption/desorption. Physical Chemistry Chemical Physics, 20:12390–12395, 2018.

[55] Saad Alafnan and Theis Solling. Effect of kerogen thermal maturity on methane adsorption capacity: A molecular modeling approach. Molecules, 25:1–14, 2020.

[56] The Impact of Kerogen Structure on Shale Permeability: Coupled Molecular Diffusion and Geomechanical Behavior Study. SPE Annual Technical Conference and Exhibition, 2021.

[57] Runxi Wang, Jun Li, Livio Gibelli, Zhaoli Guo, and Matthew K. Borg. Sub-nanometre pore adsorption of methane in kerogen. Chemical Engineering Journal, 426:1–9, 2021.

[58] Hongxin Wu, Long Wen, Li Zhang, Dongbo Wang, Nong Li, and Mingli Yang. Gas adsorption capacity of type-kerogen at a varying burial depth. Energy & Fuels, 2022.

[59] Tianyi Zhao, Xiangfang Li, Huawei Zhao, and Meifen Li. Molecular simulation of adsorption and thermodynamic properties on type II kerogen: Influence of maturity and moisture content. Fuel, 190:198–207, 2017.

[60] Tianyi Zhao, Xiangfang Li, Zhengfu Ning, Huawei Zhao, and Meifen Li. Molecular simulation of methane adsorption on type II kerogen with the impact of water content. Journal of Petroleum Science and Engineering, 161:302–310, 2018.

[61] Wenxi Ren, Jianchun Guo, Fanhui Zeng, and Tianyu Wang. Modeling of high-pressure methane adsorption on wet shales. Energy & Fuels, 33:7043–7051, 2019.

[62] Leebyn Chong, Sean Sanguinito, Angela L. Goodman, and Evgeniy M. Myshakin. Molecular characterization of carbon dioxide, methane, and water adsorption in micropore space of kerogen matrix. Fuel, 283:84–92, 2021.

[63] Jiawei Li, Wang Yuzhu, Zhixi Chen, and Sheikh Rahman. Insights into the molecular competitive adsorption mechanism of ch4/co2 in a kerogen matrix in the presence of moisture, salinity, and ethane. Langmuir, 37(43):12732–12745, 2021.

[64] Amaël Obliger, Franz-Josef Ulm, and Roland Jean-Marc Pellenq. Impact of nanoporosity on hydrocarbon transport in shales' organic matter. Nano Letters, 18:832 – 837, 2018.

[65] Kai Bin Yu, Geoffrey M. Bowers, Narasimhan Loganathan, Andrey G. Kalinichev, and A. Ozgur Yazaydin. Diffusion behavior of methane in 3d kerogen models. Energy & Fuels, 35(20):16515–16526, 2021.

[66] Alexandru Botan, Benjamin Rotenberg, Virginie Marry, Pierre Turq, and Benoit Noetinger. Carbon dioxide in montmorillonite clay hydrates: Thermodynamics, structure, and transport from molecular simulation. Journal of Physical Chemistry C, 114:14962–14969, 2010.

[67] Fouad Oulebsir, Romain Vermorel, and Guillaume Galliero. Diffusion of supercritical fluids through single-layer nanoporous solids: Theory and molecular simulations. Langmuir, 34(2):561–571, 2018.

[68] Julien Collell and Guillaume Galliero. Determination of the thermodynamic correction factor of fluids confined in nano-metric slit pores from molecular simulation. The Journal of chemical physics, 140:1–7, 2014.

[69] Thomas Lee, Lydéric Bocquet, and Benoit Coasne. Activated desorption at heterogeneous interfaces and long-time kinetics of hydrocarbon recovery from nanoporous media. Nature Communications, 7:1–10, 2016.

[70] Stéphane Tesson and Abbas Firoozabadi. Deformation and swelling of kerogen matrix in light hydrocarbons and carbon dioxide. The Journal of Physical Chemistry C, 123(48):29173–29183, 2019.

[71] Saad Alafnan, Yusuf Falola, Osamah Al Mansour, Khalid L. Alsamadony, Abeeb A. Awotunde, and Murtada Saleh Aljawad. Enhanced recovery from organic-rich shales through carbon dioxide injection: Molecular-level investigation. Energy & Fuels, 34(12):16089–16098, 2020.

[72] Sen Wang, Xinyu Yao, Qihong Feng, Farzam Javadpour, Yuxuan Yang, Qingzhong Xue, and Xiaofang Li. Molecular insights into carbon dioxide enhanced multi-component shale gas recovery and its sequestration in realistic kerogen. Chemical Engineering Journal, 425:1–17, 2021.

[73] Jian Wu, Pengyu Huang, Federico Maggi, and Luming Shen. Effect of sorption-induced deformation on methane flow in kerogen slit pores. Fuel, 325:124886, 2022.

[74] Laurent Brochard, Matthieu Vandamme, and Roland J.-M. Pellenq. Poromechanics of microporous media. Journal of the Mechanics and Physics of Solids, 60(4):606–622, 2012.

[75] Laurent Brochard, Matthieu Vandamme, Roland J. M. Pellenq, and Teddy Fen-Chong. Adsorption-induced deformation of microporous materials: Coal swelling induced by co_2-ch_4 competitive adsorption. Langmuir, 28:2659–2670, 2012.

[76] Perla B. Balbuena, David Berry, and Keith E. Gubbins. Solvation pressures for simple fluids in micropores. The Journal of Physical Chemistry, 97(4):937–943, 1993.

[77] Piotr Kowalczyk, Alina Ciach, and Alexander V Neimark. Adsorption-induced deformation of microporous carbons: pore size distribution effect. Langmuir, 24(13):6603–6608, 2008.

[78] Kan Yang, Xiancai Lu, Yangzheng Lin, and Alexander Neimark. Deformation of coal induced by methane adsorption at geological conditions. Energy & Fuels, 24:5955–5964, 2010.

[79] Jekaterina Jeromenok and Jens Weber. Restricted access: On the nature of adsorption/desorption hysteresis in amorphous, microporous polymeric materials. Langmuir : the ACS journal of surfaces and colloids, 29, 2013.

[80] Gilles Pijaudier-Cabot, Romain Vermorel, Christelle Miqueu, and Bruno Mendiboure. Revisiting poromechanics in the context of microporous materials. Comptes Rendus Mécanique, 339(12):770–778, 2011.

[81] Yan Xinlin Hou Yuguang Zhang Jiankun, He Sheng and Chen Xiaojun. Structural characteristics and thermal evolution of nanoporosity in shales. Journal of China University of Petroleum, 41:11–24, 2017.

[82] Shiv Ojha, Siddharth Misra, Ali Tinni, Carl Sondergeld, and Chandra Rai. Estimation of pore-network characteristics and irreducible saturations in wolfcamp and eagle ford shales using low-pressure-nitrogen-adsorption/desorption-isotherm measurements. SPE Reservoir Evaluation & Engineering, 21, 2017.

[83] Amaël Obliger, Colin Bousige, Benoit Coasne, and Jean-Marc Leyssale. Development of atomistic kerogen models and their applications for gas adsorption and diffusion: a mini-review. Energy & Fuels, accepted for publication.

[84] Luís F. M. Franco, Marcelo Castier, and Ioannis G. Economou. Anisotropic parallel self-diffusion coefficients near the calcite surface: A molecular dynamics study. The Journal of chemical physics, 145(8):1–8, 2016.

[85] Tai Bui, Anh Phan, David R. Cole, and Alberto Striolo. Transport mechanism of guest methane in water-filled nanopores. Journal of Physical Chemistry C, 121:15675–15686, 2017.

[86] Ioannis Bitsanis, Jules Magda, Matthew Tirrell, and H. Davis. Molecular dynamics of flow in micropores. The Journal of Chemical Physics, 87:1733–1750, 1987.

[87] James M. D. Macelroy and S.-H. Suh. Simulation studies of a lennard-jones liquid in micropores. Molecular Simulation, 2(4-6):313–351, 1989.

[88] T. Kyle Vanderlick and H. Ted Davis. Self-diffusion in fluids in microporous solids. The Journal of Chemical Physics, 87(3):1791–1795, 1987.

[89] Turgay Ertekin, Gregory R. King, and Fred C. Schwerer. Dynamic Gas Slippage: A Unique Dual-Mechanism Approach to the Flow of Gas in Tight Formations. SPE Formation Evaluation, 1(01):43–52, 1986.

[90] Stephen Whitaker. Flow in porous media i: A theoretical derivation of darcy's law. Transport in Porous Media, 1:3–25, 1986.

[91] Jan von Plato. Boltzmann's ergodic hypothesis. Archive for History of Exact Sciences, 42:71–89, 1991.

[92] Daan Frenkel and Berend Smit. Understanding molecular simulation : from algorithms to applications. 2nd ed, volume 50. Academic Press, 1996.

[93] Loup Verlet. Computer "experiments" on classical fluids. i. thermodynamical properties of lennard-jones molecules. Physical Review, 159:98–103, 1967.

[94] Michael P. Allen and Dominic J. Tildesley. Computer Simulation of Liquids. Oxford University Press, 2017.

[95] William G. Hoover and Brad Lee Holian. Kinetic moments method for the canonical ensemble distribution. Physics Letters A, 211(5):253–257, 1996.

[96] Steven J. Plimpton. Fast parallel algorithms for short-range molecular dynamics. Journal of Computational Physics, 117:1–19, 1993.

[97] Steven J. Stuart, Alan B. Tutein, and Judith A. Harrison. A reactive potential for hydrocarbons with intermolecular interactions. Journal of Chemical Physics, 112:6472–6486, 2000.

[98] Donald W. Brenner, O. A. Shenderova, Judith A. Harrison, Steven J. Stuart, Boris Ni, and Susan B. Sinnott. A second-generation reactive empirical bond order (rebo) potential energy expression for hydrocarbons. Journal of Physics: Condensed Matter, 14:783–802, 2002.

[99] Jonathan G. Harris and Kwong H. Yung. Carbon dioxide's liquid-vapor coexistence curve and critical properties as predicted by a simple molecular model. The Journal of Physical Chemistry, 99:12021–12024, 1995.

[100] Markus Höhnerbach and Paolo Bientinesi. Accelerating AIREBO: Navigating the Journey from Legacy to High-Performance Code. Journal of Computational Chemistry, 40(14):1471–1482, 2019.

[101] Kimberly Chenoweth, Adri C T van Duin, and William A 3rd Goddard. Reaxff reactive force field for molecular dynamics simulations of hydrocarbon oxidation. The Journal of Physical Chemistry A, 112(5):1040–1053, 2008.

[102] Loup Verlet. Computer "experiments" on classical fluids. ii. equilibrium correlation functions. Physical Review, 165:201–214, 1968.

[103] Yuji Sugita and Yuko Okamoto. Replica-exchange molecular dynamics method for protein folding. Chemical Physics Letters, 314(1):141–151, 1999.

[104] N. Metropolis, Arianna W. Rosenbluth, Marshall N. Rosenbluth, A. H. Teller, and Edward Teller. Equation of state calculations by fast computing machines. Journal of Chemical Physics, 21:1087–1092, 1953.

[105] Sriram G. Srinivasan, Adri. C. T. van Duin, and Panchapakesan Ganesh. Development of a reaxff potential for carbon condensed phases and its application to the thermal fragmentation of a large fullerene. The journal of physical chemistry. A, 119 4:571–80, 2015.

[106] Hans C. Andersen. Molecular dynamics simulations at constant pressure and/or temperature. The Journal of Chemical Physics, 72(4):2384–2393, 1980.

[107] Marcus Gary Martin and J. Ilja Siepmann. Transferable potentials for phase equilibria. 1. united-atom description of n-alkanes. Journal of Physical Chemistry B, 102:2569–2577, 1998.

[108] Claudia Crestini, Federica Melone, Marco Sette, and Raffaele Saladino. Milled wood lignin: a linear oligomer. Biomacromolecules, 12:3928–35, 2011.

[109] Michael P. Allen and Dominic J. Tildesley. Computer Simulation of Liquids. 1989.

[110] Glenn J. Martyna, Mark E. Tuckerman, Douglas J. Tobias, and Michael L. Klein. Explicit reversible integrators for extended systems dynamics. Molecular Physics, 87(5):1117–1157, 1996.

[111] Gaël J. Cherfallot, Pierre Levitz, Pauline Michel, Eric Kohler, Jacques Jestin, and Loïc Barré. Probing multiscale structure of mineral and nanoporous kerogen phase in organic-rich source rocks: Quantitative comparison of small-angle x-ray and neutron scattering. Energy & Fuels, 34:9339–9354, 2020.

[112] Xin Gu, David Cole, Gernot Rother, David Mildner, and Susan Brantley. Pores in marcellus shale: A neutron scattering and fib-sem study. Energy & Fuels, 29:1295–1308, 2015.

[113] Joel Sarout and Yves Guéguen. Anisotropy of elastic wave velocities in deformed shales: Experiments and modeling. Geophysics, 73(5):75–89, 2008.

[114] Manas Pathak, Palash Panja, Hai huang, and Milind Deo. Enhanced recovery in shales: Molecular investigation of co2 energized fluid for re-fracturing shale formations. 2016.

[115] Maria Mastalerz, Lilin He, Yuri B. Melnichenko, and John A. Rupp. Porosity of coal and shale: Insights from gas adsorption and sans/usans techniques. International Journal of Coal Geology, 23:5109–5120, 2012.

[116] Paulo J. M. Monteiro, Chris H. Rycroft, and Grigory Isaakovich Barenblatt. A mathematical model of fluid and gas flow in nanoporous media. Proceedings of the National Academy of Sciences of the United States of America, 109(50):20309–20313, 2012.

[117] David Rodney, Anne Tanguy, and Damien Vandembroucq. Modeling the mechanics of amorphous solids at different length scale and time scale. Modelling and Simulation in Materials Science and Engineering, 19:1–49, 2011.

[118] Richard Jana and Lars Pastewka. Correlations of non-affine displacements in metallic glasses through the yield transition. Journal of Physics: Materials, 2(4):1–14, 2019.

[119] Nikolai V. Priezjev. Spatiotemporal analysis of nonaffine displacements in disordered solids sheared across the yielding point. Metallurgical and Materials Transactions A, 51(7):3713–3720, 2020.

[120] Kai Yu, Geoffrey Bowers, Narasimhan L, Andrey Kalinichev, and A. Yazaydin. Diffusion behavior of methane in 3d kerogen models. Energy & Fuels, 35(20):16515–16526, 2021.

[121] Manolis Vasileiadis, Loukas Peristeras, Konstantinos Papavasileiou, and Ioannis Economou. Transport properties of shale gas in relation to kerogen porosity. The Journal of Physical Chemistry C, 122:6166–6177, 2018.

[122] Hongguang Sui, Fengyun Zhang, Ziqiang Wang, Dian sheng Wang, and Yudou Wang. Effect of kerogen maturity, water content for carbon dioxide, methane, and their mixture adsorption and diffusion in kerogen: A computational investigation. Langmuir, 36(33):9756–9769, 2020.

[123] Mahnaz Firouzi and Jennifer Wilcox. Slippage and viscosity predictions in carbon micropores and their influence on 2 and 4 transport. The Journal of Chemical Physics, 138(6):1–12, 2013.

[124] Kristina Ariskina, Guillaume Galliéro, and Amaël Obliger. Free volume model for transport in flexible kerogen of source rock's organic matter. The Journal of Physical Chemistry B, 126(38):7409–7417, 2022.

[125] Hiroshi Fujita. Free volume interpretation of the polymer effect on solvent dynamics. Macromolecules, 26(4):643–646, 1993.

[126] Hiroshi Fujita. Notes on free volume theories. Polymer Journal, 23(12):1499–1506, 1991.

[127] Hiroshi Fujita and Akira Kishimoto. Diffusion-controlled stress relaxation in polymers. ii. stress relaxation in swollen polymers. Journal of Polymer Science, 28(118):547–567, 1958.

[128] Akira Kishimoto and Hiroshi Fujita. Diffusion-controlled stress relaxation in polymers. iii. stress relaxation in a swelling polymer. Journal of Polymer Science, 28(118):569–585, 1958.

[129] Morrel H. Cohen and David Turnbull. Molecular transport in liquids and glasses. The Journal of Chemical Physics, 31(5):1164–1169, 1959.

[130] David Turnbull and Morrel H. Cohen. Free-volume model of the amorphous phase: Glass transition. The Journal of Chemical Physics, 34(1):120–125, 1961.

[131] E.K. Lenzi, L.R. Evangelista, M.K. Lenzi, H.V. Ribeiro, and E.C. de Oliveira. Solutions for a non-markovian diffusion equation. Physics Letters A, 374(41):4193–4198, 2010.

[132] Marco da Silva, G. Viswanathan, and J. Cressoni. Ultraslow diffusion in an exactly solvable non-markovian random walk. Physical review, 89:1–9, 2014.

[133] Gerhard Jung, Martin Hanke, and Friederike Schmid. Iterative reconstruction of memory kernels. Journal of chemical theory and computation, 13(6):2481—2488, 2017.

[134] Ch.G. van Weert. Generalized hydrodynamics from relativistic kinetic theory. Physica A-statistical Mechanics and Its Applications, 111:537–552, 1982.

[135] B. Markiv, I. Omelyan, and M. Tokarchuk. Consistent description of kinetics and hydrodynamics of weakly nonequilibrium processes in simple liquids. Journal of Statistical Physics, 155:843–866, 2014.

[136] R.F. Rodríguez, J. Fujioka, and E. Salinas-Rodríguez. Fractional correlation functions in simple viscoelastic liquids. Physica A: Statistical Mechanics and its Applications, 427:326–340, 2015.

[137] M. Dentz, M. Icardi, and J. J. Hidalgo. Mechanisms of dispersion in a porous medium. Journal of Fluid Mechanics, 841:851–882, 2018.

[138] Lorenzo Costigliola, David Heyes, Thomas Schroeder, and Jeppe Dyre. Revisiting the stokes-einstein relation without a hydrodynamic diameter. The Journal of Chemical Physics, 150:021101, 2019.

[139] Robert Zwanzig. Memory effects in irreversible thermodynamics. Physical Review, 124:983–992, 1961.

[140] Hazime Mori. Transport, collective motion, and brownian motion. Progress of Theoretical Physics, 33(3):423–455, 1965.

[141] Robert W. Zwanzig. Nonequilibrium statistical mechanics. Physics Subject Headings, 2001.

[142] Dominika Lesnicki. Flots microscopiques et mécanisme de la diffusion en phase liquide. PhD thesis, Université Pierre et Marie Curie, 2015.

[143] Hyun Shin, Changho Kim, Peter Talkner, and Eok Lee. Brownian motion from molecular dynamics. Chemical Physics, 375:316–326, 2010.

[144] Antoine Carof, Rodolphe Vuilleumier, and Benjamin Rotenberg. Two algorithms to compute projected correlation functions in molecular simulations. The Journal of chemical physics, 140:1–9, 2014.

[145] Gerhard Jung. Coarse-Graining Frequency-Dependent Phenomena and Memory in Soft Matter Systems. PhD thesis, The Johannes Gutenberg University Mainz, 2018.

[146] Noel Corngold. Behavior of autocorrelation functions. Physical Review A, 6:1570–1573, 1972.

[147] Thomas Franosch, Matthias Grimm, Maxim Belushkin, Flavio Maurizio Mor, Giuseppe Foffi, László Forró, and Sylvia Jeney. Resonances arising from hydrodynamic memory in brownian motion. Nature, 478:85–88, 2011.